



January 2019

Development Of DNA-Based Biosensors And Antibacterial Additive

Yuqian Xing

[How does access to this work benefit you? Let us know!](#)

Follow this and additional works at: <https://commons.und.edu/theses>

Recommended Citation

Xing, Yuqian, "Development Of DNA-Based Biosensors And Antibacterial Additive" (2019). *Theses and Dissertations*. 2492.

<https://commons.und.edu/theses/2492>

This Dissertation is brought to you for free and open access by the Theses, Dissertations, and Senior Projects at UND Scholarly Commons. It has been accepted for inclusion in Theses and Dissertations by an authorized administrator of UND Scholarly Commons. For more information, please contact und.common@library.und.edu.

DEVELOPMENT OF DNA-BASED BIOSENSORS AND ANTIBACTERIAL
ADDITIVE

by

Yuqian Xing
Bachelor of Science, Hunan University, 2009
Master of Engineering, Hunan University, 2012

A Dissertation

Submitted to the Graduate Faculty

of the

University of North Dakota

In partial fulfillment of the requirements

for the degree of

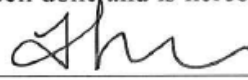
Doctor of Philosophy

Grand Forks, North Dakota

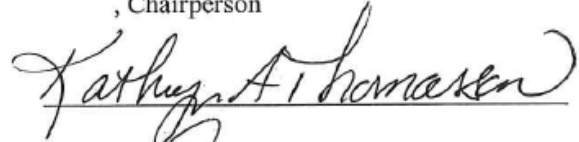
May
2019

Copyright 2019 Yuqian Xing

This dissertation, submitted by *Yupian Xing* in partial fulfillment of the requirements for the Degree of *Philosophy* from the University of North Dakota, has been read by the Faculty Advisory Committee under whom the work has been done, and is hereby approved.



, Chairperson



This dissertation is being submitted by the appointed advisory committee as having met all of the requirements of the School of Graduate Studies at the University of North Dakota and is hereby approved.



Dr. Chris Nelson, Associate Dean
School of Graduate Studies

4/30/19

Date

PERMISSION

Title Development of DNA-Based Biosensors and Antibacterial Additive

Department Chemistry

Degree Doctor of Philosophy

In presenting this dissertation in partial fulfillment of the requirements for a graduate degree from the University of North Dakota, I agree that the library of this University shall make it freely available for inspection. I further agree that permission for extensive copying for scholarly purposes may be granted by the professor who supervised my dissertation work or, in her absence, by the Chairperson of the department or the dean of the School of Graduate Studies. It is understood that any copying or publication or other use of this dissertation or part thereof for financial gain shall not be allowed without my written permission. It is also understood that due recognition shall be given to me and to the University of North Dakota in any scholarly use which may be made of any material in my dissertation.

Yuqian Xing
May 2019

TABLE OF CONTENTS

LIST OF FIGURES	VIII
LIST OF TABLES	XIII
LIST OF SCHEMES.....	XIV
ACKNOWLEDGEMENTS.....	XV
ABSTRACT.....	XVII
CHAPTER I.....	1
ULTRASENSITIVE DETECTION OF MERCURY IONS USING SINGLE PARTICLE INDUCTIVELY COUPLED PLASMA-MASS SPECTROMETRY	1
1. INTRODUCTION	1
2. EXPERIMENTAL SECTION	4
2.1. <i>Chemicals and Instruments</i>	4
2.2. <i>Instruments</i>	4
2.3. <i>Preparation of ssDNA Modified AuNPs</i>	6
2.4. <i>Detection of Hg²⁺ Using spICP-MS</i>	6
3. RESULTS AND DISCUSSION.....	7
3.1. <i>Detection of Hg²⁺ Using spICP-MS</i>	7
3.2. <i>Synthesis of AuNP-ssDNA</i>	8
3.3. <i>Feasibility Investigation</i>	10
3.4. <i>Optimizations</i>	13
3.5. <i>Characteristics of Hg²⁺ Analysis Method</i>	14
3.6. <i>Selectivity</i>	19
3.7. <i>Analysis of Real Sample</i>	19
4. CONCLUSIONS.....	20
CHAPTER II.....	21
AN ULTRASENSITIVE GOLD NANOPARTICLE BASED GRAPHENE BIOSENSING PLATFORM USING SINGLE PARTICLE INDUCTIVELY COUPLED PLASMA MASS SPECTROMETRY	21
1. INTRODUCTION	21
2. EXPERIMENTAL SECTION	23
2.1. <i>Materials</i>	23
2.2. <i>Instruments</i>	24
2.3. <i>Preparation of ssDNA Modified AuNPs</i>	25
2.4. <i>Adsorption of ssDNA to GO</i>	26
2.5. <i>Analysis of Thrombin by GO/AuNPs Composites Using spICP-MS</i>	26

3. RESULTS AND DISCUSSION.....	26
3.1. <i>Design of the Biosensing Platform.</i>	26
3.2. <i>Formation of GO/AuNPs Composites.</i>	28
3.3. <i>Validation of spICP-MS for Ultrasensitive Detection.</i>	32
3.4. <i>Optimizations.</i>	35
3.5. <i>The Sensitivity of Thrombin Detection.</i>	37
3.6. <i>Selectivity.</i>	39
4. CONCLUSIONS.....	40
CHAPTER III	42
DETECTION OF ESCHERICHIA COLI IN DRINKING WATER USING DSDNA- TEMPLATED COPPER NANOPARTICLES WITH HYBRIDIZATION CHAIN REACTION	42
1. INTRODUCTION	42
2. EXPERIMENTAL SECTION	44
2.1. <i>Materials.</i>	44
2.2. <i>Instruments.</i>	45
2.3. <i>Preparation of Antibody Conjugated Magnetic Beads (MBs).</i>	45
2.4. <i>Bacteria Culture.</i>	45
2.5. <i>Bacteria Capture Using Antibody Conjugated MBs.</i>	46
2.6. <i>Fluorescence Detection Using dsDNA Templated CuNPs.</i>	46
3. RESULTS AND DISCUSSION.....	47
3.1. <i>Design of the Biosensor Platform for Bacterial Detection.</i>	47
3.2. <i>Antibody Modified MBs for Specifically Capturing E. coli.</i>	48
3.3. <i>Formation of Fluorescent CuNPs through dsDNA Templating.</i>	49
3.4. <i>Amplification by the Hybridization Chain Reaction (HCR)</i>	49
3.5. <i>Optimizations.</i>	51
3.6. <i>Application of the Biosensing System for the Detection of E. coli in Water.</i>	53
3.7. <i>Selectivity of the Biosensor.</i>	54
4. CONCLUSIONS.....	55
CHAPTER IV	56
BIOCOMPATIBLE G-QUADRUPLEX/HEMIN FOR ENHANCING ANTIBACTERIAL ACTIVITY OF H ₂ O ₂	56
1. INTRODUCTION	56
2. EXPERIMENTAL SECTION	59
2.1. <i>Materials.</i>	59
2.2. <i>Instruments.</i>	59
2.3. <i>Preparation of DNzyme.</i>	60
2.4. <i>Culture of Bacteria and Detection of Antibacterial Activity of the Developed Reagents.</i>	60
2.5. <i>Study of the Cell Wall/Membrane Integrity.</i>	61
2.6. <i>In Vivo Mouse Wound Model.</i>	61
2.7. <i>Cytotoxicity of G/H Complex Used as Additive.</i>	61

2.8. Spin Trapping Technique Using Electron Paramagnetic Resonance for Detection of $\cdot\text{OH}$	62
3. RESULTS AND DISCUSSION.....	62
3.1. Formation of A Hydroxyl Radical from H_2O_2 by G/H DNAzyme.	62
3.2. Optimization of the Peroxidase-Mimic Activity of the G/H DNAzyme.	65
3.3. Enhanced Antibacterial Property of H_2O_2 by G/H Complex.....	66
3.4. Effect of G/H Complex on Bacterial Cell Membrane Integrity.....	69
3.5. Anti Infection Effect of the G/H Complex on Wound Healing.	71
3.6. Cytotoxicity Study of the G/H Complex.	73
4. CONCLUSIONS.....	74
REFERENCES	76

LIST OF FIGURES

Figure	Page
1. Characterization of AuNP-ssDNA composites. A, UV-Vis spectra of bare and AuNPs modified with ssDNA; B, UV-Vis spectra of AuNP-ssDNA with or without 10 ppm Hg ²⁺ in water; C, Electrophoresis gel image of AuNP-ssDNA: Lane 1 with bare AuNPs, Lane 2 with AuNP-A ₁₀ P1 conjugate, Lane 3 with AuNP-A ₁₀ P2 conjugate, Lane 4 with AuNP-A ₁₀ P1 conjugate and AuNP-A ₁₀ P2 conjugate, Lane 5 with AuNP-A ₁₀ P1 conjugate and AuNP-A ₁₀ P2 conjugate + 10 ppm of Hg ²⁺	9
2. TEM image of AuNPs modified with ssDNA. A, bare AuNPs; B, AuNP-A ₁₀ P1 conjugate; C, AuNP-A ₁₀ P2 conjugate; D, AuNP-A ₁₀ P1 conjugate and AuNP-A ₁₀ P2 conjugate	9
3. A-D, spICP-MS spectra of AuNPs with different sizes (A: 20 nm, B: 30 nm, C: 40 nm, D: 60 nm); E-F, spICP-MS spectra of 30 nm-AuNPs at different concentrations (E: 1×10 ⁴ particles(P)/mL, F: 2×10 ⁴ P/mL, G: 5×10 ⁴ P/mL, H: 1×10 ⁵ P/mL,). (¹⁹⁷ Au, dwell time: 5ms)	11
4. A, Relationship between average peak intensity and AuNPs mass in different sizes (20, 30, 40 and 60 nm); B, Relationship between number of peaks and 30 nm AuNPs concentration collected in 180 s acquisition time (10 ⁴ , 2×10 ⁴ , 5×10 ⁴ and 10 ⁵ P/mL).	12
5. spICP-MS spectra of AuNPs-ssDNA in 10 mM PB buffer pH 7.4 without (A, AuNP-A ₁₀ P1; B, AuNP-A ₁₀ P2; C, AuNP-A ₁₀ P1 and AuNP-A ₁₀ P2) or with (D, AuNP-A ₁₀ P1; E, AuNP-A ₁₀ P2; F, AuNP-A ₁₀ P1 and AuNP-A ₁₀ P2) 1 M NaCl. (¹⁹⁷ Au, dwell time: 5ms).	13
6. The optimizations of AuNPs particle number concentrations (A), incubation temperature (B), and incubation time (C). Hg ²⁺ concentration: 1 ppb.....	14
7. spICP-MS spectra of AuNP-ssDNA in presence of different concentrations of Hg ²⁺ . A, without Hg ²⁺ ; B-K, Hg ²⁺ concentrations in 0.01 ppt, 0.1 ppt, 1 ppt, 10 ppt, 100 ppt, 1 ppb, 10 ppb, 100 ppb, 1 ppm. (¹⁹⁷ Au, dwell time: 5ms).....	16
8. TEM image of AuNP-ssDNA in presence of different concentrations of Hg ²⁺ . A, AuNP-ssDNA without Hg ²⁺ ; B-E, AuNPs-ssDNA with Hg ²⁺ in 10 ppb, 100 ppb, 1 ppm, 10 ppm.	17
9. Relationship between aggregation efficiency and Hg ²⁺ in concentration from 0.1 ppt to 10 ppm. Linear range from 0.1 ppt to 1 ppb	17

10. Relationship between average intensity and Hg^{2+} in concentration from 0.1 ppt to 10 ppm. Linear range from 0.1 ppt to 1 ppb.....	18
11. Selectivity of the AuNP-ssDNA probe for Hg^{2+} detection by spICP-MS. Hg^{2+} concentration: 1 ppb; other ion concentrations: 100 ppb.....	19
12. Zeta potential measurements of the nanomaterials. A, bare AuNPs (-42.71±3.20 mV); B, AuNPs-TOEG6 (-20.08±1.54 mV); C, AuNPs-aptamer (-25.98±2.63 mV); D, GO (-43.28±0.63 mV).....	30
13. UV-Vis absorption of AuNPs at 520 nm with different concentration of MgCl_2 (A) or NaCl (B). The AuNPs were in the filtrate after incubation with GO in a PB buffer (10.0 mM, pH 7.4).....	30
14. Photos of GO/AuNPs collected on the filter membrane surface. A, GO only; B, AuNPs-aptamer only; C, GO and AuNPs-ssDNA; D, GO and AuNPs-TOEG6. Incubated in 1.0 mL of 10.0 mM PB buffer with 0.5 mM MgCl_2 (pH 7.4) for 10 min at room temperature. The GO concentration: 20 $\mu\text{g/mL}$; AuNPs concentration: 10^{10} nanoparticles/mL.	31
15. TEM image of the GO/AuNPs composites re-dispersed in water. The GO/AuNPs composites were obtained by incubating a 50 μL aliquot of 5×10^{11} particle/mL AuNPs-ssDNA and 50 μL of 400.0 $\mu\text{g/mL}$ of GO in 1.0 mL of PBS buffer (10 mM with 0.5 mM MgCl_2 , pH 7.4) at room temperature for 30 min. Scale bar: 200 nm.....	32
16. spICP-MS spectra of AuNPs in different particle number concentrations. A-G: 0, 100, 500, 1,000, 5,000, 10,000, and 100,000 particles/mL. (^{197}Au , dwell time: 5 ms). H. Relationship between the number of pulses and the particle number concentration from 0 to 100,000 particles/mL within 180 s collection time. Inset: Calibration curve of the number of pulses and the particle number concentration from 0 to 10,000 particles/mL.....	34
17. The optimizations of aptamer density on AuNPs (A), and incubation time (B). Thrombin concentration: 10 pM. GO/AuNPs composites concentration: 1 $\mu\text{g/mL}$ (GO mass based) Incubation in PBS buffer (10 mM with 0.5 mM MgCl_2 , pH 7.4).	37
18. spICP-MS spectra of AuNPs in the presence of different concentrations of Thrombin (A to J: 0, 10^{-4} , 10^{-3} , 10^{-2} , 10^{-1} , 1, 10, 10^2 , 10^3 , 10^4 pM). GO/AuNPs composites concentration: 1 $\mu\text{g/mL}$ (GO mass based). Incubation at 37 °C for 60 min in PBS buffer (10 mM, 0.5 mM MgCl_2 , pH 7.4). 200 folds dilution before injecting into spICP-MS (^{197}Au , dwell time: 5 ms).....	38
19. Relationship between the changes of number of detected AuNPs and thrombin in concentration from 10^{-4} to 10^4 pM. Collection time: 180 s. Inset: Calibration curve of changes of number of detected AuNPs and thrombin concentration from 10^{-2} to 10^2 pM.....	38

20. Selectivity of the platform for thrombin detection by spICP-MS. Thrombin concentration: 10.0 pM; BSA and IgG concentrations: 1.0 μM; FBS concentration: ~ 0.1 g protein/L. GO/AuNPs composites concentration: 1 μg/mL (GO mass based). Incubation at 37 °C for 60 min in PBS buffer (10 mM, 0.5 mM MgCl₂, pH 7.4). 40
21. SEM images of MBs (1 μ M) incubated with *E. coli* (A) and *S. aureus* (B). Incubate at 37 °C for 20 min; Bacteria concentration: 10⁶ CFU/mL..... 49
22. The size distribution of CuNPs (A), and the Fluorescence spectrum of CuNPs(B)..... 49
23. A, Fluorescence spectra of the CuNPs formed using different templates: a, no DNA; b, 1 μM HP1 only; c, 1 μM HP2 only; d, 1 μM HP2 and 50 nM Primer; e, 500 nM HP1 and 500 nM HP2; f, 500 nM HP1, 500 nM HP2 and 50 nM Primer. HCR reaction time was 1 h. The concentration of Cu²⁺ and sodium ascorbate were 200 μM and 4 mM, respectively. CuNPs formation time was 10 min. The excitation wavelength was 350 nm. B, Photograph of the fluorescent CuNPs formed using different templates under an UV excitation..... 51
24. The effect of different experimental conditions on the detection of *E. coli*. A, Impact of amount of antibody modified MBs on the capture efficiency of *E. coli*. B, Impact of incubation time between MBs and bacteria on the capture efficiency of *E. coli*. C, Time dependence of the fluorescence intensity after adding Cu²⁺ (200 μM) and sodium ascorbate (4 mM), 500 nM of HP1 and 500 nM of primer probes for formation of CuNPs, λ_{em}= 615 nm, λ_{ex}= 350 nm. D, Impact of incubation time of HCR amplification on the fluorescence of CuNPs with 50 nm of primer, 500 nM of HP1 and 500 nM of HP2..... 53
25. A, Fluorescence of dsDNA templated CuNPs to different concentrations of *E. coli* O157:H7. (0, 10³, 5×10³, 10⁴, 5×10⁴, 10⁵, 10⁶, 10⁷, and 10⁸ CFU/mL). B, Relationship of bacteria concentration (0, 5×10³, 10⁴, 5×10⁴, 10⁵, 10⁶, 10⁷, and 10⁸ CFU/mL) and fluorescence intensity of CuNPs. Inset: Linear range from 5×10³ to 10⁵ CFU/mL. Ex: 350 nm; Em: 615 nm. 54
26. Fluorescence of dsDNA templated CuNPs to target *E. Coli* various other bacteria strains (*A. baumannii*, *K. pneumoniae*, *S. aureus*, and *P. aeruginosa*) at a concentration of 10⁵ CFU/mL. Ex: 350 nm; Em: 615 nm. 55
27. CW EPR spectra of DMPO-OH. Conditions: 10 mM H₂O₂, 25 μM G/H complex, 500 mM DMPO in 25 mM Tris-HCl buffer (pH 6.8), incubation at room temperature for 30 min. Signal average time is 20-25 min for each sample. 63
28. Normalized fluorescence spectra of TAOH formed under different conditions, including only TA (curve a); TA and G/H complex (curve b) ; TA and H₂O₂ (curve c) ; and TA, H₂O₂, and G/H complex (curve d) . Conditions: 20 mM PBS buffer (pH 7.4), incubation at room temperature for 12 h. The concentrations of TA, H₂O₂, and the G/H complex were 0.5 mM, 1 mM, and 1 μM, respectively. λ_{ex}: 315 nm, λ_{em} : 435 nm. Inset: the normalized ΔPL intensity

- with or without the G/H complex. 64
29. Peroxidase-mimic property verification by directly monitoring the color change (A) and UV- Vis spectra (B) of 5 mM ABTS solution in 25 mM Tris-HCl buffer (pH 6.8) containing (a) ABTS only; (b) 5 mM H₂O₂; (c) 1 μM G/H complex; (d) 5 mM H₂O₂ + 1 μM Hemin; (e) 5 mM H₂O₂ + 1 μM G/H complex. Incubation at room temperature for 10 min. 65
30. Optimization of peroxidase-mimic activity of G/H complex: (A) Plots of absorbance at 420 nm versus G/H complex at different temperatures. Experiments were performed using the 1 μM G/H complex and 1 mM H₂O₂ in 25 mM Tris-HCl buffer (pH 6.8) with 2 mM ABTS work solution at different temperatures. (B) V_0 values of the G/H complex at different temperatures. (C) V_0 values of the G/H complex at different pH. Experiments were performed using 1 μM G/H complex and 1 mM H₂O₂ in 2 mM ABTS working solution at 37 °C at different pH. 66
31. A, Survival rate of *E. coli* treated with H₂O₂ at different concentration coinubation (10⁻⁸, 10⁻⁷, 10⁻⁶, 10⁻⁵, 10⁻⁴, 10⁻³, 10⁻², 10⁻¹ M) with or without 1 μM G/H complex. Incubation at 37 °C for 30 min in Tris-HCl buffer. B, Growth inhibition experiment by incubation in 0.01 M H₂O₂ with or without a 1 μM G/H complex at 37 °C in different medium solutions at 1 and 5 h. *p < 0.01. C and D for Gram-negative bacteria, *S. aureus*. The experimental conditions are similar to A and B. 68
32. Representative photos of bacterial colonies showing the influences of the catalytic activity of the G/H complex on the growth of *E. coli*. (up) and *S. aureus* (bottom). (A and E) bacterial cells only; (B and F) bacteria with 1 μM G/H complex; (C and G) bacteria with 0.01 M H₂O₂; (D and H) bacteria with 0.01 M H₂O₂ + 1 μM G/H complex. Incubation at 37 °C for 30 min. 69
33. Fluorescence images of live and dead *E. coli* cells after incubation with 10 mM H₂O₂ for 2 h: (A) *E. coli* only; (B) *E. coli* with 1 μM of G/H complex; (C) *E. coli* with 0.01 M H₂O₂; (D) *E. coli* with 0.01 M H₂O₂ + 1 μM G/H complex. Blue fluorescence shows bacterial quasinuclear staining with DAPI, while red fluorescence shows dead bacteria staining with PI. Bar scale: 20 μm. 70
34. SEM images of bacterial morphology. (A) *E. coli*; (B) *E. coli* incubated with 1 μM G/H complex; (C) *E. coli* incubated with 0.01 M H₂O₂; (D) *E. coli* incubated with 0.01 M H₂O₂ and 1 μM G/H complex; (E) *S. aureus*; (F) *S. aureus* incubated with 1 μM G/H complex; (G) *S. aureus* incubated with 0.01 M H₂O₂; (H) *S. aureus* incubated with 0.01 M H₂O₂ and 1 μM G/H complex. Incubation at 37°C for 30 min. 71
35. Photographs of wounds on mice treated with different solutions (0.1 M H₂O₂, saline, 1 μM G/H complex, 1 mM H₂O₂, 1 μM G/H complex + 1 mM H₂O₂) at indicated times. 73
36. Relative cell viability of *E. coli* and *S. aureus* (A) and SW620 and MH-S (B) after culturing with different concentrations of G/H complex (0, 5, 10, 20, 30,

40, 50 to 60 μM). Incubation conditions: 5 h for bacteria, 24 h for SW620 and MH-S at 37 $^{\circ}\text{C}$ 74

LIST OF TABLES

Table	Page
1. Instrument parameters used for spICP-MS measurements	5
2. DMA-80 conditions used for Hg determinations of aqueous samples	6
3. Comparison of AuNPs for Hg ²⁺ detection based on aggregation strategy.....	18
4. Spike recovery efficiency of spICP-MS method for Hg ²⁺ detection in the tap water and river water(n=3).	20
5. ICP-MS instrument parameters used for conventional and single-particle measurements.....	25
6. AuNPs particle number concentration quantified by spICP-MS and conventional ICP-MS.	35
7. Effect of TOEG6 concentration on aptamer binding to AuNPs.	36

LIST OF SCHEMES

Scheme	Page
1. Schematic illustration of Hg ²⁺ detection using probe modified AuNPs by spICP-MS.....	8
2. Schematic illustration of thrombin detection using aptamer modified AuNPs by spICP-MS. A, thrombin aptamer modified AuNPs incubated with GO; B, thrombin molecule as target incubated with GO/AuNPs composites; C, desorbed AuNPs were separated and introduced into spICP-MS; D, no thrombin molecule added as control.	28
3. Scheme for the detection of <i>E. coli</i> using dsDNA-templated CuNPs amplified by the HCR	48

ACKNOWLEDGEMENTS

Many people have earned my gratitude for their contributions to me during my Ph.D. study. I would never have been possible to finish my dissertation without whom guide, help, and support in my study and life: my committee members, the faculty members, and my lab mates, the financial support, and my family.

I would like to express my deepest gratitude to my advisor, Dr. Julia Xiaojun Zhao, for the guidance, caring, encouragement and patience during my graduate studies at the University of North Dakota. She not only helped me to finish my study and get a degree but also train me to be independent in my future career. I am grateful for everything she did for me. I would also like to thank all of my committee members: Dr. David T. Pierce, Dr. Alena Kubátová, Dr. Kathryn A. Thomasson, and Dr. Colin Combs. Thank Dr. Pierce for his guidance in my research, especially for those spICP-MS projects, and his revision for my research paper and dissertation. I know that it was extremely hard work and took a lot of effort due to my poor writing skill. Thanks so much. Thank Dr. Kubátová for offering several opportunities to participate in all the outreach activities, which is a great experience out of the research. Thank Dr. Thomasson for your encouragement all the time, and the cards received every year. Thank Dr. Combs for the guidance and offering the opportunities to work in his lab. Thank all of my committee members for their thought-provoking suggestions for my projects during my OPR. I would like to thank Dr. Min Wu from the School of Medicine and Health for his assistance and guidance in my research projects. I would like to thank all of the chemistry department faculty for their education and staff for their assistant.

Next, I would like to thank all of my current and former colleagues in Dr.

Zhao's group. They are Dr. Xu Wu, Dr. Jiao Chen, Dr. Fei Tian, Shaina Mattingly, Dr. Xuefei Zhang, Xiao Liu, Juan Han, Dr. Ying Zhang, Wen Sun, Dr. Yanxi Zhou, Yingfen Wu, and Sarah Reagen. Specially thanks to Qinqin Pu and Xuefeng Li from Dr. Wu's group, for the help of biological experiments

I am truly grateful for the financial support I received from NSF, NIH, North Dakota INBRE, UND Graduate School, and UND Chemistry Department. Without their financial support, I could never make it so far. Meanwhile, I appreciate the technical support from the Basic Science Imaging Center for training me on the microscopes and allowing me to use these instruments independently.

Finally, and most importantly, I would like to thank my family: my parents, my dear wife, and my little princess. Thanks for their, encouragement, patience and love, that support me to finish this work.

ABSTRACT

In the first project, an ultrasensitive assay has been developed for the detection and determination of $\text{Hg}^{2+}(\text{aq})$ based on single-particle inductively coupled plasma-mass spectrometry (spICP-MS). In the presence of $\text{Hg}^{2+}(\text{aq})$, AuNPs modified with a segment of single-stranded DNA can aggregate due to the formation of well-known thymine (T)- Hg^{2+} -T complex. The spICP-MS can sensitively and quantitatively measure the degree of aggregation by the overall decrease in number of detected AuNPs or NP aggregates. Compared with most other Hg assays that use the same principle of aggregation-dispersion with DNA modified AuNPs, this spICP-MS-based method achieved a much lower detection limit of 0.031 part-per-trillion (155 fM) and a wider (10,000-fold) linear range up to 1 ppb. The method also showed good potential for practical applications with the environment and biomedical samples because it demonstrated minimal interference from the sample matrix. Moreover, this method, with its outstanding sensitivity could be expanded for the detection of other targets by designing the recognition unit on gold nanoparticles.

In the second project, an ultrasensitive assay for biomolecules has been developed using graphene/gold nanoparticles (AuNPs) composites and single-particle inductively coupled plasma-mass spectrometry (spICP-MS). Thrombin was chosen as a model biomolecule for this study. AuNPs modified with thrombin aptamers were first non-selectively adsorbed onto the surface of graphene oxide (GO) to form GO/AuNPs composites. In the presence of thrombin, the AuNPs desorbed from the GO/AuNPs composites due to a conformation change of the thrombin aptamer after binding with thrombin. The desorbed AuNPs were proportional to the concentration of thrombin and

could be quantified by spICP-MS. By counting the individual AuNPs in the spICP-MS measurement, the concentration of thrombin could be determined. This assay achieved an ultralow detection limit of 4.5 fM with a broad linear range from 10 fM to 100 pM. The method also showed excellent selectivity and reproducibility when a complex protein matrix was evaluated. Furthermore, the diversity of ssDNA ligands made this method a promising new technology for ultrasensitive detection of a wide variety of biomarkers in clinical diagnostics.

In the third project, a novel sandwich bioreagent for sensitive and selective detection of *E. coli* bacteria was developed. The bioreagent combined antibody and aptamer as selective ligands and CuNPs as fluorescent signal labels. To further improve the method sensitivity, a hybridization chain reaction (HCR) amplification strategy was applied. *E. coli* bacteria in water were first captured by the anti-*E. coli* antibody modified magnetic beads and used to obtain the primer for HCR based on the aptamer. Ultimately, the fluorescent CuNPs were produced using the long length dsDNA formed during HCR as templates. The measured fluorescence intensity was directly dependent on *E. coli* concentration. A low detection limit of 5,200 CFU/mL and excellent selectivity were achieved under the optimal conditions. Moreover, the method exhibited great potential for detection of other bacteria in environmental analysis and clinical diagnostics.

In the fourth project, the G-quadruplex/hemin (G/H) complex was applied as an additive to increase the antibacterial efficiency of H₂O₂ and avoid serious toxicity effect. The G/H complex catalyzes the decomposition of H₂O₂ and yields a higher hydroxyl radical (\cdot OH) generation during the procedure. The formed \cdot OH has a higher antibacterial performance than the original H₂O₂. Using the G/H complex as an additive, the antibacterial activity of H₂O₂ was vastly enhanced against both Gram-positive and

Gram-negative bacteria *in vitro* experiments. Furthermore, the designed antibacterial system was applied using a mouse wound model *in vivo* and showed outstanding prevention of wound infection and facilitation of wound healing. The study demonstrated the utility of using the G/H complex to help control both Gram-positive and Gram-negative infections.

CHAPTER I

ULTRASENSITIVE DETECTION OF MERCURY IONS USING SINGLE PARTICLE INDUCTIVELY COUPLED PLASMA-MASS SPECTROMETRY

1. Introduction

Mercury (Hg) is well-known to have a low level but widespread distribution in the environment and has been found in air, water, and soil.¹⁻² Mercury compounds are particularly hazardous pollutants because of their high toxicity and tendency to bioaccumulate, thereby causing serious risks to environmental and human health.³ Mercury commonly exists in three basic forms: metallic or elemental mercury (Hg^0), ionic mercury (Hg^{2+} or Hg_2^{2+}) typically comprising sparingly soluble halide and chalcogenides compounds, and organic mercury like methylmercury.⁴ The elemental mercury is volatilized during combustion of fossil fuels and is eventually oxidized to Hg^{2+} in the atmosphere and deposited on land or in the ocean.⁵ This ionic mercury is easily methylated to organic mercury, which accumulates in the food chain to pose adverse health effects for human beings.⁶⁻⁹ To establish safety margins for the food supply, the US Environmental Protection Agency (EPA) has set the maximum contaminant level of mercury in drinking water at 2.0 ppb, and the US Food and Drug Administration (FDA) has set a guideline of mercury compounds in food at 1.0 ppm.¹⁰⁻¹¹ Therefore, it is essential to develop a high sensitive and selective method for monitoring the low concentration of Hg^{2+} in environment and food. To date, various types of analytical techniques for the detection of Hg^{2+} , including fluorescence,¹²⁻¹³ atomic absorption spectroscopy,¹⁴ and surface-enhanced Raman scattering¹⁵ have been developed. However, these methods require time-consuming and tedious sample preparation and treatment.

Recently, more interest has been shown in the development of nanomaterial-based methods and reagents for analysis. As a well-studied nanomaterial, gold

nanoparticles (AuNPs) have been widely applied in various assays for Hg^{2+} based on their excellent optical, electrochemical and other properties.¹⁶⁻¹⁸ As far as we know, previous studies have focused exclusively on Hg^{2+} induced aggregation of AuNPs, which can be manifested by a significant change of the AuNPs plasmon peak.¹⁷ Two strategies are commonly used to fabricate these assays. One is to disrupt the protecting function of the surface ligands of the AuNPs under special conditions, like high ionic strength conditions, thereby causing the aggregation of the AuNPs.¹⁹ For instance, Liu and co-workers designed AuNPs with a physically adsorbed single-stranded DNA (ssDNA), that form double-stranded DNA (dsDNA) in the presence of Hg^{2+} due to the thymine- Hg^{2+} - thymine (T- Hg^{2+} -T) interaction.²⁰ The dsDNA easily desorbs from the surface of the AuNPs and induce aggregation in a high concentration of NaCl that is proportional to Hg^{2+} concentration. Another strategy uses Hg^{2+} -induced crosslinking reaction between two or more AuNPs modified with the same or different ligands, respectively. For example, Du and co-workers used urine to ligate the surface of AuNPs and work as ligands. Adding Hg^{2+} led to crosslinking of the AuNP ligand and induced the aggregation of AuNPs.²¹ Despite the success of these methods at promoting Hg^{2+} -selective aggregation of AuNPs, their sensitivity is compromised by the low sensitivity of the AuNP plasmon absorption.

Over the last decade, inductively coupled plasma-mass spectrometry(ICP-MS) has gained tremendous research interest for single nanoparticle analysis.²²⁻²⁴ Single particle ICP-MS (spICP-MS) is a time-based analysis method that yields a large data set (usually over 10,000 measurements) spanning a relatively long acquisition period (> 60 s). It is performed with the MS tuned to a target isotope and configured to repeatedly measure counts of this isotope over a short dwell time (5-10 ms). If the sample analyzed is sufficiently dilute ($< 10^6$ particles/mL), a high proportion of the dwell-time

measurements (over 50%) show only background levels of the target isotope. However, the other dwell-time measurements show counts significantly higher than the background. Ideally, these spikes or peaks in isotope count reflect the signal of a single nanoparticle reaching the torch plasma within one measurement cycle and the isotope count is directly proportional to the particle mass. Such spICP-MS can provide not only information about the nanoparticle size and size distribution, but it can also determine the exact number of the nanoparticle in solution. Furthermore, interactions such as agglomeration and disaggregation between two or more nanoparticles can be easily identified by changes to spICP-MS signal. Combined with the excellent analytical features of ICP-MS, including high sensitivity, wide linear range, and absolute quantification, routine single nanoparticle analysis now is a promising starting point for extremely sensitive bioassays. Because AuNPs are composed of a highly abundant isotope (^{197}Au) and are easy to be functionalized, they are becoming widely applied in spICP-MS studies. For instance, Han and co-workers developed a one-step homogeneous DNA assay with AuNPs using spICP-MS. The concentration-dependent changes to the spICP-MS made it possible to detect target DNA down to 1 pM.²⁵

Here, I present a new strategy for highly sensitive and selective determination of Hg^{2+} ion using spICP-MS AuNPs modified with ssDNA. Samples of 30 nm AuNPs were individually functionalized with two ssDNA probes (Probe 1 and Probe 2). In the presence of Hg^{2+} , agglomeration occurs between AuNP-Probe 1 conjugates and AuNP-Probe 2 conjugates due to the formation of T- Hg^{2+} -T containing dsDNA. According, reduced number of AuNPs or gold clusters observed in spICP-MS decreased with Hg^{2+} concentration in a well-defined manner. This designed assay can selectively detect Hg^{2+} as low as 155 fM.

2. Experimental Section

2.1. Chemicals and Instruments.

Gold nanoparticles with different sizes were purchased from Cytodiagnostics Inc (Burlington, Canada). Mercury standard, mercury(II) chloride, (11-mercaptopundecyl)hexa(ethylene glycol) (TOEG6), tris(2-carboxyethyl)phosphine hydrochloride (TCEP), polyethylene glycol sorbitan monolaurate (Tween-20), sodium chloride, sodium phosphate monobasic, sodium phosphate dibasic, sodium citrate tribasic dihydrate were purchased from Sigma-Aldrich (St. Louis, MO). Deionized (DI) water (18.2 M Ω •cm) was produced from a Millipore water purification system. All DNA sequences were synthesized by Integrated DNA Technology (Coralville, IA). The sequences of DNA were as follows:

Probe 1 (A₁₀P1): 5'-HS-(CH₂)₆-A₁₀-GGTTGTGTTTCGTGTGC-3'

Probe 2 (A₁₀P2): 5'-HS-(CH₂)₆-A₁₀-GCTCTCGTTCTCTTCC-3'

2.2. Instruments.

UV-Vis absorption measurements were performed with a PerkinElmer Lambda 1050 UV/Vis/NIR spectrometer (PerkinElmer, Santa Clara, CA), equipped with a Peltier temperature control accessory. Transmission electron microscopy (TEM) images of ssDNA modified AuNPs were acquired by Hitachi 7500 transmission electron microscope (Hitachi, Japan).

A ThermoFisher iCAP Q ICP-MS (Waltham, MA, U.S.A) equipped with a microflow perfluoroalkoxy nebulizer and a quartz cyclonic spray chamber cooled to 2.70 °C, was used to monitor the ICP-MS signals of AuNPs. The sample solution was introduced into the ICP-MS using a peristaltic pump operating at 20 rpm and with PVC peristaltic pump tubing of 0.508 mm i.d (ThermoFisher, Waltham, MA, U.S.A) yielding a normal flow rate of 0.2 mL/min. The exact sample flow rate was measured daily by

mass of DI water. The ICP-MS instrument was tuned daily using a multi-element solution (1µg/L In, U, and Ce in 2.5 % (v/v) HNO₃) for maximum ¹¹⁵In, ²³⁸U and minimum ¹⁴⁰Ce¹⁶O/¹⁴⁰Ce level (<3.0 %) under high-sensitivity standard mode. The isotope ¹⁹⁷Au signal in counts was measured with a dwell time of 5 ms and a total acquisition period of 180 s, including 36,000 individual measurements. The ICP-MS instrument operating parameters are shown in Table 1. Data evaluation was performed with the Microsoft Excel Worksheet and Origin (Northampton, Massachusetts, USA). Measurements above 5 counts, which was five-times the highest signal intensity in blank solution, was the nanoparticle detection criterion used in this work.

Table 1. Instrument parameters used for spICP-MS measurements

Parameters	Value
Radio Frequency Power (W)	1550.00
Cool Gas (L min ⁻¹)	14.00
Sample Gas Flow (L min ⁻¹)	0.20
Nebulizer Gas Flow (L min ⁻¹)	1.19
Spray Chamber Temperature (°C)	2.70
Sampling Depth	5.00
Peristaltic Pump Speed (rpm)	20.00

The procedure followed EPA method 7473 (Feb. 2007 Revision 0) for determination of mercury in solids and liquids by thermal decomposition, amalgamation, and atomic absorption spectrophotometry. All measurements were performed with a Milestone DMA-80 Tri Cell direct mercury analyzer (Shelton, CT) equipped with a 40-position auto-sampler. Liquid samples were weighed to 0.1 mg in quartz sample boats and placed on the auto-sampler spindle. Samples were individually dried and then decomposed under the flow of regulated oxygen carrier gas. An amalgamator was used to trap the elemental mercury after which the trap was rapidly heated and mercury vapor was carried sequentially through three quartz cells positioned in the light path of atomic absorption spectrophotometer. Transient absorbance of mercury was measured at 253.7 nm for each cell and related back to mercury

concentration in the sample by external calibration over three ranges. Specific instrument operating parameters are listed in Table 2.

Table 2. DMA-80 conditions used for Hg determinations of aqueous samples.

Parameters	Value
Carrier gas	High purity oxygen at 5 psi
Furnace 1, drying	70 s at 250 °C
Furnace 1, decomposition	180 s at 650 °C
Furnace 2, catalyst	565 °C
Furnace 3, amalgamator	N/A
Furnace 4, cells	120 °C
Max. Start-T	250 °C
Purge Time	60 s
Amalgamator Heater Time	12 s
Recording Time	30 s

2.3. Preparation of ssDNA Modified AuNPs.

Thiol-functionalized ssDNA (SH-ssDNA) (100.0 μ L of 200.0 μ M) was first reduced in the same volume of TCEP (20.0 mM), and incubated for 2 h at room temperature. The amount of ssDNA was quantified with UV-Vis spectrometry. The modification of ssDNA onto AuNPs was performed according to the literature with a slight change.²⁶ Briefly, the reduced SH-ssDNA (10.0 μ L of 100.0 μ M) was mixed with 1 mL of 330 pM 30-nm-diameter AuNPs under vortexing for 1 min and left to rest for 30 min at room temperature. Afterward, an aliquot of 100.0 μ L of 100 mM citrate-HCl buffer pH 4.3 was added to adjust the pH of the solution and incubated for another 30 min, followed by adding 10.0 μ L of 300 μ M TOEG6. After another 30 min static incubation, the solution was centrifuged at 6000 rpm for 30 min. The precipitates were collected and washed with DI water twice. The final pellet was re-dispersed in 1.0 mL of DI water and store at 4 °C for further usage.

2.4. Detection of Hg²⁺ Using spICP-MS.

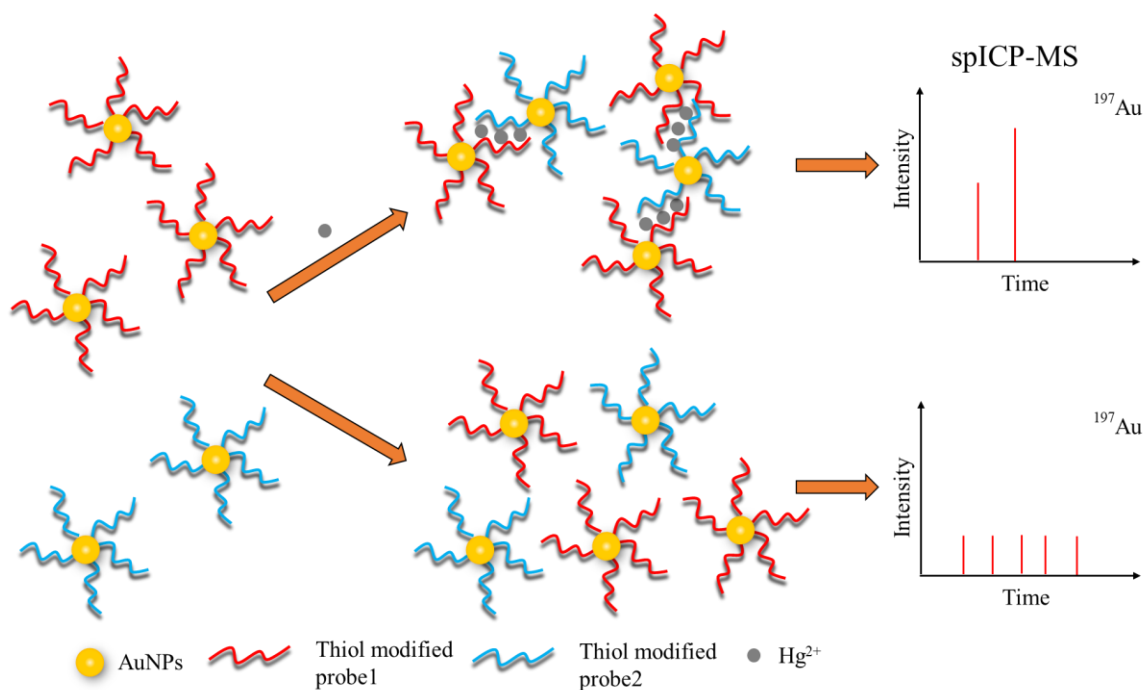
The prepared ssDNA modified AuNPs (AuNP-A₁₀P1 and AuNP-A₁₀P2) were first diluted to 10⁸ particles/mL (1.65 pM) with 10 mM PB buffer containing 300 mM

NaCl, pH 7.4. The particle number concentration of both ssDNA modified AuNPs were diluted to 10^6 , 10^7 , 10^8 , 10^9 , and 10^{10} particles/mL, respectively, during the optimization of particle number concentration. Aliquots of 90 μL of AuNP-A₁₀P1 and 90 μL of AuNP-A₁₀P2 were mixed, followed by adding 20 μL of different concentration of Hg²⁺ solution. After that, the mixture was heated up to 95 °C for 5 min and then cooled to room temperature. Then, the mixture was incubated for 2 h with constant shaking to finish the reaction. An aliquot of 0.2 μL of Tween 20 was added and incubated in an ultrasonic water bath for another 5 mins. Finally, the solution was diluted to 5×10^4 particles/mL of AuNPs before introducing into spICP-MS.

3. Results and Discussion

3.1. Detection of Hg²⁺ Using spICP-MS.

In this study, a new strategy for highly sensitive and selective detection of Hg²⁺ ion was established by using spICP-MS to monitor the agglomeration of monodisperse AuNPs by T-Hg²⁺-T pairing of ssDNA on the AuNPs surfaces. As illustrated in Scheme 1, T-rich ssDNA probes (A₁₀P1 or A₁₀P2) were individually immobilized onto the surface of different AuNP samples. The two probes are complementary except for seven mismatched T bases. In the absence of Hg²⁺, the affinity between the two probes is too weak to cause binding at room temperature, which is much lower than their melting temperature. However, in the presence of Hg²⁺, the T-Hg²⁺-T interaction will increase the melting temperature of formed dsDNA between two probes, causing the aggregation of a portion of the AuNPs. The higher the concentration of Hg²⁺, the greater the degree of aggregation, which can be easily distinguished by spICP-MS measurements of detected particle frequency and ¹⁹⁷Au counts intensity.



Scheme 1. Schematic illustration of Hg^{2+} detection using probe modified AuNPs by spICP-MS.

3.2. Synthesis of AuNP-ssDNA.

Immobilization of ssDNA on AuNPs was proven by UV-Vis spectroscopy. Compared with the bare AuNPs, the plasmon resonance peak of AuNPs modified with ssDNA (A₁₀P1 or A₁₀P2) was red-shifted to 530 nm from 526 nm (Figure 1A). Meanwhile, a new peak at 260 nm also demonstrated the immobilization of ssDNA on the AuNPs. After adding 10 ppm of Hg^{2+} , aggregation of modified AuNPs was demonstrated by a significant redshift and broadening of the UV-Vis plasmon peak (Figure 1B). The successful immobilization of ssDNA on the AuNPs was also confirmed by gel electrophoresis with which the movement of AuNPs can be tracked by the red AuNP color. As shown in Figure 1C, AuNPs modified with ssDNA (lanes 2-4) moved at a relatively fast speed which was aided by the negatively charged ssDNA. Bare AuNPs in lane 1 moved more slowly than the modified AuNPs. The AuNPs-ssDNA sample aggregated by Hg^{2+} in lane 5 showed a tailed band and moved much slower than the bare AuNPs due to their increased size after aggregation.

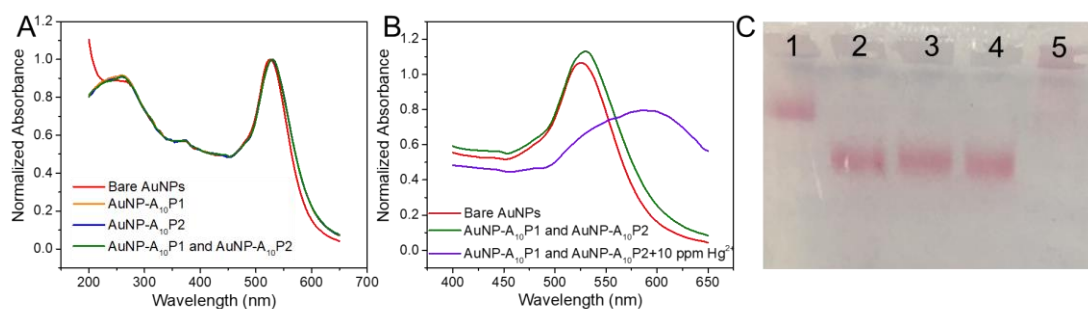


Figure 1. Characterization of AuNP-ssDNA composites. A, UV-Vis spectra of bare and AuNPs modified with ssDNA; B, UV-Vis spectra of AuNP-ssDNA with or without 10 ppm Hg^{2+} in water; C, Electrophoresis gel image of AuNP-ssDNA: Lane 1 with bare AuNPs, Lane 2 with AuNP-A₁₀P1 conjugate, Lane 3 with AuNP-A₁₀P2 conjugate, Lane 4 with AuNP-A₁₀P1 conjugate and AuNP-A₁₀P2 conjugate, Lane 5 with AuNP-A₁₀P1 conjugate and AuNP-A₁₀P2 conjugate + 10 ppm of Hg^{2+} .

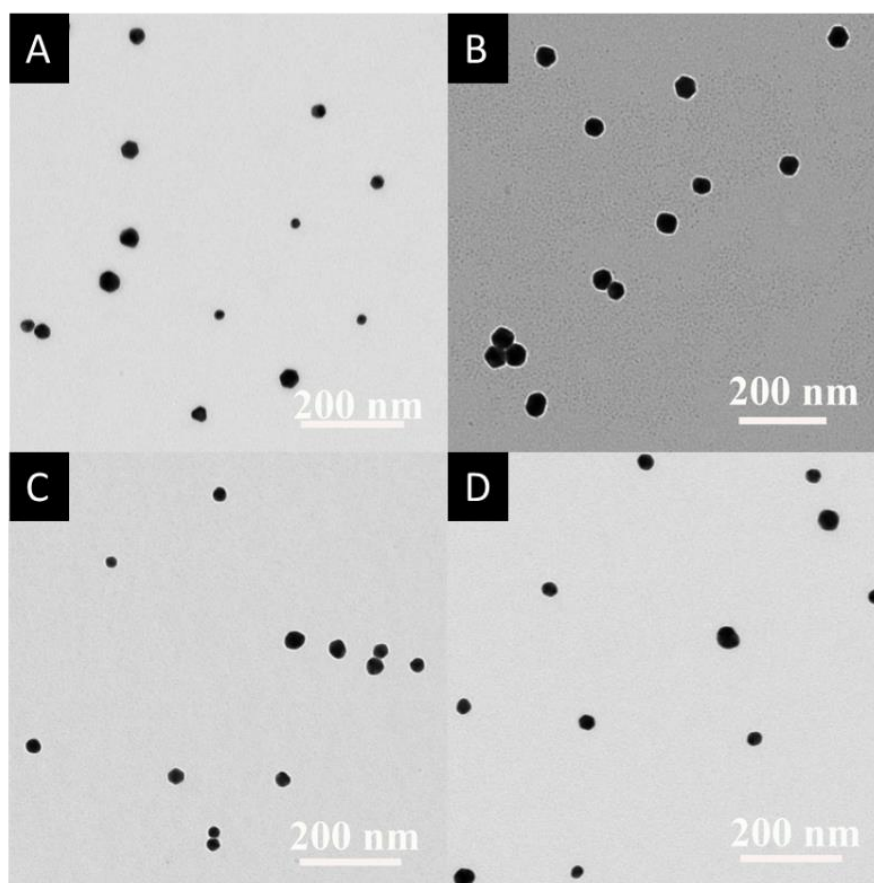


Figure 2. TEM image of AuNPs modified with ssDNA. A, bare AuNPs; B, AuNP-A₁₀P1 conjugate; C, AuNP-A₁₀P2 conjugate; D, AuNP-A₁₀P1 conjugate and AuNP-A₁₀P2 conjugate.

The size and stability of AuNPs modified with ssDNA were also characterized by TEM. As shown in Figure 2A-C, monodispersed AuNPs with the size of 32 ± 5 nm

were observed no matter which ssDNA probe was immobilized. Even in the mixture of AuNP-A₁₀P1 conjugate and AuNP-A₁₀P2 conjugate, the particles remained monodisperse in the absence of Hg²⁺ (Figure 2D), indicating excellent selectivity of the aggregation process.

3.3. Feasibility Investigation.

To demonstrate the feasibility of Hg²⁺ detection by the proposed method, the capacity of spICP-MS quantify aggregation of AuNPs was investigated. It was expected that aggregation of AuNPs would decrease the number of detected nanoparticles within the acquisition period but increase the count intensity of the ones that were detected. To prove this hypothesis, AuNPs with different sizes and different concentrations were analyzed by spICP-MS (Figure 3). As shown in Figure 3A-D, AuNPs of 20 nm, 30 nm, 40 nm, and 60 nm showed peaks with different intensities. The average intensities of the samples increased from 18.1 ± 0.8 to 450 ± 20 counts with the increase of AuNPs size ranging from 20 nm to 60 nm. In spICP-MS, the peak intensity is proportional to the numbers of Au atoms reading the plasma in one dwell time. The larger the size of the AuNPs, the higher the peak intensity (Figure 4A). This relationship demonstrated that Au atom changes caused by aggregation should be easily detected by the spICP-MS. To evaluate changes to the number of detected AuNPs, 30 nm AuNPs with different concentrations were analyzed in spICP-MS as well. As shown in Figure 3E-F and Figure 4B, 30 nm AuNPs with increasing particle concentrations of 1×10^4 , 2×10^4 , 5×10^4 and 1×10^5 particles (P) /mL increased the number of peaks (i.e., detected AuNPs) during the same acquisition period. This relationship demonstrated that the smaller number of particles resulting from the aggregation should be easily detected by spICP-MS. Therefore, spICP-MS should be a powerful tool for quantification of Hg²⁺ by monitoring Hg²⁺ induced aggregation of AuNPs.

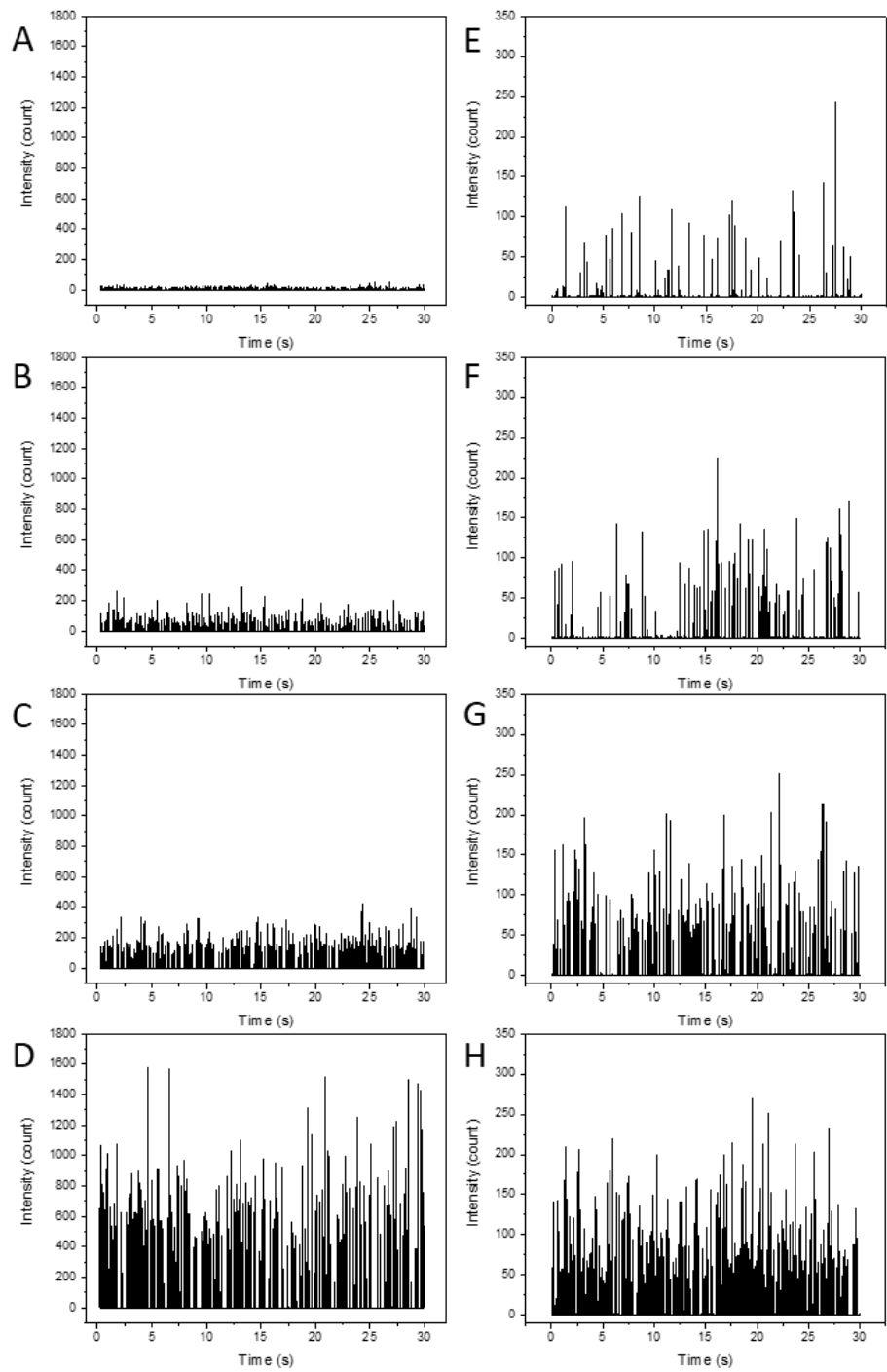


Figure 3. A-D, spICP-MS spectra of AuNPs with different sizes (A: 20 nm, B: 30 nm, C: 40 nm, D: 60 nm); E-F, spICP-MS spectra of 30 nm-AuNPs at different concentrations (E: 1×10^4 particles(P)/mL, F: 2×10^4 P/mL, G: 5×10^4 P/mL, H: 1×10^5 P/mL.). (^{197}Au , dwell time: 5ms)

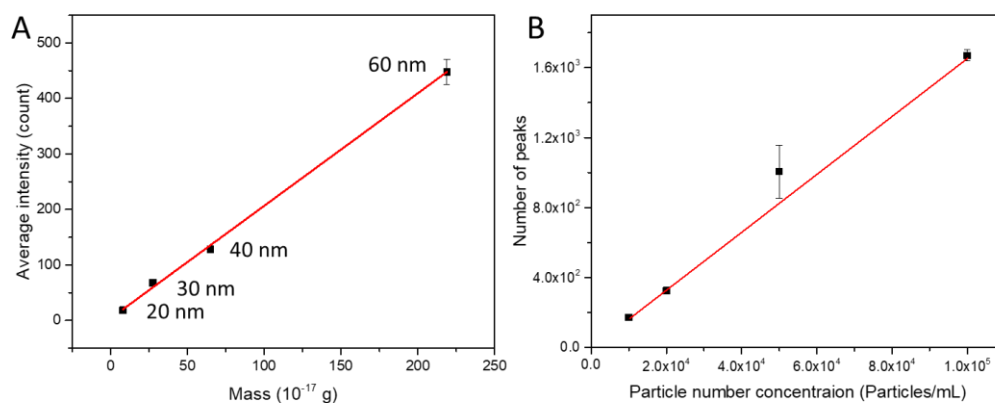


Figure 4. A, Relationship between average peak intensity and AuNPs mass in different sizes (20, 30, 40 and 60 nm); B, Relationship between number of peaks and 30 nm AuNPs concentration collected in 180 s acquisition period (10^4 , 2×10^4 , 5×10^4 and 10^5 P/mL).

The binding affinity of Hg^{2+} and thymine group was affected by the concentration of NaCl in the buffer system. However the high concentration of NaCl will cause aggregation of AuNPs.²⁷ By using TOEG6 during the ssDNA modification, the AuNPs-ssDNA can be stable in high concentration (up to 3 M) of NaCl.²⁶ We investigated the stability of prepared AuNP-ssDNA, whether it was individual (AuNP-A₁₀P1 or AuNP-A₁₀P2) or mixture, using spICP-MS with high salinity. As shown in Figure 5, the peak intensities recorded for modified AuNPs in PB buffer with 1 M NaCl (Figure 5D-F), which is much higher than the NaCl concentration used in binding buffer (300 mM), was as identical as that in PB buffer without NaCl (Figure 5A-C). No unusually high peaks were observed might indicate aggregated AuNPs. The average number of AuNPs detected during the same acquisition period were also same to that in PB buffer without NaCl. The results demonstrated that the AuNP-ssDNA conjugates could keep monodispersed in a relatively high concentration of NaCl.

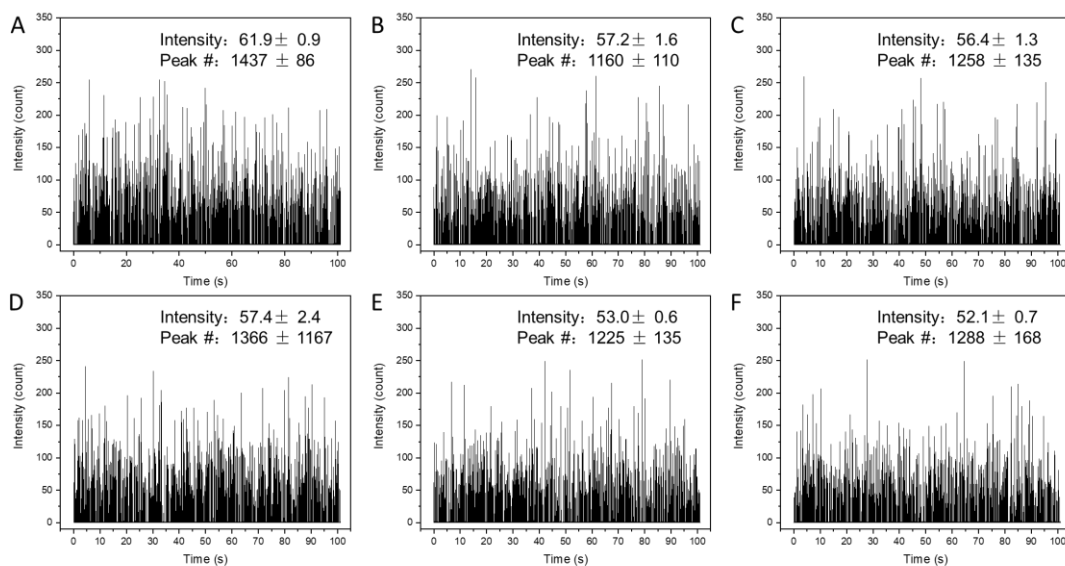


Figure 5. spICP-MS spectra of AuNP-ssDNA in 10 mM PB buffer pH 7.4 without (A, AuNP-A₁₀P1; B, AuNP-A₁₀P2; C, AuNP-A₁₀P1 and AuNP-A₁₀P2) or with (D, AuNP-A₁₀P1; E, AuNP-A₁₀P2; F, AuNP-A₁₀P1 and AuNP-A₁₀P2) 1 M NaCl. (¹⁹⁷Au, dwell time: 5ms).

3.4. Optimizations.

To optimize the aggregation of ssDNA-modified AuNPs for Hg²⁺ analysis by spICP-MS, a general method for preparing sample was developed (described in Experimental section 2.3) and a dimensionless metric for assessing the amount of aggregation was defined. Feasibility experiments demonstrated that both the number and average peak intensity AuNPs detected within the spICP-MS acquisition period (180 s) would change with the amount of aggregation. Because the change in particle number was much greater than for average peak intensity, especially at low Hg²⁺ concentrations, the dimensionless aggregation efficiency (γ) in Eq 1 was used for optimizations.

$$\gamma = 1 - \frac{\text{number of AuNPs detected after Hg}^{2+}\text{ exposure}}{\text{number of AuNPs detected before Hg}^{2+}\text{ exposure}} \quad \text{Eq 1}$$

As shown in Figure 6A, with decreasing of the particle number concentration from 10¹⁰ to 10⁶ P/mL, the aggregating efficiency first increased to the maximum at 10⁸ P/mL and then decreased. Because at high concentrations (10⁹ and 10¹⁰ P/mL), the

change of particle numbers induced by aggregation may be negligible compared to the plentiful of original particles. At low concentrations (10^6 and 10^7 P/mL), the opportunity of collision between two nanoparticles significantly decreased, causing the low aggregating efficiency. To achieve the best result, 10^8 P/mL of AuNPs-DNAs was chosen as the optimal working condition.

The T-Hg²⁺-T interaction occurred between ssDNA modified AuNPs is sensitive to the change of temperature, so the effect of incubation temperature and time were studied as shown in Figure 6B and 6C, respectively. Aggregating efficiency increased and reached a plateau from 25 °C to 35 °C. After that, the temperature was closer to the melting temperature of dsDNA and induced the dissociation of T-Hg²⁺-T between Hg²⁺ and ssDNA. Because the aggregating efficiency was constant from 25 °C to 35 °C, 30 °C was chosen for further application. Incubation time was also found to have a plateau, so that optimum conditions of 2 h at 30 °C were selected for further testing.

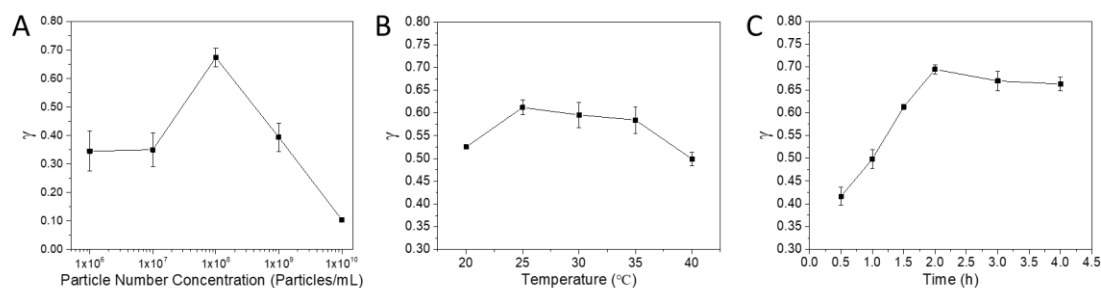


Figure 6. The optimizations of AuNPs particle number concentrations (A), incubation temperature (B), and incubation time (C). Hg²⁺ concentration: 1 ppb.

3.5. Characteristics of Hg²⁺ Analysis Method.

Analytical performance of the spICP-MS method was evaluated by applying the previously optimized aggregation conditions over a 10^8 range of Hg²⁺ concentration; from 0.01 parts per trillion (ppt, ng Hg/L) to 10,000 parts per billion (ppb, μg Hg/L).

Raw spICP-MS data for only 20 s of the 180 s acquisition period are shown in Figure 7. These data demonstrated fewer peaks but an increased number of larger peaks with higher Hg^{2+} concentration, thereby confirming the aggregation model proposed in Scheme 1. TEM images of the same samples (Figure 8) also confirmed greater aggregation of AuNPs with higher mercury level. Plots of aggregation efficiency (γ) and average peak intensity versus Hg^{2+} concentration (Figures 9, and 10, respectively) also confirmed these characteristics quantitatively. The average peak intensity increased significantly at higher mercury levels, but the increase was accompanied by unacceptably large variations from sample-to-sample and changes at low mercury levels that were too small to provide adequate sensitivity. Aggregation efficiency proved to be far better quantitative metric for Hg^{2+} calibration and determination. It showed an extremely wide dynamic range covering almost the entire 10^8 range that was tested. Moreover, the change in γ was purely logarithmic between 0.1 to 1000 ppt (line in Figure 9, $\gamma = 0.137 \cdot \text{Log}[\text{Hg}^{2+}] + 0.720$, $R^2 = 0.994$) making calibration straight forward and allowing an estimate of limit of detection ($\text{LOD} = 0.031$ ppt) from the measured variance of aggregation efficiency ($\sigma = 0.021$) in the absence of mercury (i.e., when $\gamma = 0$) and applying a detection criterion of $\gamma = 3\sigma$. Overall, this method for Hg^{2+} detection exhibited the outstanding advantages in a linear range and detection limit (Table 3).

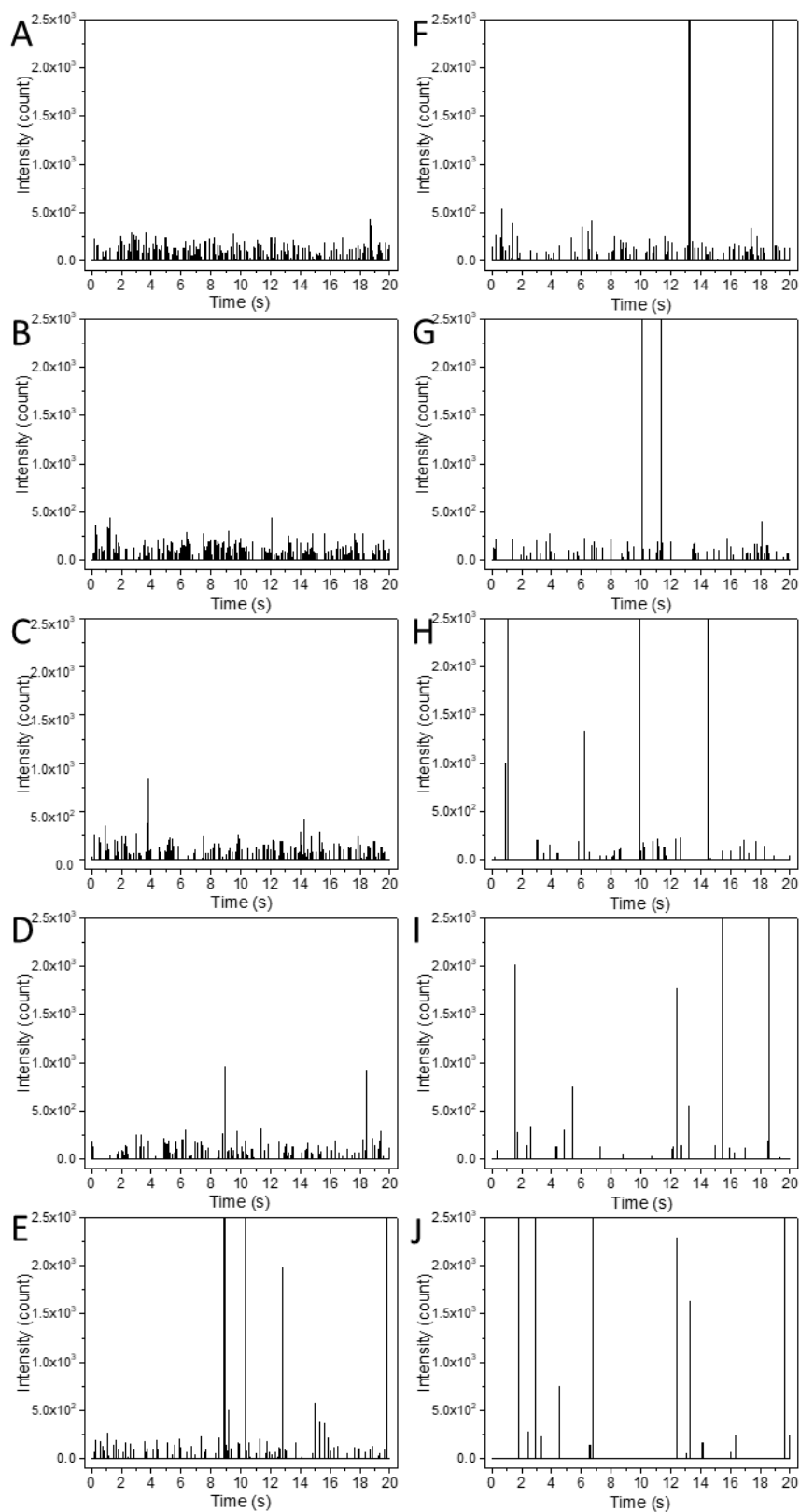


Figure 7. spICP-MS spectra of AuNP-ssDNA in the presence of different concentrations of Hg^{2+} . A, without Hg^{2+} ; B-K, Hg^{2+} concentrations in 0.01 ppt, 0.1 ppt, 1 ppt, 10 ppt, 100 ppt, 1 ppb, 10 ppb, 100 ppb, 1 ppm. (^{197}Au , dwell time: 5ms)

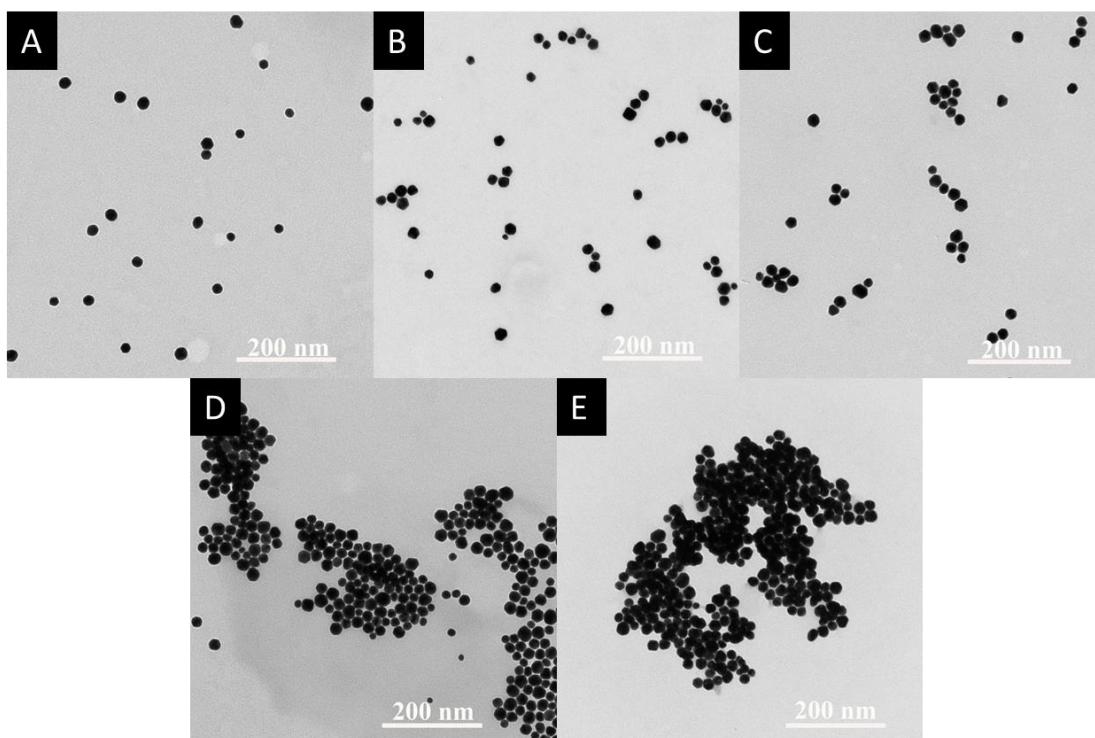


Figure 8. TEM image of AuNP-ssDNA in the presence of different concentrations of Hg^{2+} . A, AuNPs-ssDNA without Hg^{2+} ; B-E, AuNPs-ssDNA with Hg^{2+} in 10 ppb, 100 ppb, 1 ppm, 10 ppm.

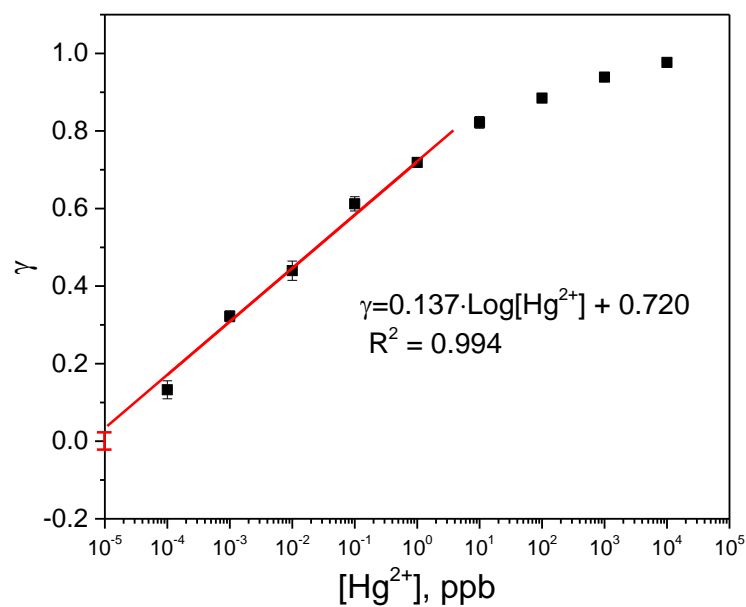


Figure 9. Relationship between aggregation efficiency and Hg^{2+} in concentration from 0.1 ppt to 10 ppm. Linear range from 0.1 ppt to 1 ppb.

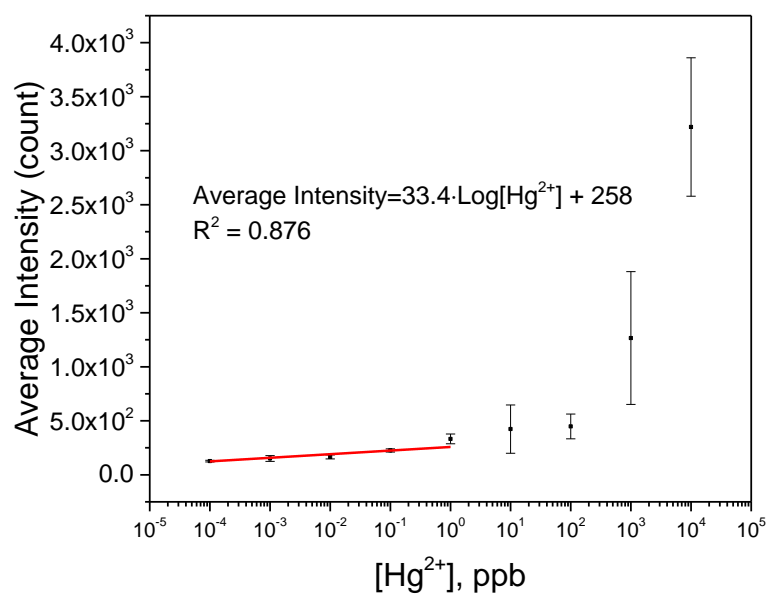


Figure 10. Relationship between average intensity and Hg^{2+} in concentration from 0.1 ppt to 10 ppm. Linear range from 0.1 ppt to 1 ppb.

Table 3. Comparison of AuNPs for Hg^{2+} detection based on aggregation strategy.

Methods	Materials	LOD	Linear range	Strategy	References
Colorimetric	AuNPs, APTES	10 nM	0-92.3 nM	Aggregation, APTES	[28]
Colorimetric	AuNPs, DNA	1 nM	1 nM-0.5 μM	Aggregation, NaCl	[29]
Fluorescence	AuNPs, DNA	16 nM	0.02-1 μM	Quench, T- Hg^{2+} -T	[12]
Colorimetric	AuNPs, CDs	7.5 nM	10-300 nM	Aggregation, CDs	[30]
Colorimetric (LFA)	AuNPs, DNA	1.5 ppt (7.5 pM)	0-2 ppb (10 nM)	Aggregation, T- Hg^{2+} -T	[31]
Localized surface plasmon resonance (LSPR)	AuNPs, DNA	0.7 nM	1-50 nM	Aggregation, T- Hg^{2+} -T	[32]
Colorimetric (paper-based)	AuNPs, DNA	50 nM	25-100 nM	Aggregation, NaCl	[33]
Colorimetric & Fluorescence	AuNPs, DNA	0.1 nM	0.2-100 nM	Aggregation, NaCl	[34]
Colorimetric	AuNPs, DNA, Polymer	0.15 nM	0.25-500 nM	Aggregation, Polymer	[35]
spICP-MS	AuNPs, DNA	0.031 ppt (155 fM)	0.1 ppt (500 fM)-1 ppb (5 nM)	Aggregation, T- Hg^{2+} -T	This work

3.6. Selectivity.

The selectivity of AuNP-ssDNA aggregation for Hg^{2+} was also evaluated using the spICP-MS method. AuNP-ssDNA mixtures were incubated with other environmentally relevant metal ions, including Pb^{2+} , Cd^{2+} , Ni^{2+} , Mn^{2+} , Cu^{2+} , Fe^{2+} , Mg^{2+} , Zn^{2+} , Ca^{2+} , Al^{3+} , and Fe^{3+} at a concentration of 100 ppb, which were 100 times higher than the concentration of Hg^{2+} used for comparison (1 ppb). The results in Figure 11 demonstrated that the AuNP-ssDNA probe aggregated very selectively with Hg^{2+} compared to the other bivalent or trivalent metal ions. Despite the concentration of other ions being 100-fold higher, none showed an aggregation efficiency higher than 30% of that for Hg^{2+} .

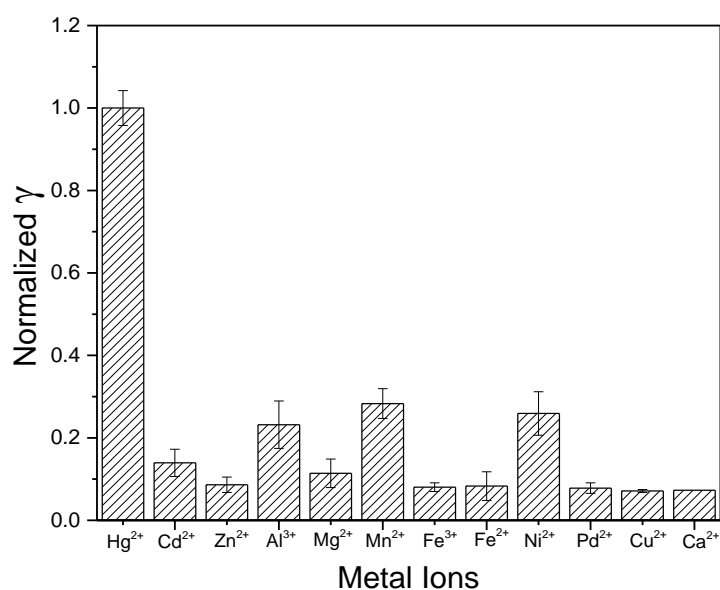


Figure 11. Selectivity of the AuNP-ssDNA probe for Hg^{2+} detection by spICP-MS. Hg^{2+} concentration: 1 ppb; other ion concentrations: 100 ppb.

3.7. Analysis of Real Sample.

To validate the optimized spICP-MS method for determination of Hg^{2+} in real samples, both tap water and river water samples were spiked with varied levels of

mercury (1 ppt and 1 ppb) and tested. The spICP-MS testing was performed in parallel with the standard EPA method 7473 and the spike recovery results were compared (Table 4). Although lower spike level (1 ppt) was below the detection limits of the standard method, the results for the higher spike level (1 ppb) showed good correspondence between the two methods and acceptable recoveries ($100 \pm 20\%$). It is noteworthy that the spICP-MS method demonstrated acceptable Hg^{2+} recoveries at both concentration levels.

Table 4. Spike recovery efficiency of spICP-MS method for Hg^{2+} detection in the tap water and river water(n=3).

Samples	Spiked (ppb)	Found by spICP-MS (ppb)	Recovery of spICP-MS (%)	Found by DMA (ppb)	Recovery of DMA (%)
Tap water	1.00×10^{-3}	$(1.05 \pm 0.13) \times 10^{-3}$	105 ± 13	a	-
	1.00	0.88 ± 0.18	88 ± 18	1.16 ± 0.06	115 ± 6
River water (Red river)	1.00×10^{-3}	$(1.09 \pm 0.22) \times 10^{-3}$	109 ± 22	a	-
	1.00	0.90 ± 0.07	90 ± 7	1.15 ± 0.01	112 ± 1

^a The concentration of Hg^{2+} was too low to be detected by DMA

4. Conclusions

This work developed a method for the determination of Hg^{2+} using aggregation of DNA modified AuNPs and measurement of that aggregation by spICP-MS. Because of the strong and highly specific “T- Hg^{2+} -T” interactions between modified AuNPs, the method achieved outstanding sensitivity and selectivity. The optimized assay provided a 10^8 dynamic range and a broad logarithmic range from 0.1 ppt to 1 ppb, and a detection limit of 0.031 ppt. These characteristics are superior to most other reported mercury assays. Moreover, this assay demonstrated an accurate analysis of Hg^{2+} in tap water and river water with satisfactory recovery results. The developed assay provided promising potential for the detection of other metal ions and biomolecules by carefully designing the probes on AuNPs.

CHAPTER II

AN ULTRASENSITIVE GOLD NANOPARTICLE BASED GRAPHENE BIOSENSING PLATFORM USING SINGLE PARTICLE INDUCTIVELY COUPLED PLASMA MASS SPECTROMETRY

1. Introduction

Graphene oxide (GO) has been widely applied to fabricate fluorescence biosensors due to its unique optical properties.³⁶⁻³⁷ In general, it is a high capacity energy acceptor and has played a significant role as a quencher in the fluorescence resonance energy transfer (FRET) of optical biosensors.³⁸⁻³⁹ For instance, single-stranded DNA (ssDNA) is easily adsorbed to the GO surface because of strong π - π stacking interactions between the base structure of ssDNA and the two-dimensional multi-hexagonal structure of GO.⁴⁰ The strong adsorption between GO and ssDNA, coupled with the excellent quenching ability of GO provides an effective fluorescence platform for sensing biomolecules.⁴¹ Two major factors determine the sensitivity of DNA-sensing applications of this platform. The first factor is a target-induced DNA conformational change, which results in desorption of fluorophore molecules away from the GO, and thus increased fluorescence signals. Since the first report by Zhang *et al.* in 2009,⁴¹ a broad range of targets including nucleotides,⁴² metal ions,⁴³ proteins,⁴⁴ enzymes,⁴⁵ and other small molecules⁴⁶ have been detected using various ssDNA conformational changes with this platform.⁴⁷ The second factor is the signal output based on the FRET effect between fluorophore molecules and the GO. However, the high background signal in some complex samples,⁴⁸ photobleaching of fluorophores, and the practical limitations of fluorophotometers has prevented further improvement in sensitivity to achieve sub-picomolar detection. Thus, a better signal output method is needed.

Two possible strategies could improve the signal output of the GO platform.

The first strategy is to introduce an amplification step in the sensing process.⁴⁹ For instance, several methods have been applied for oligonucleotide amplification, such as polymerase chain reaction and other isothermal nucleic acid amplification methods.⁵⁰ However, specific enzymes and delicate sequence design were required, diminishing assay feasibility. The second strategy is to utilize a more sensitive detector. One candidate is the inductively coupled plasma-mass spectrometry (ICP-MS) when operated in the time-resolved mode with ultrashort dwell time. This configuration has demonstrated encouraging results for nanoparticle analysis and is often referred to as single particle ICP-MS (spICP-MS).²²⁻²⁴ The method provides “particle by particle” measurements that include information about particle number concentration, particle size, and size distribution.²⁴ Each particle that enters the ICP plasma forms an ion cloud that results in an isotope count registered by the MS during a single dwell time measurement. Theoretically, single particle in the solution can be detected if 100 % transportation efficiency and enough collection time were applied.⁵¹⁻⁵² Although most spICP-MS applications to date have been focused on the characterization and direct quantification of nanoparticles themselves,⁵³⁻⁵⁴ the capacity for ultralow detection of the particle concentration also makes spICP-MS a promising tool for ultrasensitive bioassay.^{25, 55} Zhang *et al.* developed a multiple DNA assay using different isotopes of nanoparticles as the output signal. The nanoparticles were first captured by the heterogeneous sandwich structure and then melted and washout into the ICP-MS. The nanoparticle concentration quantified by spICP-MS was proportional to the concentration of the target.⁵⁶

Considering the criteria for the ultrasensitive detection,⁴⁹ which used to describe the sensors with an ultralow detection limit (sub-picomolar), the demands of ultrasensitive detection ultralow concentrations of biomarkers, such as bloodborne

viruses, circulating tumor cells, and circulating nucleic acids,⁵⁷ might be met by using the spICP-MS as the signal output system. Based on this hypothesis, in this work, we have developed an ultrasensitive graphene platform for sensing biomolecules using gold nanoparticles (AuNPs) and spICP-MS technology. Thrombin, a kind of serine protease that plays a crucial role in blood coagulation and thrombotic diseases, was chosen as the model target biomolecules of study. We fabricated a sensing platform based on the GO/DNA recognition and spICP-MS detection to detect thrombin. An ultralow detection limit of 4.5 fM was archived by the combination of excellent recognition ability of GO for ssDNA and ultra-sensitivity of spICP-MS. Moreover, the diversity of ssDNA sequences on AuNPs made then an excellent building block for various targets because they can work as an aptamer or as a complementary sequence.⁵⁸⁻⁵⁹ Hence, our designed platform has potential as a broad-spectrum biosensor for ultrasensitive detection of biomarkers in clinical diagnostics.

2. Experimental Section

2.1. Materials.

Gold nanoparticles (20 nm) were purchased from Cytodiagnosics Inc (Burlington, Canada). Gold standard solution was purchased from Inorganic Ventures (Christiansburg, VA). High purity liquid argon was used as the plasma gas and the nebulizer gas for all ICP-MS measurements. In the conventional ICP-MS measurements, an ultra-high purity helium gas was used to remove undesirable molecule ions in the kinetic energy discrimination (KED mode). (11-mercaptoundecyl) hexa (ethylene glycol) (TOEG6), sodium chloride, magnesium chloride, sodium phosphate monobasic, sodium phosphate dibasic, sodium citrate tribasic dihydrate, bovine serum albumin (BSA), and 0.22 μm filter membranes were purchased from

Sigma-Aldrich (St. Louis, MO). Immunoglobulin G (IgG) was purchased from Santa Cruz Biotechnology (Dallas, TX). Fetal bovine serum (FBS) was purchased from VWR (Radnor, PA). Single layer graphene oxide was purchased from ACS Material (Pasadena, CA). The deionized (DI) water (18.2 M Ω •cm) was produced from a Millipore water purification system. All DNA sequences were synthesized by Integrated DNA Technology (Coralville, IA). The sequences of DNA used were as follows:

m29: 5'-HS-(CH₂)₆-TTTTTAGTCCGTGGTAGGGCAGGTTGGGGTGACT

m29-F: 5'-HS-(CH₂)₆-TTTTTAGTCCGTGGTAGGGCAGGTTGGGGTGACT-Alex750-3'

2.2. Instruments.

UV-Vis absorption measurements were performed on a PerkinElmer Lambda 1050 UV/Vis/NIR spectrometer (PerkinElmer, Santa Clara, CA), equipped with a Peltier temperature control accessory. Zeta potential of nanomaterials was measured using Zetasizer nano (Malvern Panalytical, UK). Fluorescence spectra were obtained with an RF-6000 spectrophotometer (Shimadzu, Japan). Transmission electron microscopy (TEM) images of GO and AuNPs were taken using a Hitachi 7500 transmission electron microscope (Hitachi, Japan). All ICP-MS measurements were carried out using a Thermo Scientific iCAP Qc ICP-MS (Bremen, Germany) coupled with a 4-channel 12-roller peristaltic pump, nickel sample and skimmer cones, a Teledyne CETAC ASX560 autosampler (Omaha, NE), a microflow perfluoroalkoxy nebulizer (Thermo Scientific) and a Peltier-cooled quartz cyclonic spray chamber. To monitor the ICP-MS instrument, the THERMO-4AREV (Thermo Scientific) standard was run daily for maximum ⁵⁹Co, ²³⁸U and minimum ¹⁴⁰Ce¹⁶O/¹⁴⁰Ce signal. The ICP-MS measurements of AuNPs were controlled by the Qtegra™ software (version

2.8.2944.202). The instrument operating parameters used for the single particle and conventional ICP-MS measurements are listed in Table 5.

Table 5. ICP-MS instrument parameters used for conventional and single-particle measurements.

Parameter	Conventional measurement	Single-particle measurement
<i>Sample introduction</i>		
peristaltic pump	4-channel, 12-roller	4-channel, 12-roller
pump speed (rpm)	20	20
sample tubing (mm ID)	0.508	0.508
internal-standard tubing (mm ID)	0.508	not used
waste tubing (mm ID)	1.295	1.295
nebulizer	Microflow PFA-ST	Microflow PFA-ST
nebulizer gas flow (L/min)	1.09	1.05
spray chamber	quartz cyclonic	quartz cyclonic
spray chamber temperature (°C)	2.70	2.70
<i>Plasma</i>		
torch	ICAP Q quartz	ICAP Q quartz
Rf power (W)	1550	1550
coolant gas flow (L/min)	14	14
plasma gas flow (L/min)	0.8	0.8
sample injector	quartz (2.5 mm ID)	quartz (2.5 mm ID)
<i>Mass spectrometer</i>		
sample cone	nickel	nickel
skimmer cone	nickel	nickel
cone insert	3.5 mm	2.8 mm
mode	KED	STDS
KED gas flow (mL/min)	4.6	0
dwel Time (ms)	50	5
sweeps	10	0
internal standards	^{103}Rh , ^{209}Bi	none

2.3. Preparation of ssDNA Modified AuNPs.

Thiol-functionalized ssDNA (SH-ssDNA) (100 μL of 200.0 μM) was reduced in the 100 μL of TCEP (20.0 mM), and then was incubated for 2 h at room temperature. The amount of ssDNA was quantified with UV-Vis spectrometry. The modification of ssDNA onto AuNPs was performed according to the literature with a slight change.²⁶ Briefly, the reduced SH-ssDNA (10 μL of 100.0 μM) was mixed with 1.0 mL of 1 OD 20-nm-diameter AuNPs under vortexing for 1 min and was retained in the container for

10 min at room temperature. Afterward, a 100 μL aliquot of citrate-HCl buffer (100 mM, pH 4.3) was added to adjust the pH of the solution and incubated for 30 min, followed by adding 50 μL of 300.0 μM TOEG6. After additional 10 min of static incubation, the solution was centrifuged at 6,500 $\times g$ for 30 min. The precipitates were collected and washed with DI water twice. The final pellet was re-dispersed in 1.0 mL of DI water and stored at 4 $^{\circ}\text{C}$ for further use.

2.4. Adsorption of ssDNA to GO.

A 50 μL aliquot of 5×10^{11} particle/mL AuNPs-ssDNA and 50 μL of 400.0 $\mu\text{g/mL}$ of GO were incubated in 1.0 mL of PBS buffer (10 mM with 0.5 mM MgCl_2 , pH 7.4) at room temperature for 30 min with regular shaking. Then the solution was vacuum filtered by a 0.22 μm membrane. After washing with water twice and PBS buffer once, the maroon-colored GO/AuNPs composites distributed on the membrane surface were re-dispersed in 2 mL of PBS buffer by using an ultrasonic water bath.

2.5. Analysis of Thrombin by GO/AuNPs Composites Using spICP-MS.

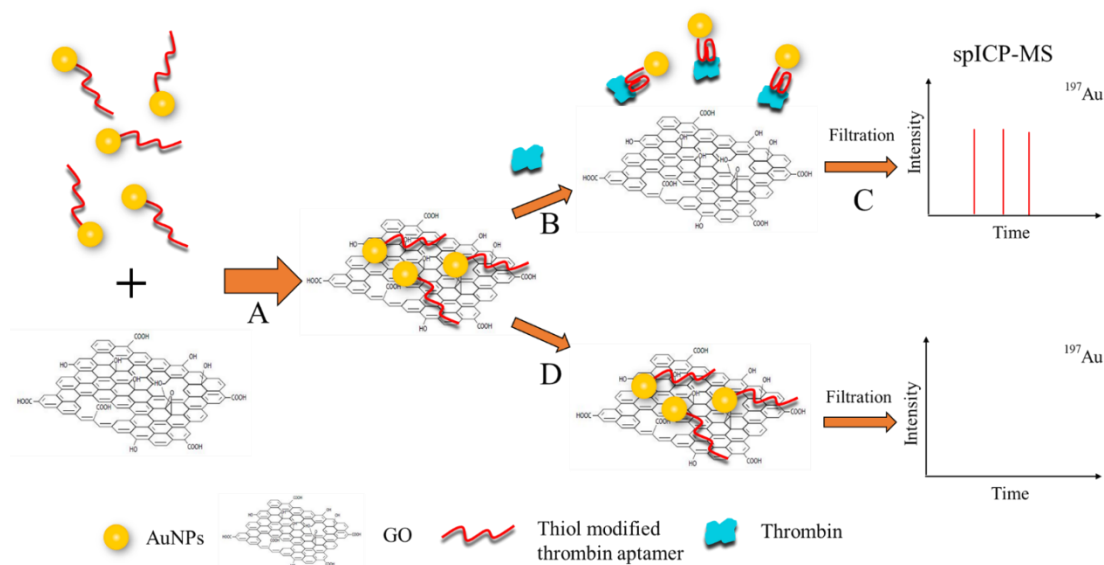
A 50 μL aliquot of thrombin solution with different concentrations were incubated with 50 μL of prepared GO/AuNPs composites in a total of 500 μL of PBS buffer (10 mM with 0.5 mM MgCl_2 , pH 7.4) at 37 $^{\circ}\text{C}$ with regular shaking. After 1 h of incubation, the solutions were removed by syringe and filtered using a 0.22 μm membrane. Followed by 10 min of ultrasonic water bathing, the filtrate would be introduced to the ICP-MS.

3. Results and Discussion

3.1. Design of the Biosensing Platform.

A new graphene-based platform for ultrasensitive detection of biomolecules was based on spICP-MS directly counting escaped AuNPs from the graphene oxide/Au

nanoparticles (GO/AuNPs) composites. The escape was caused by the reaction between the target molecule and the ssDNA ligands (aptamer) modified on the surface of AuNPs. The design of the platform is illustrated in Scheme 2. First of all, a thrombin aptamer (ssDNA sequence with specific strong affinity to thrombin) was covalently immobilized on the surface of 20 nm citrate stabilized AuNPs through the formation of an Au-S bond. After incubation with a GO sheet, the aptamer modified AuNPs were adsorbed on the surface of GO due to the strong π - π stacking interaction between the ring structures of ssDNA base and the GO sheet, thereby forming the GO/AuNPs composites (Scheme 2A). After thoroughly washing to remove any free AuNPs, the target biomolecule, thrombin, was introduced to the platform. In the presence of thrombin, aptamer on the AuNPs complexed with the thrombin molecule and changed the aptamer structure (Scheme 2B). This conformational change broke the interaction between the aptamer and the GO, causing the associated AuNPs-aptamer to desorb from the GO surface. Before introducing the solution into the spICP-MS, it was filtered to 0.22 μ m membrane to remove the AuNPs still adsorbed to GO. Only the escaped thrombin-complexed AuNPs would be injected into the ICP-MS (Scheme 2C). There were no aptamer-modified AuNPs desorbed in the absence of thrombin (Scheme 2D). In the single particle analysis mode, the number of AuNPs was absolutely quantified by counting the pulse detected. The number of pulses, related to the number of AuNPs desorbed from GO by thrombin-aptamer complexation, was directly related to thrombin concentration. Because the spICP-MS method can easily detect even small number (<100) of AuNPs per mL of solution, this designed platform has the capability to achieve ultralow detection limits for thrombin or other potential biomarkers.



Scheme 2. Schematic illustration of thrombin detection using aptamer modified AuNPs by spICP-MS. A, thrombin aptamer modified AuNPs incubated with GO; B, thrombin molecule as target incubated with GO/AuNPs composites; C, desorbed AuNPs were separated and introduced into spICP-MS; D, no thrombin molecule added as control.

3.2. Formation of GO/AuNPs Composites.

Two strategies have been applied in the graphene/DNA based fluorescence biosensors, which depend on the sequence of ssDNA adsorbed to the GO.^{42, 60} In the “turn off” mode, also named post-adsorb strategy, the target molecule was first incubated with dye modified ssDNA, then addition of GO caused fluorescence quenching after the unbound ssDNA adsorbed to the GO surface. In the “turn on” mode, also named pre-adsorb strategy, the dye modified ssDNA reagent was first adsorbed to the GO surface to quench the fluorescence. Addition of target molecules caused the desorption of dye molecules from the GO due to the interaction with ssDNA, resulting in fluorescence recovery. Considering the ultrahigh signal to noise ratio of the “turn on” mode inherent to the pre-adsorb strategy, the GO/AuNPs composites were obtained before incubation with thrombin. Unlike adsorption between dye-modified ssDNA and GO, unmodified AuNPs were easily adsorbed to GO in high ionic-strength buffers, although both were negatively charged (Figure 12). Strong van der Waals forces play a

significant role in the aggregating of AuNPs and GO by screening the charge repulsion at a high salt concentration.⁶¹ Accordingly, the moderate salt concentration is required to favor the adsorption of ssDNA to GO and avoid nonspecific adsorption of AuNPs to GO. To determine the most favorable ionic strength, the salt concentration was optimized. As shown in Figure 13, the amount of AuNPs measured in the filtrate after incubating with GO in a PB buffer was found to vary with different concentrations of Mg^{2+} or Na^+ . The difference was quantified by measuring the UV-Vis absorbance peak at 520 nm for 20 nm AuNPs. For 0.5 mM $MgCl_2$ (Figure 13A), around 100% of the AuNPs-TOEG6 (red circle, control group without ssDNA modification) was recovered in the filtrate after incubating with GO, indicated that there was no nonspecific binding between the AuNPs and GO. When the $MgCl_2$ concentration was higher than 1.0 mM, less than 70 % of the AuNPs were recovered in the filtrate. The unrecovered AuNPs were non-specifically bound to the GO surface, so these conditions should be avoided. For all $MgCl_2$ concentrations, the aptamer modified AuNPs (black squares) were easily adsorbed to the GO surface and retained. Moreover, there was no aptamer modified AuNPs left in the filtrate after incubating with GO in the buffer solution with $MgCl_2$ concentration higher than 2.0 mM. Although the adsorption efficiency was not 100 % under 0.5 mM $MgCl_2$ concentration, this concentration was optimal considering the nonspecific adsorption to the AuNPs without ssDNA. The same situation was also observed when using NaCl (Figure 13B). However, the nonspecific adsorption still existed even when the concentration of NaCl was only 10.0 mM, which was much lower than the required concentration of Na^+ for the interaction between ssDNA and GO.⁶² Therefore, PB buffer with 0.5 mM $MgCl_2$ was chosen for the incubation of aptamer modified AuNPs and GO.

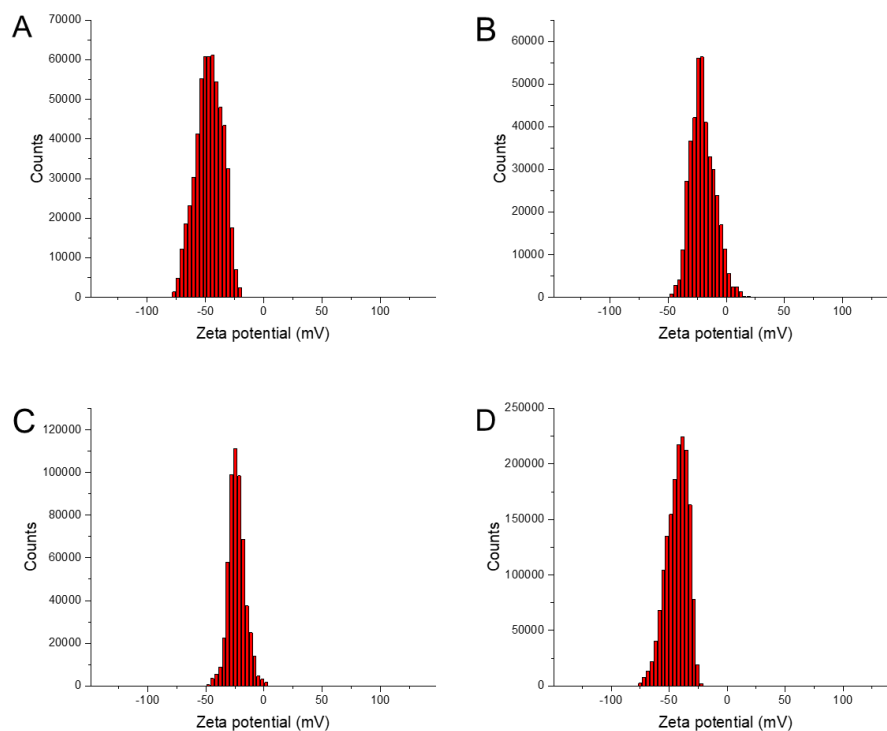


Figure 12. Zeta potential measurements of the nanomaterials. A, bare AuNPs (-43 ± 3 mV); B, AuNP-TOEG6 (-20 ± 2 mV); C, AuNP-aptamer (-26 ± 3 mV); D, GO (-43 ± 1 mV).

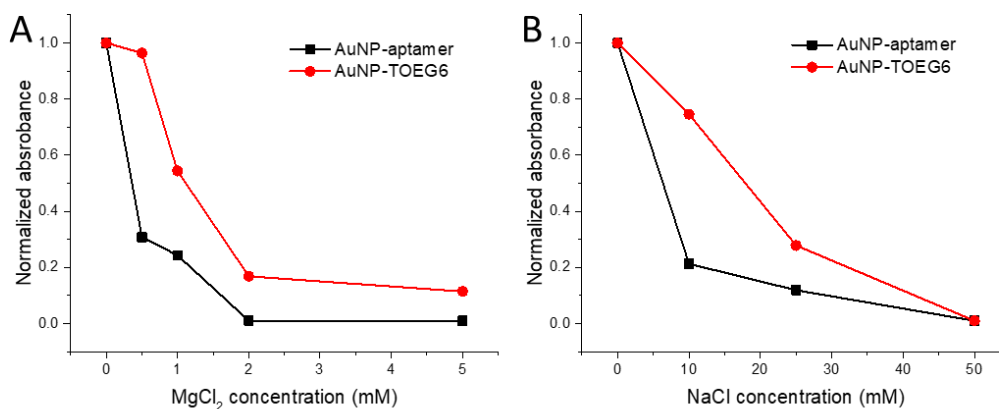


Figure 13. UV-Vis absorption of AuNPs at 520 nm with different concentration of $MgCl_2$ (A) or NaCl (B). The AuNPs were in the filtrate after incubation with GO in a PB buffer (10.0 mM, pH 7.4)

Formation of the composite was confirmed visually by 0.22 μm filtration at four stages of GO/AuNPs synthesis (Figure 14). GO was retained on the filter membrane surface (brown color) because of its larger average size (>500 nm) than the membrane pore size (0.22 μm , Figure 14A). The AuNPs-aptamer, which was only 20

nm in diameter, passed the membrane easily and no evidence of the residual AuNPs was seen on the membrane surface (Figure 14B). When the GO/AuNPs composites formed by incubation of GO and AuNPs-aptamer, the residue on the membrane was a reddish brown color, resulting from the color of AuNPs on GO (Figure 14C). The residue of the GO and AuNPs-TOEG6 (Figure 14D) was the same as the pure GO (Figure 14A), indicating no AuNPs nonspecifically adsorbed onto the GO. Formation of the GO/AuNPs composite was further confirmed by TEM images. As shown in Figure 15, the GO was present in a classic one-layer sheet structure with the size larger than 500 nm. The 20 nm AuNPs (dark spots) were evenly distributed on the GO surface. No free AuNPs existed in the area without GO, demonstrating the formation of purified AuNPs/GO composites.

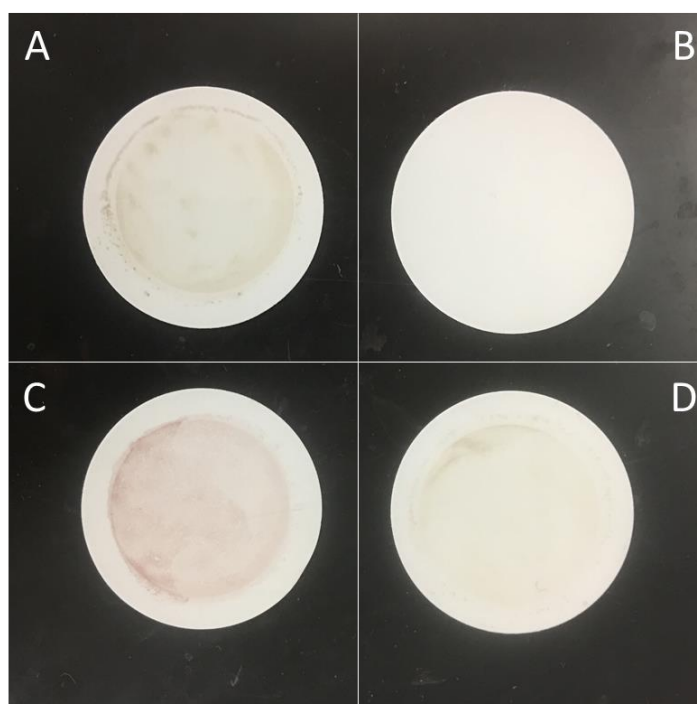


Figure 14. Photos of GO/AuNPs collected on the filter membrane surface. A, GO only; B, AuNP-aptamer only; C, GO and AuNP-aptamer; D, GO and AuNP-TOEG6. Incubated in 1.0 mL of 10.0 mM PB buffer with 0.5 mM MgCl_2 (pH 7.4) for 10 min at room temperature. The GO concentration: 20 $\mu\text{g/mL}$; AuNPs concentration: 10^{10} nanoparticles/mL.

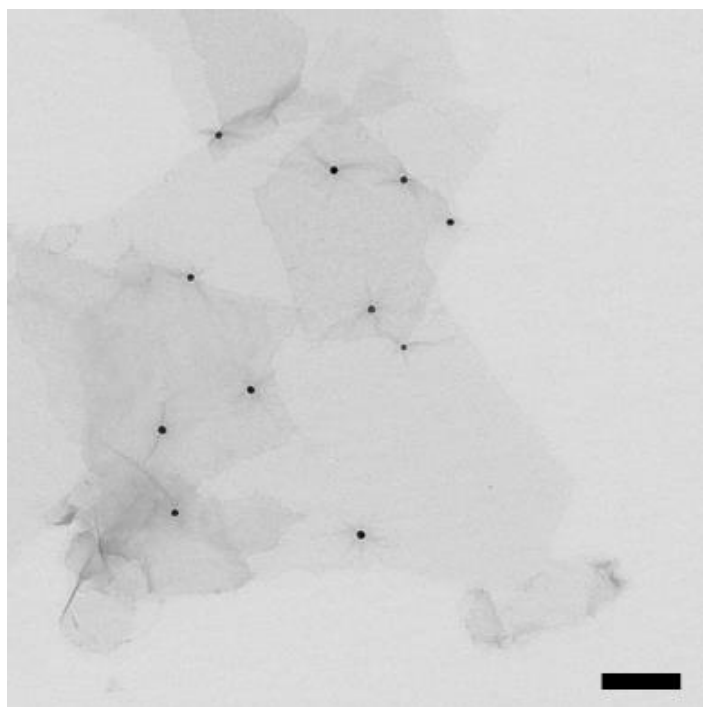


Figure 15. TEM image of the GO/AuNPs composites re-dispersed in water. The GO/AuNPs composites were obtained by incubating a 50 μL aliquot of 5×10^{11} particle/mL AuNPs-aptamer and 50 μL of 400.0 $\mu\text{g/mL}$ of GO in 1.0 mL of PBS buffer (10 mM with 0.5 mM MgCl_2 , pH 7.4) at room temperature for 30 min. Scale bar: 200 nm.

3.3. Validation of spICP-MS for Ultrasensitive Detection.

The feasibility of ultrasensitive detection of AuNPs by spICP-MS was first verified. As shown in Scheme 2, the measured signal of the method is the number of desorbed AuNPs, which is proportional to the concentration of the target molecule. Solution containing different number concentrations of standard AuNPs were tested using the spICP-MS. As shown in Figure 16, the number of pulses collected within 30 s systematically increased when the AuNP number concentration increased. The NP detection criterion applied in all measurements was signal (in counts) greater than five-times the baseline noise level. This noise level was 1 count, so a NP was detected if the signal intensity was higher than 5 counts. There were no detected NPs in the blank solution without AuNPs (Figure 16A). By increasing the particle number concentration from 100 to 100,000 particles/mL, the number of NPs detected during the 180 s

acquisition period increased from 2 to ~800 (Figure 16B-G). The relationship between the number of detected NPs and the particle number concentration was calibrated under conditions of 0.20 $\mu\text{L}/\text{min}$ flow rate and 6.45 % transport efficiency. The results showed an excellent linear fit at a low concentration range (0-10,000 particles/mL, Figure 16H inset). Hence, the number concentration of AuNPs in the solution could be absolutely quantified by using this calibration and the volume of the sample measured during the acquisition period. The number of NPs detected at high concentrations was lower than the expectation from the linear part of the calibration curve (Figure 16H). This was probably by the greater likelihood of two NPs entering the plasma within one dwell time. To avoid this issue, all the sample solutions were diluted before introducing into ICP-MS.

To demonstrate the greater capacity of spICP-MS for ultrasensitive detection of AuNPs, we compared the spICP-MS results with a conventional ICP-MS. The results are listed in Table 6. The Au detection limit using conventional mode ICP-MS was 0.005 ppb, which was calibrated using gold standard solutions. There were no Au detected by conventional ICP-MS when the particle number concentration was lower than 10^6 particles/mL. In contrast, a solution of 100 particle/mL could be easily determined using the single particle mode with only a 3 min collection time. Note that the detection limit of the spICP-MS method could be even lower if the collection time was increased.⁵¹ Moreover, the theoretical number of pulses calculated based on the literature⁵¹ was close to the experimental data, demonstrating the reliability of the method. These data demonstrated that even if only a few hundred AuNPs desorbed from GO induced by a thrombin sample, they could be easily quantified by spICP-MS. Assuming each thrombin molecule of the sample would desorb one AuNP and that each

AuNP would be detected, this analytical performance would correspond to a thrombin concentration of less than 1×10^{-18} M.

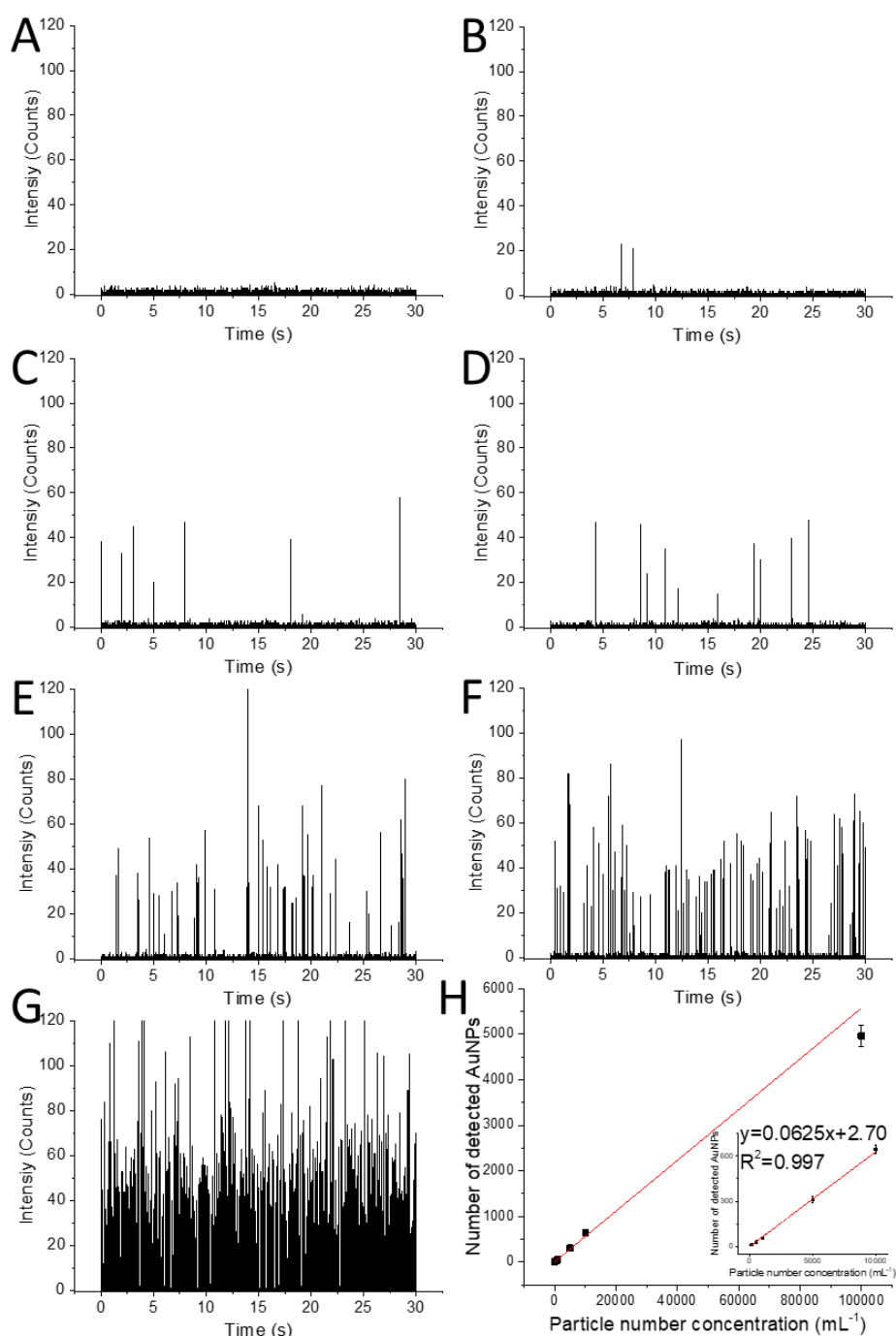


Figure 16. spICP-MS spectra of AuNPs in different particle number concentrations. A-G: 0, 100, 500, 1,000, 5,000, 10,000, and 100,000 particles/mL. (^{197}Au , dwell time: 5 ms). H. Relationship between the number of detected AuNPs and the particle number concentration from 0 to 100,000 particles/mL within 180 s collection time. Inset: Calibration curve of the number of detected AuNPs and the particle number concentration from 0 to 10,000 particles/mL.

Table 6. AuNPs particle number concentration quantified by spICP-MS and conventional ICP-MS

Particle number concentration (particle/mL)	Detected number of AuNPs	Predicted number of AuNPs*	Conventional ICP-MS (ppb) LOD: 0.005 ppb	Theoretical Concentration (ppb) [#]
100	10.5	4.05	b	8.1×10^{-6}
500	28.25	20.25	b	4.1×10^{-5}
1000	56	40.5	b	8.1×10^{-5}
5000	310.5	202.5	b	4.1×10^{-4}
10^4	645.25	405	b	8.1×10^{-4}
10^5	4957.25	4050	b	0.0081
10^6	a	40500	0.024	0.081
10^7	a	405000	0.274	0.81

*based on the following conditions: flow rate at 0.2 mL/min, collection time for 3 min, Transport efficiency at 6.45%

[#] average mass of 20 nm AuNPs: 8.1×10^{-17} g

^a too condense in spICP-MS

^b under LOD of conventional ICP-MS

3.4. Optimizations.

Unlike the dye used in the fluorescent platform, there were numerous positions on AuNPs that could be bound with ssDNA. The high loading capacity of ssDNA would strengthen the interaction between the AuNPs and the GO. Meanwhile, the AuNPs became harder to desorb in the presence of thrombin. Hence, the ssDNA density on the AuNPs, which would affect the desorption efficiency of ssDNA, was optimized prior to the detection. TOEG6, a protein-repellent alkanethiol, was used to stabilize the AuNPs by passivating the particle surface during the ssDNA immobilization. The amount of ssDNA on the AuNPs surface was tuned by changing the ratio of ssDNA to TOEG6.²⁶ The exact amount of ssDNA was quantified by measuring the decrease of fluorescence (Alex-750, modified on the other end of thrombin aptamer) in the supernatant. The ssDNA density on AuNPs at different concentrations of TOEG6 is summarized in Table 7. The higher TOEG6 concentration, the lower ssDNA density on the AuNPs. Finally, an average of one ssDNA per particle was obtained when the

TOEG6 concentration increased to 15 μM , which was 60-times higher than the ssDNA concentration. After obtaining aptamer-modified AuNPs with different numbers of immobilized ssDNA, the assay was optimized based on the number of AuNPs detected by spICP-MS. As shown in Figure 17A, the number of detected AuNPs increased with decreasing number of immobilized ssDNA, demonstrating that AuNPs with less immobilized aptamer would more easily desorb from the GO surface under the same concentration of thrombin. To achieve the best result, AuNPs with an average of one ssDNA per particle was chosen as the optimum aptamer modified AuNP reagent. Some of the AuNPs might contain no ssDNA; however, this would not affect the assay because those AuNPs without ssDNA could be washed out by passing the filter membrane before introducing to the target molecules. The results in Figure 14 support that these AuNPs with TOEG6 had little attraction with the GO.

Table 7. Effect of TOEG6 concentration on aptamer binding to AuNPs.

AuNPs (nM)	ssDNA (μM)	TOEG6 (μM)	No. of ssDNA/NP
0.5	0.25	3	10
0.5	0.25	5	9
0.5	0.25	7	8
0.5	0.25	10	5
0.5	0.25	15	1

To guarantee that the reaction of thrombin with aptamer reached equilibrium before spICP-MS analysis, the incubation time of thrombin and GO/AuNPs composites was investigated. As shown in Figure 17B, the number of detected NPs increased quickly with incubation time during the first 30 min but reached a plateau at 60 min. There was no further change even when the incubation time was extended to 2 h. As a result, the incubation time of 60 min was determined as the optimal reaction time for the assay method.

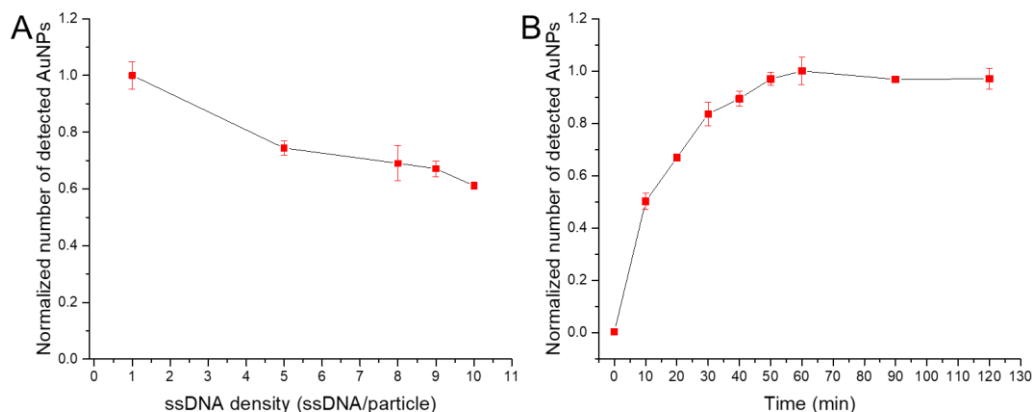


Figure 17. The optimizations of aptamer density on AuNPs (A), and incubation time (B). Thrombin concentration: 10 pM. GO/AuNPs composites concentration: 1 $\mu\text{g}/\text{mL}$ (GO mass based) Incubation in PBS buffer (10 mM with 0.5 mM MgCl_2 , pH 7.4).

3.5. The Sensitivity of Thrombin Detection.

The assay was applied to thrombin detection using the spICP-MS under the optimized conditions. As shown in Figure 18, the number of detected AuNPs systematically increased within the 30 s collection time as the thrombin concentration increased from 1.0 fM to 10.0 nM. There were also a few detected AuNPs without adding thrombin in the blank (Figure 18A). The concentration of residual AuNPs in the blank was as high as $(40 \pm 6) \times 10^3$ particle/mL after washing steps. Moreover, there was no difference between the blank and the sample with 0.1 fM of the thrombin, which established a concentration below the detection limit of the method (Figure 18B). With the 1.0 fM of thrombin sample, there was a noticeable increase in detected AuNPs compared with blank, although the distinction was only slight (Figure 18C). When the concentration of thrombin was higher than 10.0 fM, the number of detected AuNPs increased dramatically (Figure 18B-J).

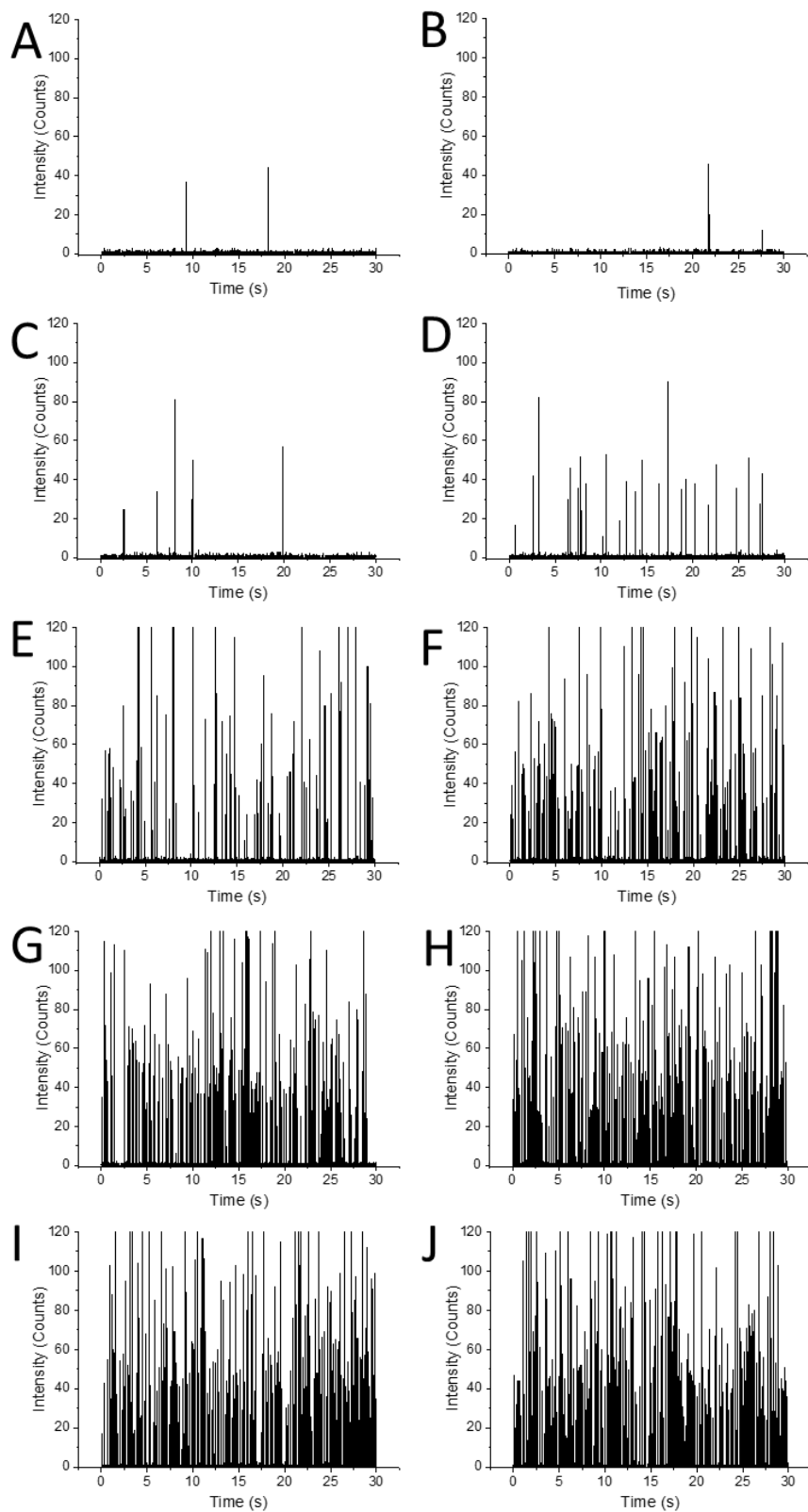


Figure 18. spICP-MS spectra of AuNPs in the presence of different concentrations of Thrombin (A to J: 0, 10^{-4} , 10^{-3} , 10^{-2} , 10^{-1} , 1, 10, 10^2 , 10^3 , 10^4 pM). GO/AuNPs composites concentration: 1 $\mu\text{g}/\text{mL}$ (GO mass based). Incubation at 37 $^{\circ}\text{C}$ for 60 min in PBS buffer (10 mM, 0.5 mM MgCl_2 , pH 7.4). 200 folds dilution before injecting into spICP-MS (^{197}Au , dwell time: 5 ms).

The quantitative relationship between the concentration of thrombin and the concentration of desorbed AuNPs is demonstrated in Figure 19. Here, N_0 is the number of detected AuNPs in the blank as control and N is the number of detected AuNPs at different thrombin concentrations. This assay showed a broad dynamic range from 1.0 fM to 10.0 nM. It also showed a logarithmic relationship with the thrombin concentration from 10.0 fM to 100.0 pM (Figure 19 inset) with a correlation coefficient (R^2) of 0.9997. The limit of detection was estimated to be 4.5 fM by the 3σ rule, which was around 5 orders of magnitude lower than the similar graphene based platform.^{41, 45}

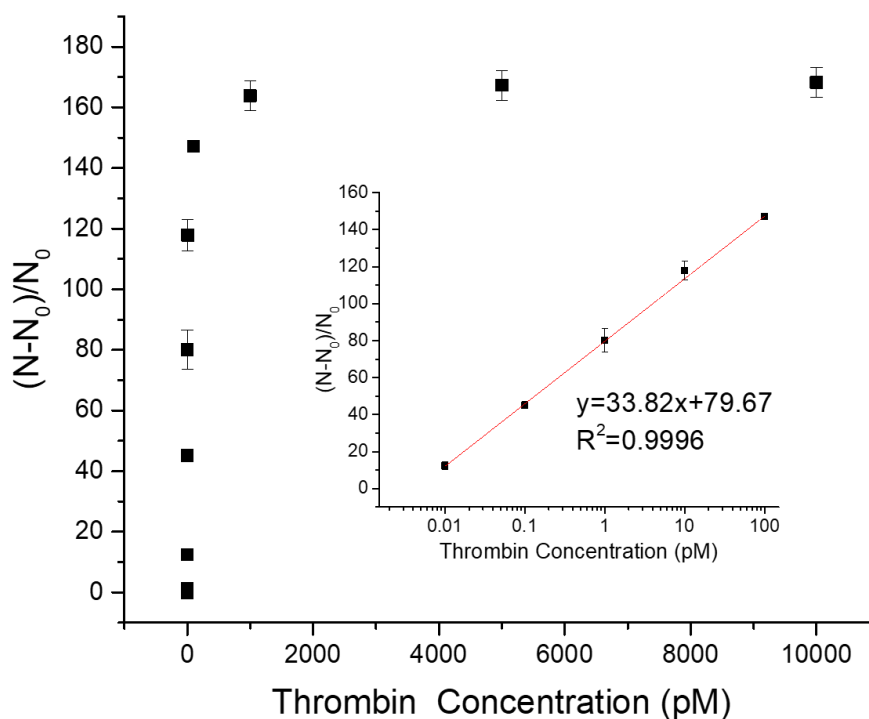


Figure 19. Relationship between the changes of number of detected AuNPs and thrombin in concentration from 10^{-4} to 10^4 pM. Acquisition period: 180 s. Inset: Calibration curve of the changes of number of detected AuNPs and thrombin concentration from 10^{-2} to 10^2 pM.

3.6. Selectivity.

The specificity of the developed sensor was evaluated by testing other protein components in a serum sample. As shown in Figure 20, the desorbed AuNPs detected

by reacting with BSA, IgG, and FBS respectively at a concentration of 1.0 μM (~ 0.1 g protein/L for FBS) were less than 10% of that caused by thrombin at a concentration of 10.0 pM. This result strongly demonstrated that the method could be used for both selective and sensitive detection of the target biomolecules. Moreover, the fact that the sample of thrombin in FBS showed the same signal level compared to the pure thrombin showed that the method was not significantly influenced by interferes and indicated its great potential for applications with complex sample interferes.

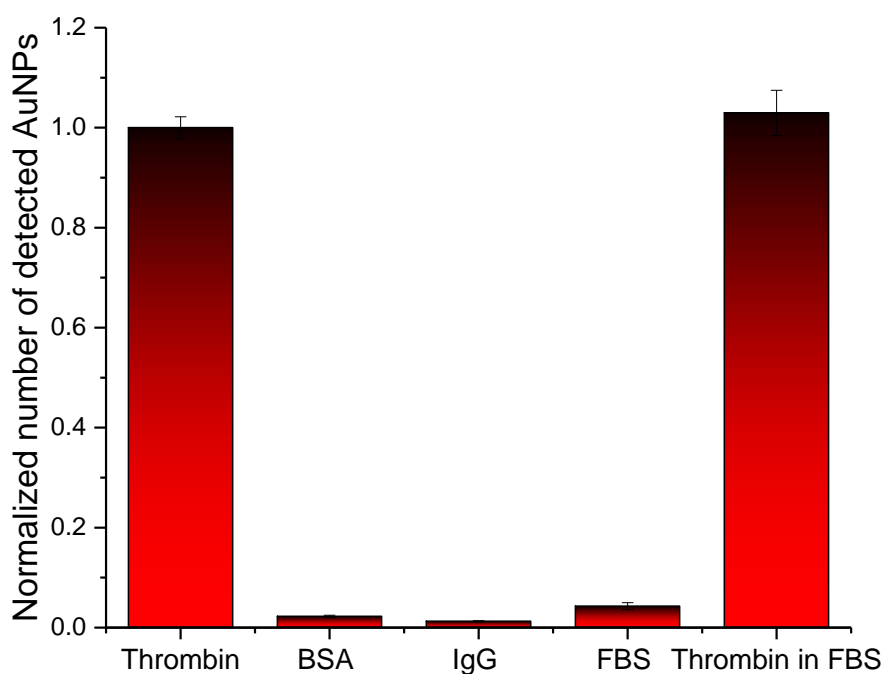


Figure 20. Selectivity of the platform for thrombin detection by spICP-MS. Thrombin concentration: 10.0 pM; BSA and IgG concentrations: 1.0 μM ; FBS concentration: ~ 0.1 g protein/L. GO/AuNPs composites concentration: 1 $\mu\text{g}/\text{mL}$ (GO mass based). Incubation at 37 $^{\circ}\text{C}$ for 60 min in PBS buffer (10 mM, 0.5 mM MgCl_2 , pH 7.4).

4. Conclusions

In conclusion, a GO/AuNPs platform for ultrasensitive detection of target biomolecules using spICP-MS technology was developed. In this case, thrombin was used as a model target molecule and could be detected at as low concentration as 4.5

fM. Compare with similar fluorescence-based platforms this detection limit was lower by five orders of magnitude, making this method comparable to other ultrasensitive detection methods for thrombin.⁶³⁻⁶⁴ It is also noteworthy that this detection limit could be further reduced by removing the free AuNPs in the GO/AuNPs composites or coupling an amplification strategy. Because of the excellent specificity of the aptamer,⁵⁸ this platform also showed high selectivity. Moreover, the type nanoparticles used as a metal isotope signal source for spICP-MS could be varied, making it possible for simultaneous multi-target detection. Finally, the method's minimal interference from the matrix makes it suitable for applications in clinical diagnostics.

CHAPTER III

DETECTION OF ESCHERICHIA COLI IN DRINKING WATER USING dsDNA-TEMPLATED COPPER NANOPARTICLES WITH HYBRIDIZATION CHAIN REACTION

1. Introduction

Escherichia coli (*E. coli*) is one of the most common pathogens that cause different kinds of diseases.⁶⁵⁻⁶⁷ The *E. coli* in drinking water, coming from domestic wastewater discharge or other sources such as livestock manure, poses a threat to human health, especially to children.⁶⁶ Therefore, the development of sensitive, fast and accurate methods for detection of *E. coli* is very important in the food industry, environmental monitoring, and clinical diagnostics. Traditional methods for detecting *E. coli* are based on microbiological culture procedures.⁶⁸⁻⁶⁹ These detection methods are sensitive and specific, but they are time-consuming (48-72 h), labor-intensive and requires highly skilled staff and expensive facilities. Therefore, several ultrasensitive detection methods, such as enzyme-linked immunosorbent assay,⁷⁰⁻⁷¹ polymerase chain reaction (PCR)⁷² and novel biosensors, including impedimetry,⁷³⁻⁷⁴ surface plasmon resonance (SPR),^{67, 75} colorimetry,⁶⁶ micro-cantilever⁷⁶ and fluorescence,⁶⁹ have been developed for quick detections.

Fluorescent methods have been widely applied in biosensors for detection of various targets, such as ions, small molecules, proteins and cells for more than two decades.⁷⁷⁻⁸⁰ The optical features of the fluorophores play the most critical function in determining the sensitivity and application fields of the biosensor. Other than traditional organic dyes, several novel fluorescent nanomaterials, such as NPs,⁷⁹ metal quantum dots (QDs)⁸¹⁻⁸² and graphene QDs,⁸³⁻⁸⁴ have been widely researched and applied. dsDNA templated CuNPs, as a new class of fluorescent nanomaterial, showed great potential as fluorescent probes for biochemical applications due to their merits of

ultrafine size, low toxicity, good biocompatibility, and outstanding photophysical properties.⁸⁵⁻⁸⁶ So far, dsDNA templated CuNPs have been applied for small molecule sensing,⁸⁷ DNA assay,^{86, 88} and protein detection.⁸⁹ More importantly, the synthesis of CuNPs can be accomplished by reducing Cu²⁺ ions with ascorbate on the dsDNA scaffold within 5-10 minutes under mild conditions. This suggests a great potential to reduce analysis time.⁹⁰⁻⁹¹

Commonly, the dsDNA sequence used as CuNPs template is monomeric and short. One dsDNA provided just one site for one CuNP. So, high concentration of dsDNA is required to reach the detectable fluorescence intensity.^{85, 87} Fortunately, the development of amplification techniques for DNA have made the detection of low concentrations of DNA possible.⁵⁰ PCR is the most popular technology for amplifying and detecting low-abundance nucleic acids, but the thermal process required in the method limits its application in biosensors.⁹²⁻⁹³ To overcome this drawback, isothermal amplification methods which can rapidly and efficiently accumulate nucleic acid sequences at constant temperature have been developed since the 1990s,⁵⁰ such as strand displacement amplification (SDA),⁹⁴⁻⁹⁵ rolling circle amplification (RCA),^{86, 96} and ligase chain reaction.⁹⁷ The limit is that an enzyme is still needed during the amplification, which requires relatively strict conditions to maintain high activity. The HCR technique has attracted increasing interest for DNA amplification compared to the isothermal amplification methods mentioned because it is an enzyme-free amplification method.⁹⁸ Furthermore, different from other methods that duplicate the DNA, the HCR technique grows the original oligonucleotides into long nicked dsDNA polymers under mild conditions. Accordingly, the HCR technique has been widely used with various types of biosensors for sensitively detecting ions, DNA, proteins and cells.^{89, 99-102}

In this work, a novel sandwich structure biosensor for *E. coli* detection was

developed using antibody and aptamer as ligands, and fluorescence of CuNPs as signal. The design combined the advantages of dsDNA templated CuNPs and the high efficiency of the HCR amplification technique. Anti *E. coli* antibody modified magnetic beads (MBs) were used to capture the target bacteria, then the primer ssDNA sequence was introduced based on a sandwich structure between *E. coli* aptamer and *E. coli*. The obtained primer initiated the HCR in the presence of HCR probes to form a long length of dsDNA. Ultimately, the CuNPs were produced using the dsDNA as templates, emitting the bright fluorescence with an *E. coli* concentration-dependent manner.

2. Experimental Section

2.1. Materials.

Copper sulfate pentahydrate, sodium ascorbate, sodium chloride, 3-(N-Morpholino) propanesulfonic acid (MOPS), ethylenediaminetetraacetic acid (EDTA), hemin, 2-amino-2-(hydroxymethyl)-1,3-propanediol (Tris-base), phosphate buffered saline (PBS), and bovine serum albumin (BSA) were purchased from Sigma Aldrich Inc. Lysogeny broth (LB) medium and streptavidin coated MBs were purchased from Thermo Fisher Scientific Inc. Anti-*E. coli* antibody (Biotin labeled) was purchased from Abcam. *E. coli* O157: H7 strain (ATCC 43888), *Staphylococcus aureus* (*S. aureus*) strain (ATCC 13301) were obtained from the American Tissue Culture Collection (ATCC). *Acinetobacter baumannii* (*A. baumannii*), *Klebsiella pneumoniae* (*K. pneumoniae*), and *Pseudomonas aeruginosa* (*P. aeruginosa*) PAO1 were provided by Dr. Min Wu's lab. The deionized (DI) water (18.2 MΩ•cm) was produced from a Millipore water purification system. All oligonucleotides were synthesized by IDT Inc. The sequences of DNA used were as follows:

HP1: 5'-TCAACATCAGTCTGATAAGCTACCTCCTAGCTTATCAGACTGAT-3'

HP2: 5'-TAGCTTATCAGACTGATGTTGAATCAGTCTGATAAGCTAGGAGG-3'

Primer: 5'-TAGCTTATCAGACTGATGTTGA-3'

Aptamer-primer (APP): 5'-ATCAAATGTGCAGATATCAAGACGATTTGTACAA
GATTTTTTAGCTTATCAGACTGATGTTGA-3'

2.2. Instruments.

Fluorescence intensities were measured using a RF-6000 spectrophotometer (Shimadzu, Japan). Zeta potential of formed CuNPs were measured by a Zetasizer Nano (Malvern Panalytical, UK). A Hitachi SU8010 field emission scanning electron microscope (Hitachi, Japan) was used to take the SEM images of the bacteria and MBs.

2.3. Preparation of Antibody Conjugated Magnetic Beads (MBs).

The antibody modified MBs were prepared according to a previously reported method with a slight modification.¹⁰³ A suspension of 10 μ L of commercial streptavidin-modified MBs was transferred into a 1.5 mL tube. The MBs were washed twice with 200 μ L of PBS buffer solution and then re-suspended in 100 μ L of PBS containing 20 μ g/mL of biotin modified anti-*E. coli* antibody. Incubating at 37 °C under continuous stirring for 30 min, the antibody was captured onto the beads surface based on streptavidin-biotin affinity interaction. After washing twice with 200 μ L of PBS buffer, the antibody-modified MBs were re-suspended in PBS buffer containing 0.1% bovine serum albumin (BSA) and incubated for 2 h at 4 °C to block residual sites on magnetic beads.⁶⁶ In the washing step, the magnet holding block was used for the separation to remove the supernatant.

2.4. Bacteria Culture.

A monoclonal colony of *E. coli* O157: H7 was selected from a previously inoculated Luria–Bertani (LB) Broth agar plate and grown in LB broth overnight at 37 °C with shaking. The bacterial cells were collected by centrifugation and were re-dispersed in a

PBS buffer with an optical density of 1.0 at 600 nm (OD_{600}) as the stock mother solution. The centrifugation step was repeated three times. Then, the mother solution was serially diluted to the desired concentrations for further use.

2.5. Bacteria Capture Using Antibody Conjugated MBs.

First, the *E. coli* stock solution was diluted to the following concentrations 10^1 , 10^2 , 10^3 , 10^4 , 10^5 , 10^6 and 10^7 CFU/mL using PBS buffer. Then the prepared antibody modified MBs (10^6 /mL) were added to each of the bacterial solutions and incubated for 20 min at 37 °C with regular shaking. Then the bacterial cells bound on the MBs were enriched and washed three times with PBS buffer. The bacteria-beads complexes were re-suspended in 100 μ L of PBS buffer for further measurement.

2.6. Fluorescence Detection Using dsDNA Templated CuNPs.

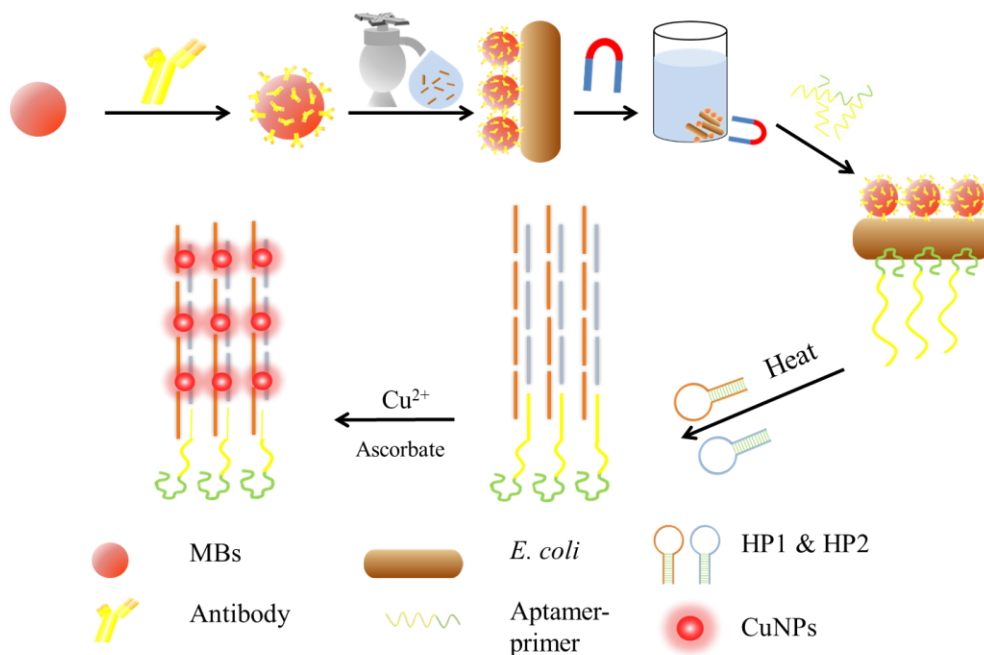
A 10 μ L aliquot of 100 nM anti-*E. coli*. aptamer-primer in PBS buffer was added into the bacteria-beads complex solution and was incubated for 1 h at 37 °C. After washing three times with PBS and once with MOPS buffer, the composites were heated to 95 °C for 5 min. The supernatant was collected after centrifuging at 8,000 rpm for 5 min when the solution was cooled down to room temperature. A 50 μ L aliquot of each HP1 and HP2 (500 nM) were separately added and incubated for 1 h to process the HCR reaction. Subsequently, 200 μ M Cu^{2+} and 4 mM sodium ascorbate in MOPS buffer were added and allowed to react for 10 min at room temperature. The fluorescence emission was determined using a fluorescence spectrophotometer at a wavelength of 615 nm under a 350 nm excitation.

Samples of prefiltered drinking water were inoculated with *E. coli* cells in concentrations ranging from 10.0 to 1.0×10^7 CFU/mL. A 100 μ L aliquot of each sample was analyzed following the method described above for standard bacterial solutions. The pure prefiltered drinking water was used as a negative control.

3. Results and Discussion

3.1. Design of the Biosensor Platform for Bacterial Detection.

In this study, we have developed a biosensor platform for sensitive and selective detection of bacteria using HCR amplification and dsDNA-templated CuNPs. As shown in Scheme 3A, anti-*E. coli* antibody was first immobilized on the surface of MBs by the interaction between biotin and streptavidin. Followed by incubating with the *E. coli* in water, the bacteria were captured by the antibodies on the surface of MBs (Scheme 3B). After enrichment of the MBs by a magnet (Scheme 3C), a ssDNA (APP) with the specific sequence was introduced and reacted with the captured bacteria (Scheme 3D). The APP was designed for two functions. At the one end of the APP an aptamer to *E. coli* was linked so that they were able to capture the bacteria by incubating the APP with *E. coli*. The other end of APP was the primer to initiate the HCR. The obtained APP was melting eluted by high temperature and was then incubated with the HCR probes (HP1 and HP2) to form a long dsDNA chain, which was used as the template for the formation of the CuNPs. The fluorescent CuNPs were finally produced after adding the Cu^{2+} and ascorbate to the system. The fluorescence intensity of the CuNPs was proportional to the concentration of the captured *E. coli*.



Scheme 3. Scheme for the detection of *E. coli* using dsDNA-templated CuNPs amplified by the HCR

3.2. Antibody Modified MBs for Specifically Capturing *E. coli*.

To effectively capture the bacteria, the immobilization of antibodies on the MBs was critical. The MBs used was streptavidin modified so the biotin labeled antibody could easily link to the MBs surface. Due to the specificity of the antibody-antigen interaction, only the target *E. coli* bacteria would be captured in the solution. Capture of bacteria using the antibody modified MBs was demonstrated through SEM images. As shown in Figure 21A, the captured *E. coli* was attached to the MBs after washing. Because the size of MBs was very close to the length of *E. coli*, normally, only one or two MBs were bound to one bacterial cell. As a control, *S. aureus* bacteria were used for the same experiment. As shown in Figure 21B, there were no *S. aureus* bacteria captured around the MBs, demonstrating a good selectivity that the anti-*E. coli* antibody modified MBs could capture *E. coli* bacteria only.

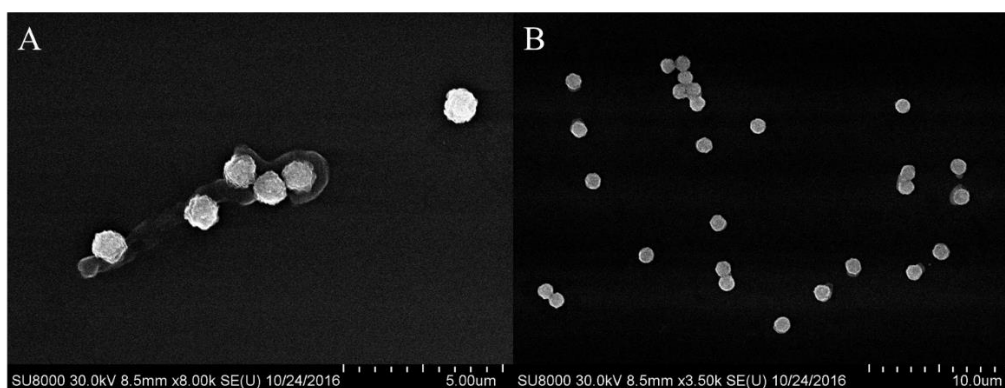


Figure 21. SEM images of MBs (1 μ M) incubated with *E. coli* (A) and *S. aureus* (B). Incubate at 37 $^{\circ}$ C for 20 min; Bacteria concentration: 10^6 CFU/mL.

3.3. Formation of Fluorescent CuNPs through dsDNA Templating.

The signal readout of the biosensor was based on fluorescent CuNPs that were templated by the dsDNA of HP1 and Primer. The formation of the CuNPs was confirmed in Figure 22. The hydrodynamic diameter of the CuNPs was 10.97 ± 2.30 nm (Figure 22A), which was close to the reported dsDNA templated CuNPs sizes. The optical property of formed CuNPs was investigated by fluorescence measurements. As shown in Figure 22B, the excitation peak and emission peak were 350 nm and 615 nm, respectively. Both peaks were red-shifted compared to the reported dsDNA templated CuNPs, which were 340 nm and 596 nm, respectively.^{85, 104}

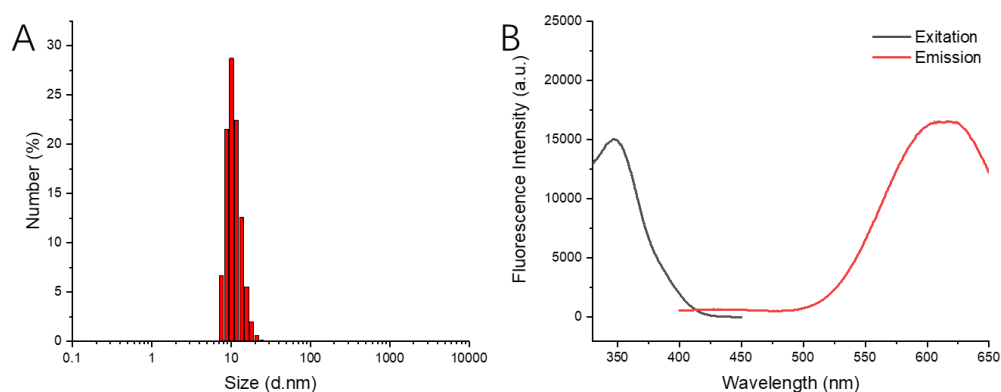


Figure 22. The size distribution of CuNPs (A), and the fluorescence spectrum of CuNPs(B).

3.4. Amplification by the Hybridization Chain Reaction (HCR)

To achieve the ultrasensitive detection of the bacteria, the HCR amplification strategy was applied after the capture of the bacteria. In principle, the fluorescence intensity of CuNPs depended on the amount of CuNPs formed, which was related to the number of dsDNA template units. Therefore, the increase of dsDNA number was critical. After HCR amplification, the length of dsDNA was much longer than the one prior to HCR, providing more dsDNA templates for the formation of CuNPs. As shown in Figure 23A, there was no fluorescence measured in the absence of DNA due to the lack of template (curve a). In the presence of the single HP1 or HP2 probes, a slight fluorescence peak at 615 nm was measured because of the short double stranded stem structure in the original hairpin structure were formed (curve b and c). The fluorescence intensity was as weak as the single probe templated CuNPs after mixing two hairpin probes together, demonstrating that there was no spontaneous reaction without primer sequence as the initiator (curve e). In the presence of primer and HP1 probes, the fluorescence intensity was slightly stronger than the groups with only hairpin probes (curve d). The short length dsDNA formed based on the complementary sequences between the primer and part of HP1. Compared with the group d, adding HP2 together with HP1 and primer made the HCR amplification processed, forming the long length of dsDNA, not merely the short one. The fluorescence intensity was significantly increased (curve f). The results demonstrated that the use of HCR amplification was necessary and efficient. The strong fluorescence presented in orange color could also be observed under the UV lamp excitation as shown in Figure 23B (f).

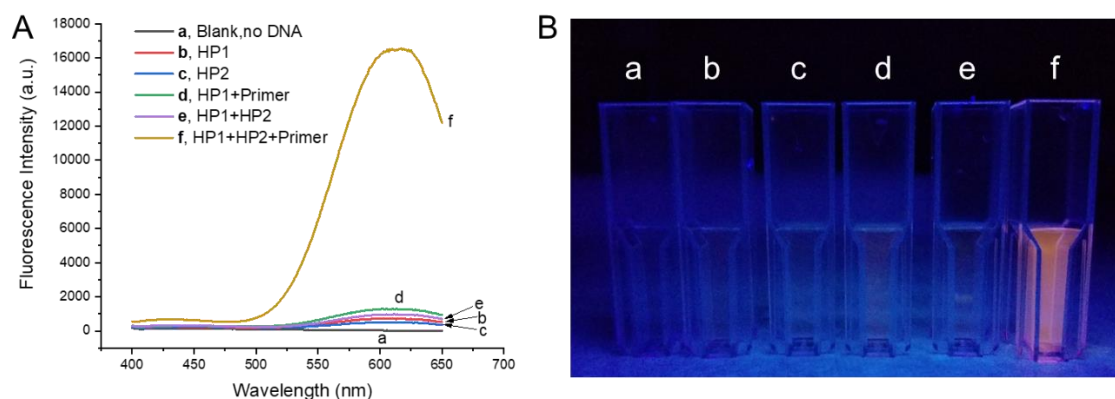


Figure 23. A, Fluorescence spectra of the CuNPs formed using different templates: a, no DNA; b, 1 μ M HP1 only; c, 1 μ M HP2 only; d, 1 μ M HP2 and 50 nM Primer; e, 500 nM HP1 and 500 nM HP2; f, 500 nM HP1, 500 nM HP2 and 50 nM Primer. HCR reaction time was 1 h. The concentration of Cu^{2+} and sodium ascorbate were 200 μ M and 4 mM, respectively. CuNPs formation time was 10 min. The excitation wavelength was 350 nm. B, Photograph of the fluorescent CuNPs formed using different templates under an UV excitation.

3.5. Optimizations.

To maximize the performance of the biosensor, several experimental conditions were optimized. As discussed previously, two major factors should affect the sensitivity of the biosensor. The first factor was the target bacteria capture efficiency by antibody modified MBs. The second factor was the formation of dsDNA templated CuNPs. The ratio of antibody modified MBs to bacteria should affect the bacteria capture efficiency. In general, as the constant amount of bacteria existed, the more MBs used, the more bacteria captured. Therefore, we fixed the number of bacteria at the level of 10^5 CFU/mL, then changed the amount of MBs from 1.0 to 1.0×10^8 . The uncaptured bacteria quantified by the plate colony counting after incubating with MBs. As shown in Figure 24A, the uncaptured bacteria amount reached a constant number, closed to 0, when the amount of MBs of 10^6 was used. Almost all bacterial cells were captured under this MBs concentration, the extra amount of MBs (10^7 and 10^8) made no further contribution. Considering the bacterial concentration in real samples is much lower than the number we chose here, the 10^6 of MBs was sufficient and thus was applied in the

subsequent experiments.

The optimal incubation time of MBs with bacteria was then studied. As shown in Figure 24B, the reaction between MBs and bacteria was fast due to the strong affinity between the antibody and antigen. The number of uncaptured bacteria was dramatically decreased after 20 min of reaction and reached a plateau. In the premise of time saving, 20 min was chosen as the optimal incubation time.

The fluorescence signal from CuNPs used as signal readout was not stable as expected during the CuNPs formation process. To obtain a reliable signal the reaction time of Cu^{2+} with sodium ascorbate to form the CuNPs was investigated. As shown in Figure 24C, the fluorescence dramatically increased in seconds after the reduction reaction between Cu^{2+} and sodium ascorbate started. The fluorescence intensity reached a peak and started to drop at around 100 s after the reaction. The fluorescence eventually dropped down to a constant level after 400 s. The reason for this phenomenon was unclear and needed further study. At this stage, a reaction time of 10 min in the constant range was selected for subsequent experiments.

The formation of long lengths of dsDNA through the HCR required sufficient reaction time. To guarantee the reaction was complete, the incubation time of the HCR was studied. As shown in Figure 24D, the fluorescence intensity increased with the increasing of reaction time for the HCR. The fluorescence signal reached a plateau and remained constant after 50 min. Therefore, the incubation time of 60 min was chosen as the optimal condition.

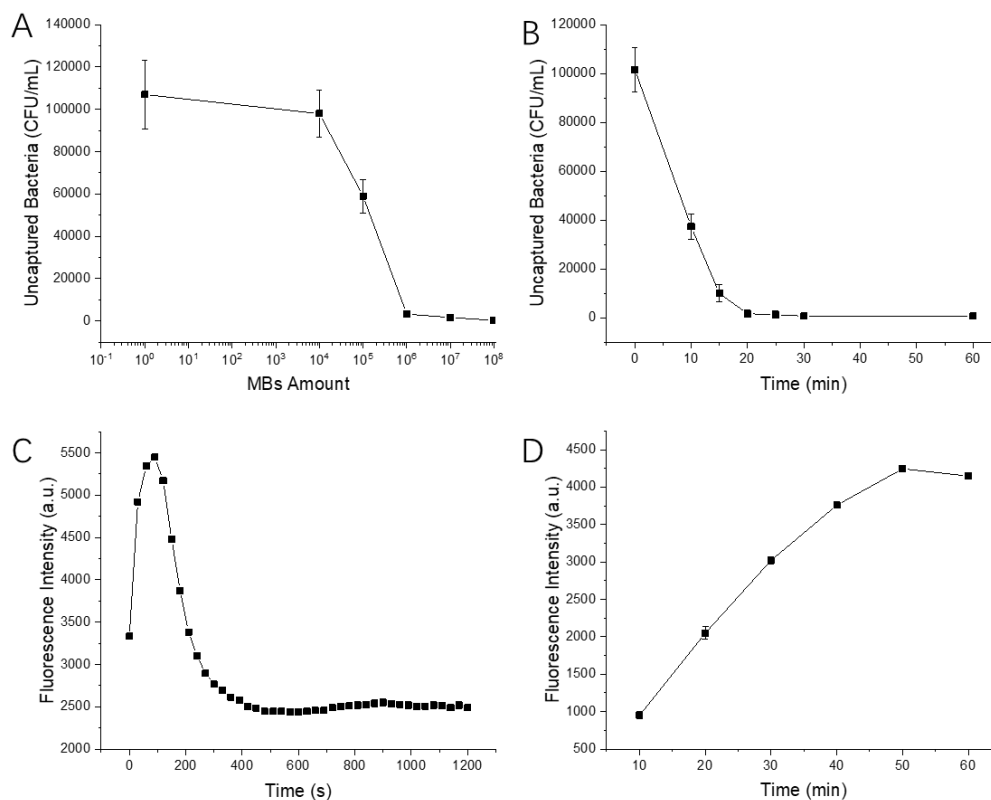


Figure 24. The effect of different experimental conditions on the detection of *E. coli*. (A) Impact of the amount of antibody modified MBs on the capture efficiency of *E. coli*. (B) Impact of incubation time between MBs and bacteria on the capture efficiency of *E. coli*. (C) Time dependence of the fluorescence intensity after adding Cu²⁺ (200 μ M) and sodium ascorbate (4 mM), 500 nM of HP1 and 500 nM of primer probes for formation of CuNPs, λ_{em} = 615 nm, λ_{ex} = 350 nm. (D) Impact of incubation time of HCR amplification on the fluorescence of CuNPs with 50 nM of primer, 500 nM of HP1 and 500 nM of HP2.

3.6. Application of the Biosensing System for the Detection of *E. coli* in Water.

Under the optimal conditions, the biosensor was applied to detect different concentrations of *E. coli* O157: H7 in water. As shown in Figure 25A, the fluorescence of CuNPs increased with the augment of target bacteria from 5×10^3 to 10^8 CFU/mL. The fluorescence intensity from 10^3 CFU/mL bacteria (yellow curve) was undistinguishable with the blank (red curve). The relationship between the fluorescence change and the concentration of bacteria was quantified in Figure 25B. Here, $(F-F_0)/F_0$ was defined as the signal change, where F_0 was the fluorescence intensity of dsDNA templated CuNPs without *E. coli* O157: H7 in the sample solution; F was the

fluorescence intensity of dsDNA templated CuNPs with different concentration of *E. coli* O157: H7 in the sample. A dynamic range of 5×10^3 to 10^8 CFU/mL concentration was found with a linear range between 5×10^3 to 10^5 CFU/mL. We estimated the detection limit for *E. coli* O157: H7 detection was 5.2×10^3 CFU/mL. The result was close to or lower than several reported biosensor for the detection of *E. coli* O157: H7.¹⁰⁵⁻¹⁰⁶

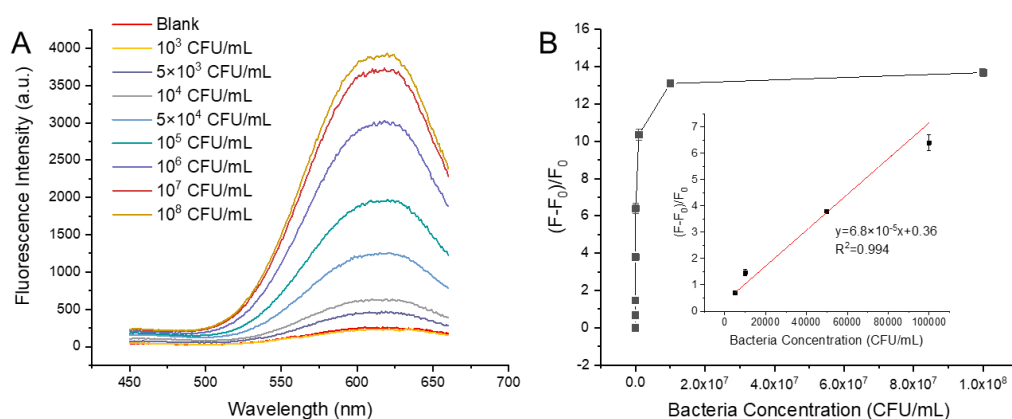


Figure 25. (A) Fluorescence of dsDNA templated CuNPs to different concentrations of *E. coli* O157: H7. (0 , 10^3 , 5×10^3 , 10^4 , 5×10^4 , 10^5 , 10^6 , 10^7 , and 10^8 CFU/mL). (B) Relationship of bacteria concentration (0 , 5×10^3 , 10^4 , 5×10^4 , 10^5 , 10^6 , 10^7 , and 10^8 CFU/mL) and fluorescence intensity of CuNPs. Inset: Linear range from 5×10^3 to 10^5 CFU/mL. Ex: 350 nm; Em: 615 nm.

3.7. Selectivity of the Biosensor.

Due to the deployment of bi-ligands with high specificity, excellent selectivity for the biosensor was expected. Some common pathogenic bacteria strains, including *A. baumannii*, *K. pneumoniae*, *S. aureus*, and *P. aeruginosa*, were applied as competitors. As shown in Figure 26, the value of $(F-F_0)/F_0$ of *E. coli* was significantly larger than that of other groups at the same concentration of 10^5 CFU/mL. Furthermore, the signal of all other groups was almost close to 0. The results demonstrated that this biosensor has a great specificity to *E. coli*.

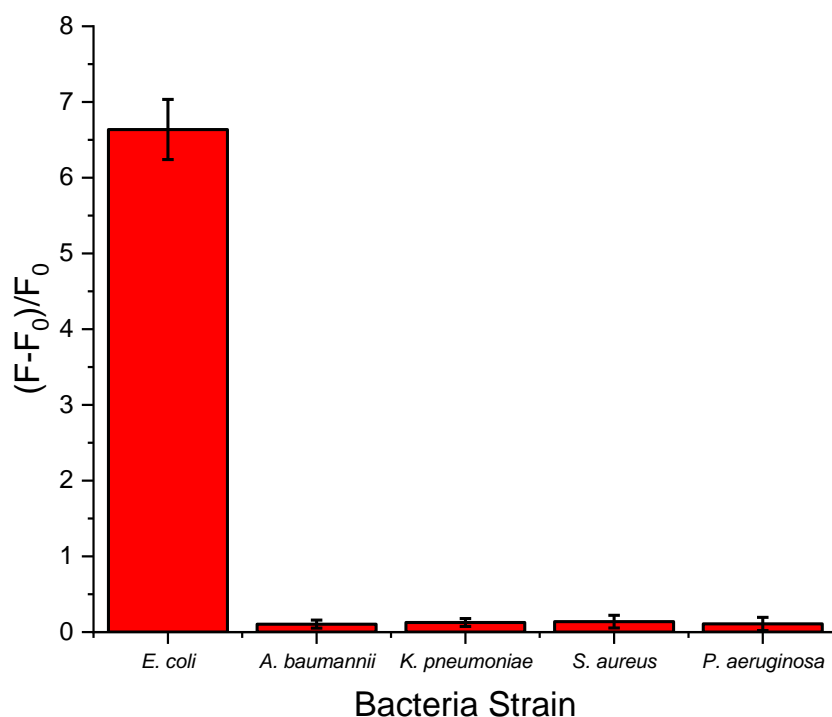


Figure 26. Fluorescence of dsDNA templated CuNPs to target *E. coli* various other bacteria strains (*A. baumannii*, *K. pneumoniae*, *S. aureus*, and *P. aeruginosa*) at a concentration of 10^5 CFU/mL. Ex: 350 nm; Em: 615 nm.

4. Conclusions

In conclusion, the sensitive and selective biosensor for the detection of *E. coli* bacteria using dsDNA templated fluorescent CuNPs as signal combined with HCR amplification was developed. By means of the enrichment of MBs and signal amplification strategy, the ultralow detection limit of 5.2×10^3 CFU/mL was achieved. Furthermore, the excellent selectivity was achieved by using a two ligands-based sandwich structure. Only the target bacteria bound to both ligands could eventually lead to the fluorescence change. The method was applied to the water samples spiked with *E. coli*. The result demonstrated the potential of the biosensing system for monitoring bacteria in real samples.

CHAPTER IV

BIOCOMPATIBLE G-QUADRUPLEX/HEMIN FOR ENHANCING ANTIBACTERIAL ACTIVITY OF H₂O₂

1. Introduction

Pathogenic bacteria are a major threat to human health worldwide.¹⁰⁷⁻¹⁰⁸ To prevent bacterial infections, a number of antibacterial substances have been developed and are widely used in our daily life.¹⁰⁹ A variety of antiseptics, such as antibiotics,¹¹⁰ metal ions,¹⁰⁸ quaternary ammonium compounds,¹¹¹ and polymers,¹¹² have been tested and applied to prevent or treat bacterial infections through diverse antibacterial mechanisms. However, continued use of many antibacterial agents may decrease their effectiveness over time due to the emergency of drug-resistant bacterial strains¹¹⁰⁻¹¹⁴. Therefore, the development of new and powerful antibacterial agents is in critical need. In the past decade, the emerging field of nanoscience and nanotechnology has produced a number of novel nanomaterials that showed excellent antibacterial activity, such as silver nanoparticles,^{108, 115} carbon nanotubes,¹¹⁶⁻¹¹⁷ graphene and graphene-based nanomaterials.¹¹⁷⁻¹¹⁹ In addition to the development of new antibacterial agents, improving the efficiency of existing antiseptics is also an attractive strategy due to low side-effects, which would be an important consideration for new antimicrobial development.

One of the traditional disinfectant agents that is widely used is hydrogen peroxide (H₂O₂) solution, as its applications can range from wound treatment and sterilization to high-level disinfection for healthcare settings, etc.¹²⁰ Meanwhile, as a low cost surface disinfectant, H₂O₂ can also be used to sterilize semicritical and noncritical equipment due to its broad-spectrum bactericidal, virucidal, sporicidal, and fungicidal properties, excellent stability, and environmentally friendly characteristics. Usually, to achieve a desired disinfection efficiency, a high concentration of H₂O₂ is

needed. For example, in a regular wound treatment, 0.5 to 3%, ca. 166 mM to 1 M H_2O_2 ¹²⁰⁻¹²¹ is needed to achieve the desired effectiveness, while in pharmaceutical and health care environments up to 35% of H_2O_2 is needed.¹²² However, such a high concentration of H_2O_2 is harmful to human health. Thus, great caution is required during these application processes. Additionally, in the case of wound treatment, high concentration of H_2O_2 could delay wound healing. Thus, a challenge for traditional antibacterial agent H_2O_2 remains, that is, how to keep its antibacterial efficiency with minimal amount of H_2O_2 .

Recent research found that the antibacterial capacity of the hydroxyl radical ($\cdot\text{OH}$) is much stronger than that of H_2O_2 .¹²³ This finding provides a viable approach of using low concentration of H_2O_2 to enhance antibacterial effects if H_2O_2 could be converted to $\cdot\text{OH}$. In fact, two common approaches have been reported to convert H_2O_2 to $\cdot\text{OH}$. One is the indirect formation of $\cdot\text{OH}$ from H_2O_2 via the iron-driven Fenton's reagent, a ferrous ion that catalyzes the decomposition of H_2O_2 to form $\cdot\text{OH}$.¹²⁴ This method has been widely used for wastewater treatment and hazardous chemical destruction.¹²⁵⁻¹²⁶ The other method of converting H_2O_2 to $\cdot\text{OH}$ is use of a peroxidase, such as catalase,¹²⁷ horseradish peroxidase,¹²⁸ and cytochrome c peroxidase.¹²⁹ Recently, nanomaterials with peroxidase-mimic property also played an important role for converting H_2O_2 to $\cdot\text{OH}$, which can significantly enhance the antibacterial property of H_2O_2 .¹³⁰⁻¹³² Sun and co-workers have demonstrated that graphene quantum dots (GQDs) with peroxidase-like property displayed a strong enhancement of antibacterial activity of H_2O_2 against both Gram-negative (*Escherichia coli*) and Gram-positive (*Staphylococcus aureus*) bacteria.¹³⁰ Gao and co-workers have reported that ferromagnetic nanoparticles with peroxidase-like activity can enhance antibacterial activity in the presence of H_2O_2 at the concentration of 1%.¹³² However, the iron ions

and those nanomaterials are potentially toxic to healthy cells.¹³²⁻¹³⁴ Moreover, the synthetic procedures are complex and difficult to scale up.

To overcome these challenges, we proposed to use DNAzymes to convert H_2O_2 to $\cdot\text{OH}$.¹³⁵⁻¹³⁷ DNAzymes with peroxidase-like activity were first reported in the late 1990s.¹³⁸⁻¹³⁹ Essentially, as a class of DNAzymes, G-quadruplex/hemin (G/H) complexes are hemin molecules bonded with their guanine-rich single strand DNA (ssDNA) aptamers, forming a quadruplex structure with the hydrogen bond between guanine bases.¹³⁹⁻¹⁴¹ This artificial system would increase the catalytic activity of hemin.¹³⁹ Up to recently, the G/H complex with peroxidase-like activity was mainly applied in bioanalytical chemistry for biosensing.¹⁴²⁻¹⁴⁸ In addition, the G/H complex was also applied *in vitro*.¹⁴⁹⁻¹⁵⁰ Zhang and co-workers used nanogel as a carrier to deliver the G/H complex into cells for selective oxidation.¹⁴⁹ However, the applications of the G/H complex for converting H_2O_2 to $\cdot\text{OH}$, as well as for antibacterial researches have not been reported.

Our design combined the advantages of oligonucleotides, such as thermal stability, hydrolysis resistance, ease of synthesis and modification, potential for scale production,¹⁵¹ and excellent peroxidase-mimic property. An antibacterial system based on a low concentration of H_2O_2 and the G/H complex as the additive was designed. The results showed that the addition of the G/H complex could effectively enhance the antibacterial activity against representatives of both Gram-positive and Gram-negative bacteria and dramatically inhibit their growth. The developed complex was successfully applied to the *in vivo* wound disinfection model without apparent side effects.

2. Experimental Section

2.1. Materials.

Hydrogen peroxide ($\geq 30.0\%$), terephthalic acid (TA), 2,2'-azinobis (3-ethylbenzthiazoline-6-sulfonate) (ABTS), potassium chloride (ACS reagent, $\geq 99.0\%$), dimethyl sulfoxide (DMSO), ethylenediaminetetraacetic acid (EDTA), hemin, 2-amino-2-(hydroxymethyl)-1,3-propanediol (Tris-base), 3-(4,5-dimethyl-2-thiazolyl)-2,5-diphenyltetrazolium bromide (MTT), and 5,5-dimethyl-1-pyrroline N-oxide (DMPO) were purchased from Sigma Aldrich Inc. Roswell Park Memorial Institute (RPMI) medium 1640, Lysogeny broth (LB) medium, fetal bovine serum (FBS), 4',6-diamidino-2-phenylindole (DAPI), and propidium iodide (PI) were purchased from Thermo Fisher Scientific Inc. The deionized (DI) water ($18.2\text{ M}\Omega\cdot\text{cm}$) was produced from a Millipore water purification system. Male C57BL/6 mice of 6-8 weeks old were purchased from Charles River. *E. coli* O157:H7 strain (ATCC 43888), *S. aureus* strain (ATCC 13301) and the macrophage cell line (MH-S) were obtained from the American Tissue Culture Collection (ATCC). The colon cancer cell line (SW620) was provided by MD Anderson Cancer Center.¹⁵² All experiments involved in animals were approved by the Institutional Animal Care and Use Committee (IACUC) in University of North Dakota. All oligonucleotides were synthesized by IDT Inc. The G-quadruplex sequence was B7-3-0 (5'- ATT GGG AGG GAT TGG GTG GG -3').¹⁵³

2.2. Instruments.

UV-Vis absorption measurements were performed on a PerkinElmer Lambda 1050 UV/vis/NIR spectrometer (PerkinElmer, Santa Clara, CA), equipped with a Peltier temperature control accessory. Fluorescence intensities were measured using a Horiba Fluorolog-3 spectrofluorometer. The fluorescence images were taken using a Nikon Eclipse 80i (upright) fluorescence microscope. A Hitachi SU8010 field emission

scanning electron microscope (SEM) was used to take the SEM images of the H₂O₂-treated bacteria. The optical density (OD) values of sample solution for MTT assays were measured at 560 nm using a multiskan spectrum spectrophotometer (Thermofisher Scientific, Waltham, MA).

2.3. Preparation of DNAzyme.

Hemin solution (4.0 mM) was first dissolved in 5 mL of DMSO as the stock solution. The oligonucleotide of 100 nmol was dissolved in 1 mL of Tris-EDTA (TE) buffer and stored at -20 °C. An aliquot of 200 µL of obtained oligonucleotide solution was heated to 95 °C and was kept at this temperature for 5 min and then cooled to room temperature and remained for 60 min to dissociate any intermolecular interactions. Subsequently, an aliquot of 5 µL of 0.1 M KCl solution was added to the oligonucleotide solution and was incubated at room temperature for 40 min. Finally, an aliquot of 2.6 µL of hemin stock solution was added up to a concentration of 50 µM and was incubated at room temperature for 60 min. The formed G/H complexes were diluted to required concentrations using Tris-HCl buffer (25 mM, pH 6.8) prior to usage.

2.4. Culture of Bacteria and Detection of Antibacterial Activity of the Developed Reagents.

Monocolony bacteria of *E. coli* and *S. aureus* were cultured in the LB medium and shaken at 37 °C overnight before usage.¹⁵⁴ The bacterial cells were collected by centrifuging and re-dispersed in Tris-HCl buffer with an optical density of 1 at 600 nm (OD₆₀₀).¹⁵⁵ Then, the bacteria were diluted to 10⁶ CFU mL⁻¹ using a sterile Tris-HCl buffer. The as-prepared bacterial solution was mixed with different concentrations of G/H complex and H₂O₂, incubating at 37 °C for 30 min under shaking. Then, an aliquot of 100 µL of the bacterial suspension was added into 900 µL of LB medium for growth in a shaking incubator at 37 °C overnight. The concentration of bacteria was finally

determined by counting the numbers of bacterial colonies on plates.¹⁵⁶

2.5. Study of the Cell Wall/Membrane Integrity.

An aliquot of 20.0 μL of log phase *E. coli* (10^9 CFU mL^{-1}) cells was dispersed in 200 μL of Tris–HCl buffer with or without 1 μL of 0.2 mM G/H complex. After incubation for 2 h at 37 °C, the bacteria were stained with 200 μL of DAPI (12.50 $\mu\text{g}/\text{mL}$) and PI (1.25 $\mu\text{g}/\text{mL}$) for 15 min under the dark.¹⁵⁷ Then the collected cells were imaged using a Nikon Eclipse 80i (upright) fluorescence microscope.

2.6. *In Vivo* Mouse Wound Model.

A mouse wound model¹³⁰⁻¹³¹ was used to evaluate the anti-infection efficiency of H_2O_2 in the G/H complex *in vivo*. A total of 15 male mice with about 4 mm^2 wound area were divided into five groups to be treated with different solutions: 0.1 M H_2O_2 , saline, 1 μM G/H complex, 1 mM H_2O_2 , and 1 mM H_2O_2 + 1 μM G/H complex. After a wound was created, an aliquot of 50 μL of *S. aureus* (1×10^8 CFU/mL) was first placed on the wound area, followed by covering with an absorbent wound dressing infused with 50 μL of different solutions, respectively. The reagents were added every 24 h and the photos of the wound area of each mouse were taken. After 72 h, the scabs of the wound were harvested and kept in PBS buffer. The numbers of bacteria were quantified by counting the colonies on the agar plate.

2.7. Cytotoxicity of G/H Complex Used as Additive.

The bacteria *E. coli* and *S. aureus* were seeded in 96-well plates and treated with various concentrations of the G/H complex at 37 °C for 5 h. Then, each well was added by 10 μL of 5 mg/mL MTT reagent to form the purple products after 4 h, followed by adding 100 μL of DMSO solution to stop the reaction and dissolve the precipitant thoroughly.¹⁵⁸ The absorption of each well at 570 nm was recorded to determine the cell survival rate.

SW620 cells and MH-S cells were cultured in 1640 medium supplemented with 10% FBS at 37 °C overnight.¹⁵² Both cells were treated with various concentrations of the G/H complex at 37 °C for 24 h. Then, the MTT method was performed to determine cell viability.

2.8. Spin Trapping Technique Using Electron Paramagnetic Resonance for Detection of ·OH.

Approximately 30 µL of sample was loaded into a borosilicate capillary tube (0.70 mm i.d./1.25 mm o.d.; VitroGlass, Inc.), which was mounted in a Varian E-109 spectrometer fitted with a cavity resonator. All continuous wave (CW) EPR spectra were obtained with an observation power of 12.5 mW. All spectra were obtained with a modulation frequency of 100 kHz and a modulation amplitude of 1 G. The spin trap agent DMPO was used to capture the formed ·OH.

3. Results and Discussion

3.1. Formation of A Hydroxyl Radical from H₂O₂ by G/H DNAzyme.

The formation of ·OH through chemical decomposition of H₂O₂ catalyzed by G/H DNAzyme is the critical step in our design. So far, this reaction has not been demonstrated in the literature. In 2016, Cai and co-workers developed a fluorometric assay platform for the detection of caffeic acid based on the oxidation of the intermediate from decomposition of H₂O₂ catalyzed by G/H DNAzyme, but it was not proved whether the intermediate was ·OH or not.¹⁵⁹

The challenge was how to accurately measure the produced ·OH in the reaction process. The lifetime of ·OH in solution is about 10⁻⁹ s, making it extremely difficult to be detected.¹⁶⁰ Based on the spin trapping technique, electron paramagnetic resonance (EPR) has been applied to detect ·OH.¹⁶¹⁻¹⁶³ As shown in Figure 27, a typical

spectrum of DMPO-OH, which was in 1: 2: 2: 1 quartet format,¹⁶¹ was presented in the presence of the complex. However, there was no distinctive or special spectrum for control without the G/H complex. Although EPR is only a semiquantitative approach for detecting $\cdot\text{OH}$, the result qualitatively confirmed the formation of $\cdot\text{OH}$ during the reaction catalyzed by the G/H complex.

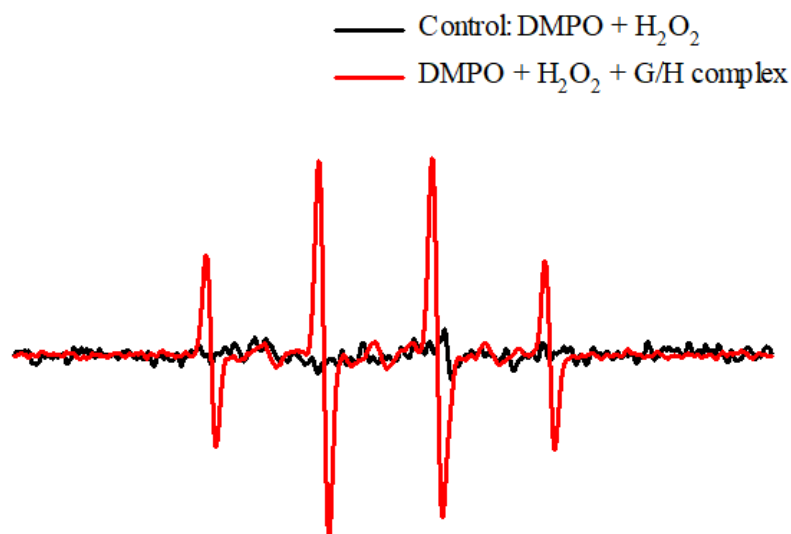


Figure 27. CW EPR spectra of DMPO-OH. Conditions: 10 mM H₂O₂, 25 μM G/H complex, 500 mM DMPO in 25 mM Tris-HCl buffer (pH 6.8), incubation at room temperature for 30 min. Signal average time is 20-25 min for each sample.

Meanwhile, an indirect method was performed to further demonstrate the formation of $\cdot\text{OH}$. According to the literature, the generated $\cdot\text{OH}$ could be monitored using a fluorescence method in which TA could capture $\cdot\text{OH}$ and generate fluorescent 2-hydroxy terephthalic acid (TAOH) with a fluorescence emission peak at 435 nm.^{130, 164-165} Based on this information, the TA might be an ideal probe for investigation of the formation of $\cdot\text{OH}$ in a reaction. Thus, in this work, we adopted this fluorescence method to confirm the formation of $\cdot\text{OH}$. First, we prepared G/H DNAzyme as described in section 2.3. Then, to verify the generation of $\cdot\text{OH}$ in the decomposition of H₂O₂, a series of fluorescence measurements were conducted using different

solutions. The results were shown in Figure 28. When only TA existed in the solution, no fluorescence signals were observed (curve a). At this moment, the G/H complex was added to the TA solution. Still, no fluorescence signals were obtained (curve b). These results showed that both TA and the G/H complex are not fluorescence materials. In parallel, a TA solution containing H_2O_2 was detected (curve c). A small fluorescence peak at 435 nm was shown in curve c. The fluorescence peak indicated that the individual H_2O_2 can oxidize TA and release $\cdot OH$ spontaneously. However, when the G/H complex was added as an additive, the fluorescence intensity increased dramatically (curve d). The comparison of fluorescence enhancement between curve c and d was shown in the inset of Figure 28. It was about an 8 times increase in intensity compared to the solution without the G/H complex. The results clearly demonstrated the ability of the G/H complex to convert H_2O_2 to $\cdot OH$.

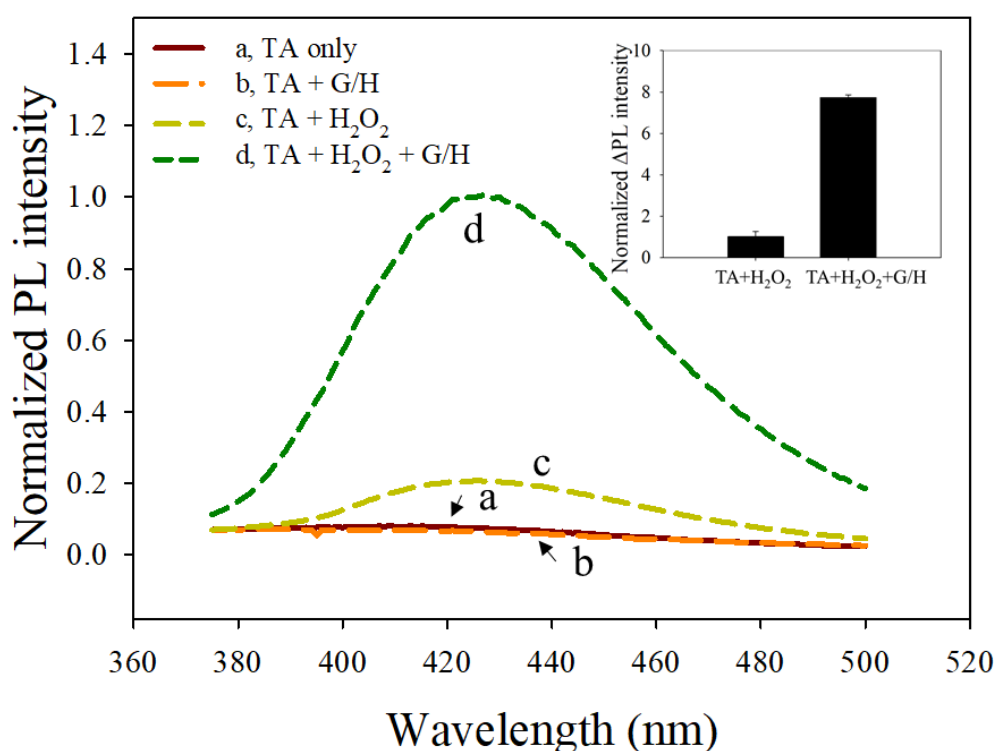


Figure 28. Normalized fluorescence spectra of TAOH formed under different conditions, including only TA (curve a); TA and G/H complex (curve b) ; TA and H_2O_2

(curve c); and TA, H₂O₂, and G/H complex (curve d). Conditions: 20 mM PBS buffer (pH 7.4), incubation at room temperature for 12 h. The concentrations of TA, H₂O₂, and the G/H complex were 0.5 mM, 1 mM, and 1 μM, respectively. λ_{ex}: 315 nm, λ_{em}: 435 nm. Inset: the normalized ΔPL intensity with or without the G/H complex.

3.2. Optimization of the Peroxidase-Mimic Activity of the G/H DNAzyme.

In order to achieve the highest production efficiency of the ·OH radical, we optimized the peroxidase-mimic activity of the synthesized G/H complex. The G/H complex is a DNAzyme in which the hemin molecules bound with their guanine-rich single-stranded DNA (ssDNA) aptamers, forming a quadruplex structure with the hydrogen bond between guanine bases. Here, we first synthesized a G/H complex with a reported high peroxidase-mimic activity structure, B7-3-0⁴¹. The experimental procedure was described in section 2.3. The peroxidase-mimic activity of the synthesized G/H complex was proved by catalytic oxidation of ABTS in the presence of H₂O₂. As shown in Figure 29A, only the group with both H₂O₂ and G/H complex led to the color change from translucent green to dark green. This qualitatively demonstrated the peroxidase-mimic activity of G/H complex. The result was also verified by UV-Vis absorption at 420 nm (Figure 29B).

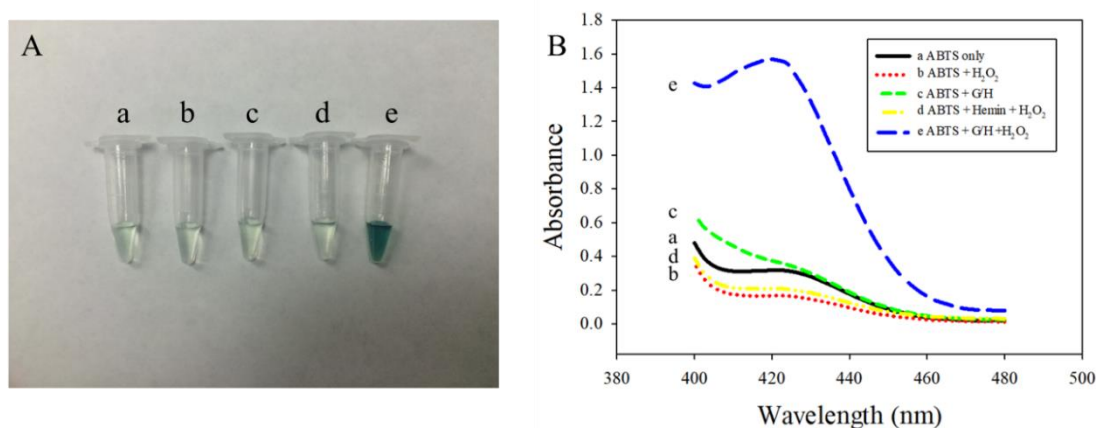


Figure 29. Peroxidase-mimic property verification by directly monitoring the color change (A) and UV- Vis spectra (B) of 5 mM ABTS solution in 25 mM Tris-HCl buffer (pH 6.8) containing (a) ABTS only; (b) 5 mM H₂O₂; (c) 1 μM G/H complex; (d) 5 mM H₂O₂ + 1 μM Hemin; (e) 5 mM H₂O₂ + 1 μM G/H complex. Incubation at room temperature for 10 min.

The peroxidase-like activity of the G/H complex was evaluated by the initial velocity V_0 of formed oxidized ABTS⁺.^{153, 166-167} As shown in Figure 30A and B, the V_0 value increased from 104 nM/s at 25 °C with increasing temperature. The result was similar to the literature, describing that G/H complex was thermophilic.¹⁶⁶ Considering the antibacterial applications to various biological samples, the temperature higher than 37 °C was not optimal. Herein, 37 °C was chosen as the working temperature. Besides temperature, the pH value also affected the oxidation extent significantly. As shown in Figure 30C, the V_0 value was very small in acidic conditions (pH 1.0-6.0). It showed large values in neutral pH to weak alkali conditions (pH 7.0-10.0). The optimal pH of the G/H complex was pH 8.0. Considering the small difference with optimum and application scenarios on skins, a Tris-HCl (pH 6.8) buffer was chosen as the reaction medium in the following work.

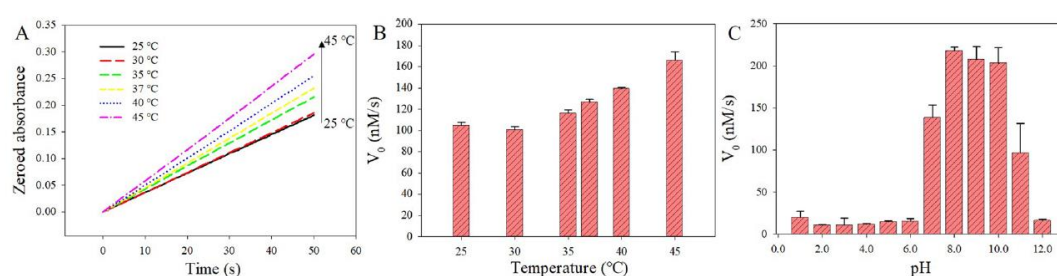


Figure 30. Optimization of peroxidase-mimic activity of G/H complex: (A) Plots of absorbance at 420 nm versus G/H complex at different temperatures. Experiments were performed using the 1 μ M G/H complex and 1 mM H₂O₂ in 25 mM Tris-HCl buffer (pH 6.8) with 2 mM ABTS work solution at different temperatures. (B) V_0 values of the G/H complex at different temperatures. (C) V_0 values of the G/H complex at different pH. Experiments were performed using 1 μ M G/H complex and 1 mM H₂O₂ in 2 mM ABTS working solution at 37 °C at different pH.

3.3. Enhanced Antibacterial Property of H₂O₂ by G/H Complex.

The G/H complex has demonstrated catalytic capacity on reduction of H₂O₂ to release the \cdot OH radical. Our objective is to enhance the antibacterial activity of H₂O₂. Next, using both Gram-negative bacteria *E. coli* and Gram-positive bacteria *S. aureus*, we investigated the ability of the G/H complex to facilitate antibacterial activity of H₂O₂.

As shown in Figure 4.5A, the potency of pure H₂O₂ in killing *E. coli* was examined and was shown to be in a dose-dependent manner. The higher the concentration of H₂O₂ was, the lower the bacterial survival rate was. As shown in Figure 31A curve a, the H₂O₂ concentration increased from 10⁻⁸ to 10⁻¹ M, the bacterial survival rate decreased from 100% to 0%. However, when the G/H complex was added, the bacterial viability significantly decreased compared to that without the G/H complex. As shown in Figure 31A curve b, a concentration of 1 mM H₂O₂ could reach 0% bacterial survival rate while 0.1 M H₂O₂ was needed to achieve a similar effect for pure H₂O₂, two orders of magnitude lower, and is a relatively safe H₂O₂ concentration for clinical application.

The improved antibacterial activity was also demonstrated by inhibiting the growth of *E. coli* (Figure 31B). The same amount of *E. coli* was incubated in three cell culture media: the regular LB medium, the regular LB medium + 0.01 M H₂O₂, and the regular LB medium + 0.01 M H₂O₂ + 1 μM G/H complex. The bacterial concentration was measured by detection of OD₆₀₀. After 1 h of incubation, the *E. coli* concentration was 0.27±0.01 (LB only), 0.22 ±0.01 (LB + H₂O₂), and 0.21 ±0.01 (LB+ H₂O₂+G/H complex) (Figure 31B, black columns). At this moment the bacterial concentration was comparable in these three media. Then, the culture time for the bacterial cells was extended to 5 h (Figure 31B, red columns). The bacterial concentration was increased to 0.70 ±0.02 and 0.35±0.02 in the regular LB medium and LB+H₂O₂ medium, respectively. However, in the LB+H₂O₂ + G/H complex medium, the bacterial growth was limited to 0.23±0.01. The student *t* test showed a significant difference between the G/H complex group and these two control groups. These results indicated the bacterial cells were able to grow in the presence of 0.01 M H₂O₂. However, as the addition of the G/H complex presented, the growth of bacteria was greatly inhibited.

Thus, the G/H complex improved the antibacterial activity of H₂O₂ for Gram-positive bacteria.

We further tested Gram-negative bacteria, *S. aureus*, using the same method. The results were shown in Figure 31C and D. Compared with Figure 31A and B, both the bacterial survival rate and the bacterial quantity are similar to the Gram-positive bacteria. Therefore, the G/H complex could be used to enhance the antibacterial activity of H₂O₂ for both Gram-negative and Gram-positive bacteria.

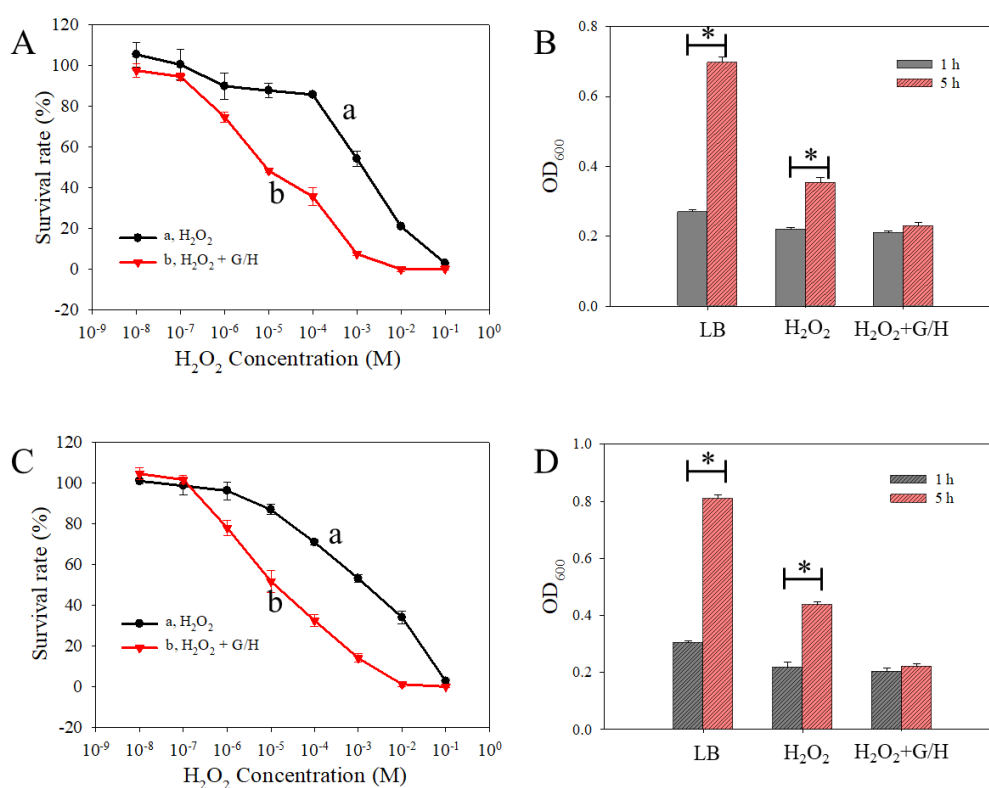


Figure 31. A, Survival rate of *E. coli* treated with H₂O₂ at different concentration coinubation (10⁻⁸, 10⁻⁷, 10⁻⁶, 10⁻⁵, 10⁻⁴, 10⁻³, 10⁻², 10⁻¹ M) with or without 1 μM G/H complex. Incubation at 37 °C for 30 min in Tris-HCl buffer. B, Growth inhibition experiment by incubation in 0.01 M H₂O₂ with or without a 1 μM G/H complex at 37 °C in different medium solutions at 1 and 5 h. *p < 0.01. C and D for Gram-negative bacteria, *S. aureus*. The experimental conditions are similar to A and B.

To visualize the above results, the antibacterial activity of the designed complex was further investigated using the CFU counting method. As shown in Figure 32, the top panel was *E. coli* cells, and the bottom panel was *S. aureus* cells. After being

treated with 0.01 M H₂O₂ (Figure 32 C and G), the bacterial colonies formed on the LB-agar plate were much less than the control groups (Figure 32 A and E, B and F). However, when the bacteria groups were treated within the G/H complex + 0.01 M H₂O₂ (D and H), the colony counts significantly reduced. Noticeably, there was no *E. coli* colony formed after treating with 0.01 M H₂O₂ and the 1 μM G/H complex (Figure 32D). This result further supported the concept that the G/H complex can enhance the antibacterial activity.

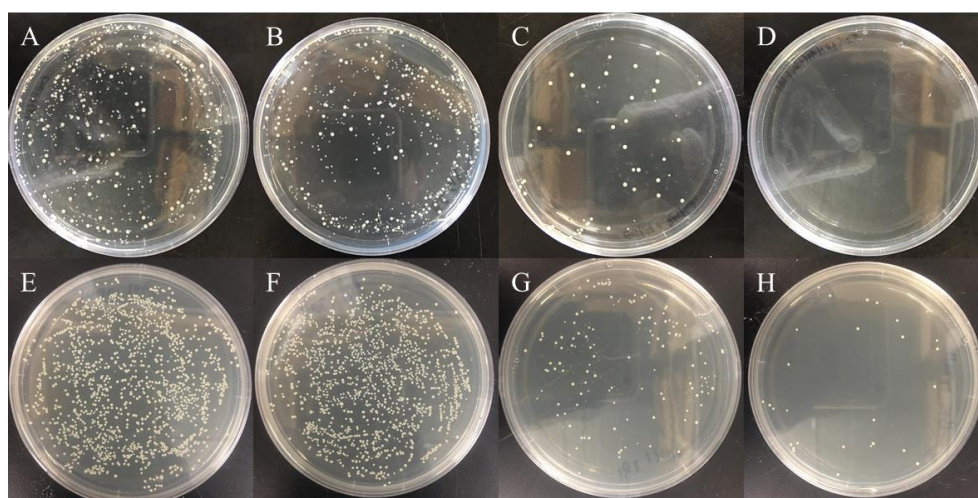


Figure 32. Representative photos of bacterial colonies showing the influences of the catalytic activity of the G/H complex on the growth of *E. coli*. (up) and *S. aureus* (bottom). (A and E) bacterial cells only; (B and F) bacteria with 1 μM G/H complex; (C and G) bacteria with 0.01 M H₂O₂; (D and H) bacteria with 0.01 M H₂O₂ + 1 μM G/H complex. Incubation at 37 °C for 30 min.

3.4. Effect of G/H Complex on Bacterial Cell Membrane Integrity.

To further explore the antibacterial mechanism of G/H complex assisted H₂O₂, the bacterial cell wall/membrane integrity was examined using *E. coli* as an example bacterium. Two fluorescent molecules, DAPI and PI, were used to stain the *E. coli* cells. According to the literature¹⁶⁸⁻¹⁶⁹, DAPI can stain all cells, while PI can only stain membrane damaged cells. As shown in Figure 33A, the bacteria without treatment showed a few red spots stained by PI, demonstrating that most of the bacterial cells were alive. The bacterial group treated with the G/H complex only (B) showed the

similar results with group A. Only a few bacterial cells stained by PI indicated that there was no direct harm of the G/H complex on bacteria. After treating bacteria with 0.01 M H₂O₂ for 2 h (C), more cells were stained by the red color. Pink staining that indicates colocalization was observed in the merged image in addition to a number of DAPI only stained cells. In this condition, about half of the bacterial cells were killed by H₂O₂. Compared to these three control groups, in the presence of the G/H complex + H₂O₂ (Figure 33D), most of the *E. coli* cells were stained by both DAPI and PI, implying damage on the cell wall/membranes. Therefore, the existence of the G/H complex in the system facilitates the destruction of the bacteria cell wall/membrane.

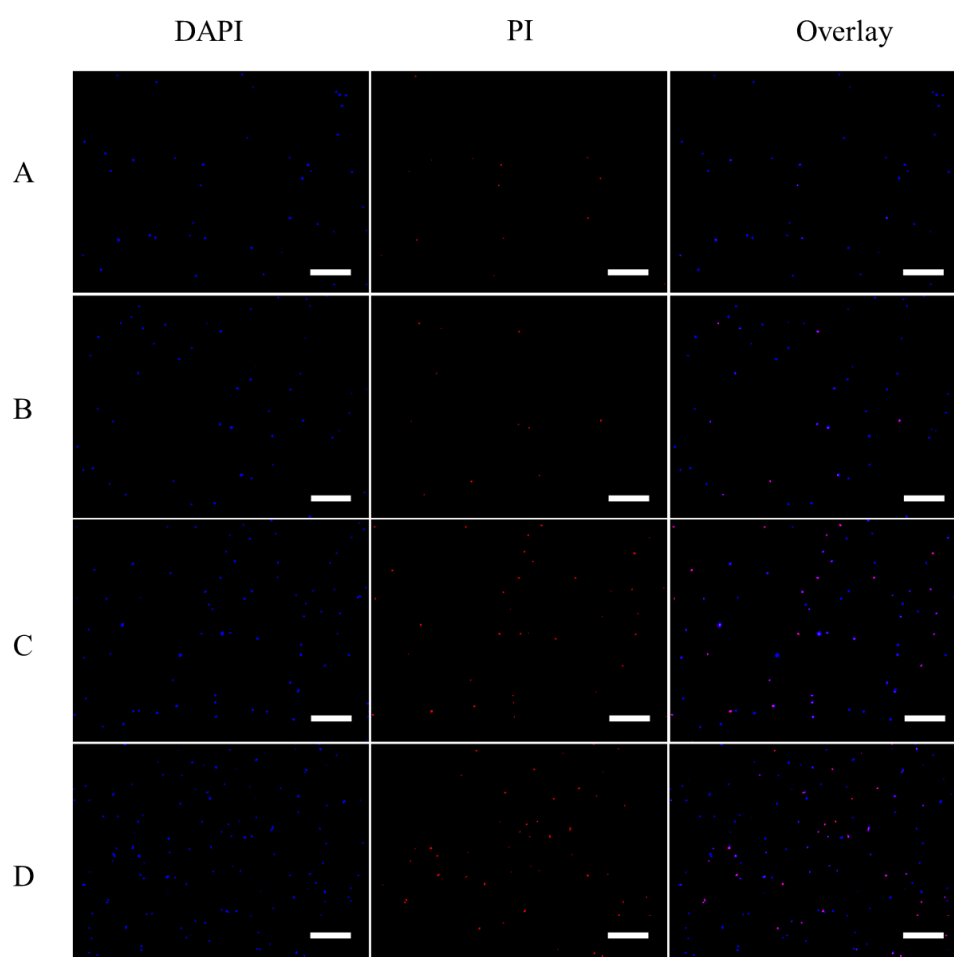


Figure 33. Fluorescence images of live and dead *E. coli* cells after incubation with 10 mM H₂O₂ for 2 h: (A) *E. coli* only; (B) *E. coli* with 1 μM of G/H complex; (C) *E. coli* with 0.01 M H₂O₂; (D) *E. coli* with 0.01 M H₂O₂ + 1 μM G/H complex. Blue fluorescence shows bacterial quasinuclear staining with DAPI, while red fluorescence shows dead bacteria staining with PI. Bar scale: 20 μm.

Scanning electron microscopy was also used to directly observe the change of the bacterial cell wall/membrane after treating with different drug solutions. As shown in Figure 34, for two negative control groups treated with saline and G/H complex (Figure 34A and 34B), the *E. coli* cells were still in the ordinary rod shape, with relatively smooth cell walls. It demonstrated that the cells in these two groups were still healthy. After treating with 0.01 M H₂O₂ (Figure 34C), the bacterial cell walls/membranes became unsmooth with some irregular asperities because of the H₂O₂ damage. Remarkably, after treating with the H₂O₂ +G/H complex (Figure 34D), the morphology of the whole cell wall became rough. To further confirm this result, we investigated the morphology change of *S. aureus* (Figure 34, bottom panel). The resulting SEM images were similar to that of *E. coli* (Figure 34E-H). Both bacterial SEM images demonstrated that the G/H complex could obviously enhance the antibacterial activity of H₂O₂. The enhancement manner was directly killing bacteria but through the additive G/H complex as an auxiliary.

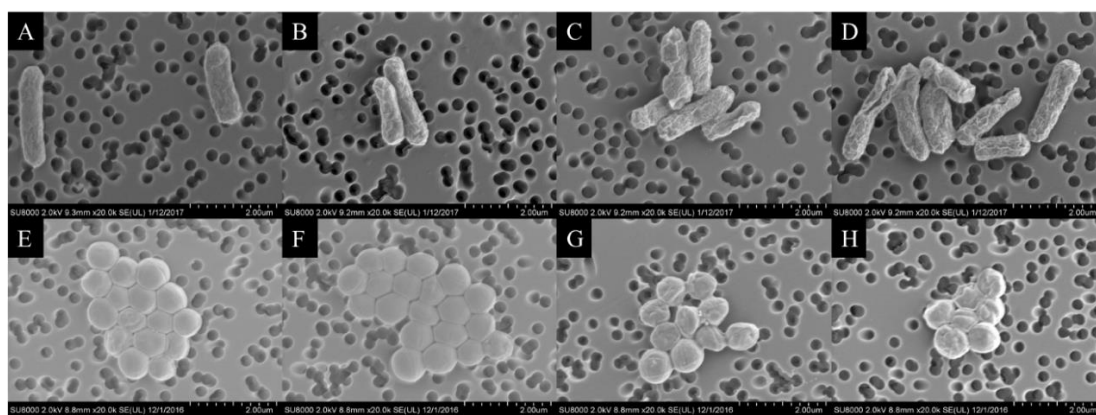


Figure 34. SEM images of bacterial morphology. (A) *E. coli*; (B) *E. coli* incubated with 1 μ M G/H complex; (C) *E. coli* incubated with 0.01 M H₂O₂; (D) *E. coli* incubated with 0.01 M H₂O₂ and 1 μ M G/H complex; (E) *S. aureus*; (F) *S. aureus* incubated with 1 μ M G/H complex; (G) *S. aureus* incubated with 0.01 M H₂O₂; (H) *S. aureus* incubated with 0.01 M H₂O₂ and 1 μ M G/H complex. Incubation at 37°C for 30 min.

3.5. Anti Infection Effect of the G/H Complex on Wound Healing.

To expand the antibacterial applications of the G/H complex *in vivo*, the anti-

infection efficiency of the G/H complex was investigated using back-wounded mice as a model.^{130-131, 170} The wounds on the mice were artificially made under similar conditions. Then, *S. aureus* bacterial cells were placed on the wound to accelerate wound infection. Then, five groups of mice were treated with 0.1 M H₂O₂, saline, 1 μM G/H complex, 1 mM H₂O₂, and 1 μM G/H complex +1 mM H₂O₂, respectively. Three mice in each group were used for parallel experiments. With a 24 h interval, new absorbent wound dressings infused with new treating solutions were covered on the wound, and the wound recovery processes were recorded by camera (Figure 35). The effective concentration of H₂O₂ was 1 mM, which was much lower than the commercial H₂O₂ products (166 mM to 1 M) for wound disinfection. After treating the wounds with H₂O₂ + G/H complex for 72 h, the wounds on mice were almost fully healed without any erythema and edema. Although the wounds on mice in the 1 mM H₂O₂ group also healed significantly, the area around the wound was slightly red and swollen compared to the group treated with the H₂O₂+ G/H complex. Unlike the groups treated with H₂O₂, the wounds of mice in saline and the G/H complex group showed the regular inflammatory reaction during wound healing processes. Some erythema and edema were found during the 72 h treatment. This result demonstrated that the combination of the G/H complex with H₂O₂ could also play a role in resisting wound infection and accelerating wound healing *in vivo*. Additionally, the group treated with a relative high level of H₂O₂ (0.1 M) showed a more adverse outcome on the skin. This concentration of H₂O₂ aggravated the damage of skin, rather than healing. Collectively, these findings illustrated the significance of reducing H₂O₂ concentration for wound healing.

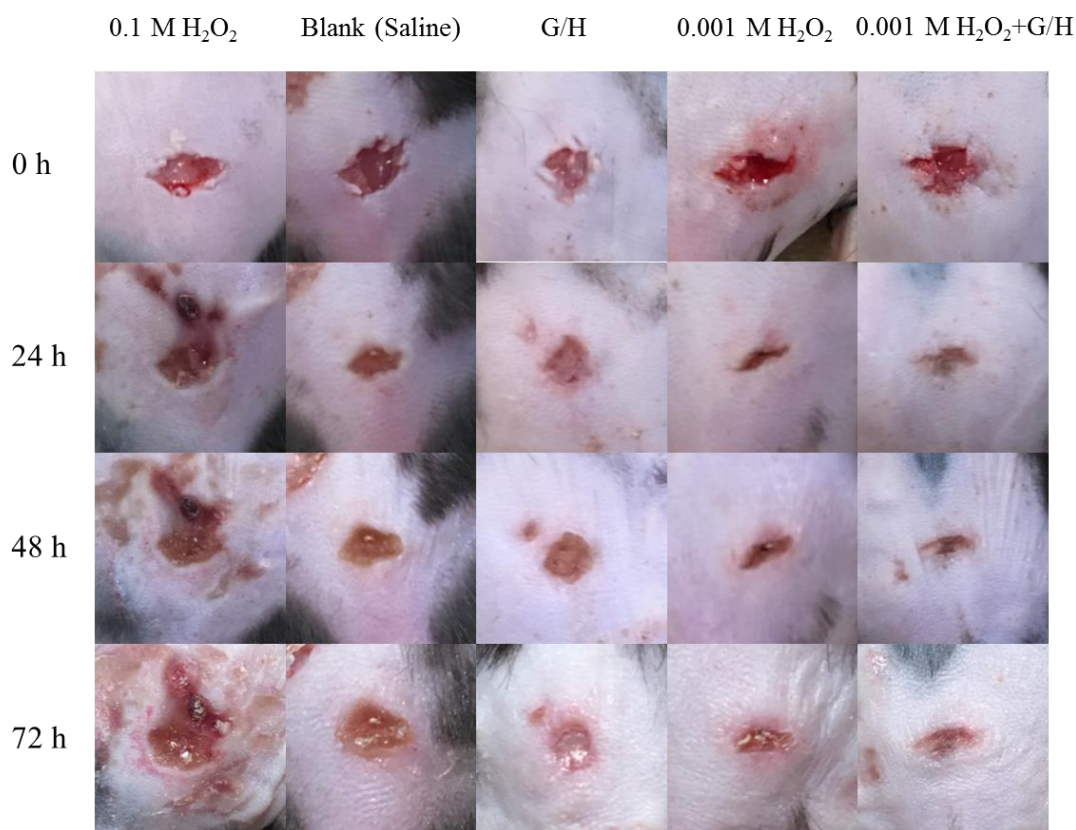


Figure 35. Photographs of wounds on mice treated with different solutions (0.1 M H₂O₂, saline, 1 μM G/H complex, 1 mM H₂O₂, 1 μM G/H complex + 1 mM H₂O₂) at indicated times.

3.6. Cytotoxicity Study of the G/H Complex.

One of the main purposes of this work is to decrease the health tissue damage when using H₂O₂ as antiseptics. *In vitro* antibacterial experiments demonstrated that G/H itself was not harmful to bacteria (Figure 4.6B and F, Figure 4.8B and F). To further investigate the cytotoxicity of the G/H complex toward bacteria and mammalian cells, the MTT assay was performed. Two bacteria (*E. coli* and *S. aureus*) and two mammalian cell lines, a macrophage cell line (MH-S) and a colon cancer cell line (SW620), were used. The cell viabilities of bacteria and mammalian cell lines were measured after incubating with different concentrations of G/H complex for 5 and 24 h, respectively. As shown in Figure 36, for both bacteria and mammalian, almost 100% of the cells were still alive after incubation with the G/H complex in the range of 0 to 20 μM, which

was about 20-fold higher than its working concentration. When the concentration went to higher range (up to 60 μM), the cell survival rate started to decrease, but above 80%. This suggests a low intrinsic toxicity to cells at a high concentration, which is mostly derived from the toxicity of hemin.¹⁷¹⁻¹⁷² However, there is no cytotoxicity of the G/H complex used as an additive at low concentrations, making the G/H complex a biocompatible agent for disinfection.

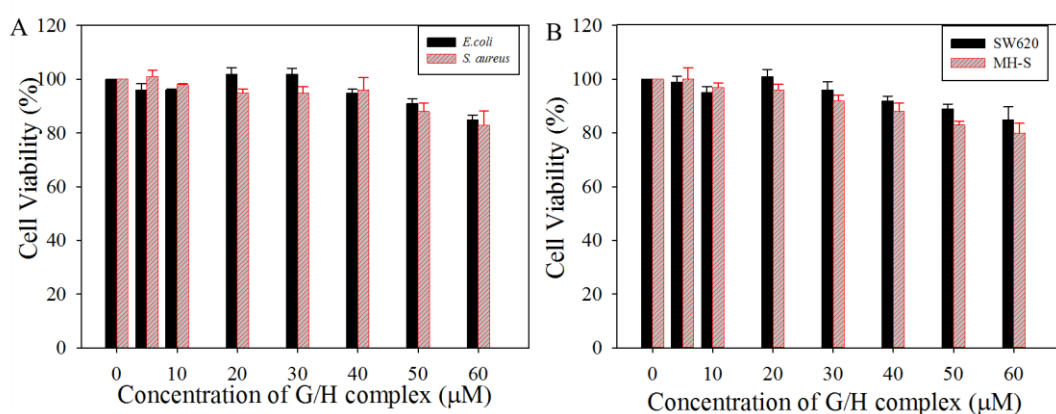


Figure 36. Relative cell viability of *E. coli* and *S. aureus* (A) and SW620 and MH-S (B) after culturing with different concentrations of G/H complex (0, 5, 10, 20, 30, 40, 50 to 60 μM). Incubation conditions: 5 h for bacteria, 24 h for SW620 and MH-S at 37 $^{\circ}\text{C}$.

4. Conclusions

In conclusion, the G/H complex was designed and used as an additive to H_2O_2 to achieve the same antibacterial effect in a much lower dose of H_2O_2 . By converting H_2O_2 into $\cdot\text{OH}$, higher antibacterial activity was achieved through catalyzing the decomposition of H_2O_2 . Therefore, low concentrations of H_2O_2 can be used to kill bacteria with a high efficiency with little harmful effects to healthy tissues. The addition of the G/H complex showed excellent antibacterial properties against both Gram-negative (*E. coli*) and Gram-positive (*S. aureus*) bacteria *in vitro* without significant cytotoxicity. Furthermore, the G/H complex based antibacterial system also showed outstanding anti-infection property *in vivo* on a mouse wound model. Overall, the

intrinsic properties of oligonucleotides made the G/H complex an ideal additive in industry.

REFERENCES

1. da Silva, A. D.; Barbosa, F. Jr; Scarano, W. R., Oral Exposure to Methylmercury Modifies the Prostatic Microenvironment in Adult Rats. *Int. J. Exp. Pathol.* **2012**, *93*, 354–360.
2. Schneider, L.; Peleja, R. P.; Kluczkovski, A.; Freire, G. M.; Marioni, B.; Vogt, R. C.; Da Silveira, R., Mercury Concentration in the Spectacled Caiman and Black Caiman (Alligatoridae) of the Amazon: Implications for Human Health. *Arch. Environ. Contam. Toxicol.* **2012**, *63*, 270-279.
3. Yu, T.; Zhang, T. T.; Zhao, W.; Xu, J. J.; Chen, H. Y., A Colorimetric/Fluorescent Dual-Mode Sensor for Ultra-Sensitive Detection of Hg²⁺. *Talanta* **2017**, *165*, 570-576.
4. Rebelo, F. M.; Caldas, E. D., Arsenic, Lead, Mercury and Cadmium: Toxicity, Levels in Breast Milk and the Risks for Breastfed Infants. *Environ. Res.* **2016**, *151*, 671-688.
5. Lamborg, C. H.; Hammerschmidt, C. R.; Bowman, K. L.; Swarr, G. J.; Munson, K. M.; Ohnemus, D. C.; Lam, P. J.; Heimbürger, L. E.; Rijkenberg, M. J. A.; Saito, M. A., A Global Ocean Inventory of Anthropogenic Mercury Based on Water Column Measurements. *Nature* **2014**, *512*, 65-68.
6. Farina, M.; Avila, D. S.; da Rocha, J. B. T.; Aschner, M., Metals, Oxidative Stress and Neurodegeneration: A Focus on Iron, Manganese and Mercury. *Neurochem. Int.* **2013**, *62*, 575-594.
7. Chen, S.; Liu, D.; Wang, Z.; Sun, X.; Cui, D.; Chen, X., Picomolar Detection of Mercuric Ions by Means of Gold–Silver Core–Shell Nanorods. *Nanoscale* **2013**, *5*, 6731-6735.
8. Ou, L.; Chen, C.; Chen, L.; Wang, H.; Yang, T.; Xie, H.; Tong, Y.; Hu, D.; Zhang, W.; Wang, X., Low-Level Prenatal Mercury Exposure in North China: An Exploratory Study of Anthropometric Effects. *Environ. Sci. Technol.* **2015**, *49*, 6899-6908.
9. Buck, K. A.; Varian-Ramos, C. W.; Cristol, D. A.; Swaddle, J. P., Blood Mercury Levels of Zebra Finches Are Heritable: Implications for the Evolution of Mercury Resistance. *PLoS ONE* **2016**, *11*, e0162440.
10. Manna, B.; Raj, C. R., Nanostructured Sulfur-Doped Porous Reduced Graphene Oxide for the Ultrasensitive Electrochemical Detection and Efficient Removal of Hg(II). *ACS Sustain. Chem. Eng.* **2018**, *6*, 6175-6182.
11. Niece, B. K.; Hauri, J. F., Determination of Mercury in Fish: A Low-Cost Implementation of Cold-Vapor Atomic Absorbance for the Undergraduate

Environmental Chemistry Laboratory. *J. Chem. Educ.* **2013**, *90*, 487-489.

12. Tan, D.; He, Y.; Xing, X.; Zhao, Y.; Tang, H.; Pang, D., Aptamer Functionalized Gold Nanoparticles Based Fluorescent Probe for the Detection of Mercury (II) Ion in Aqueous Solution. *Talanta* **2013**, *113*, 26-30.

13. Wang, H.; Wang, Y.; Jin, J.; Yang, R., Gold Nanoparticle-Based Colorimetric and “Turn-on” Fluorescent Probe for Mercury(II) Ions in Aqueous Solution. *Anal. Chem.* **2008**, *80*, 9021-9028.

14. Bagheri, H.; Naderi, M., Immersed Single-Drop Microextraction–Electrothermal Vaporization Atomic Absorption Spectroscopy for the Trace Determination of Mercury in Water Samples. *J. Hazard. Mater.* **2009**, *165*, 353-358.

15. Ding, X.; Kong, L.; Wang, J.; Fang, F.; Li, D.; Liu, J., Highly Sensitive Sers Detection of Hg²⁺ Ions in Aqueous Media Using Gold Nanoparticles/Graphene Heterojunctions. *ACS Appl. Mater. Interfaces* **2013**, *5*, 7072-7078.

16. Saha, K.; Agasti, S. S.; Kim, C.; Li, X.; Rotello, V. M., Gold Nanoparticles in Chemical and Biological Sensing. *Chem. Rev.* **2012**, *112*, 2739-2779.

17. Daniel, M. C.; Astruc, D., Gold Nanoparticles: Assembly, Supramolecular Chemistry, Quantum-Size-Related Properties, and Applications toward Biology, Catalysis, and Nanotechnology. *Chem. Rev.* **2004**, *104*, 293-346.

18. Zeng, S.; Yong, K. T.; Roy, I.; Dinh, X. Q.; Yu, X.; Luan, F., A Review on Functionalized Gold Nanoparticles for Biosensing Applications. *Plasmonics* **2011**, *6*, 491.

19. Li; Rothberg, L. J., Label-Free Colorimetric Detection of Specific Sequences in Genomic DNA Amplified by the Polymerase Chain Reaction. *J. Am. Chem. Soc.* **2004**, *126*, 10958-10961.

20. Liu, C. W.; Hsieh, Y. T.; Huang, C. C.; Lin, Z. H.; Chang, H. T., Detection of Mercury(Ii) Based on Hg²⁺-DNA Complexes Inducing the Aggregation of Gold Nanoparticles. *Chem. Commun. (Camb)* **2008**, *19*, 2242-2244.

21. Du, J.; Zhu, B.; Chen, X., Urine for Plasmonic Nanoparticle-Based Colorimetric Detection of Mercury Ion. *Small* **2013**, *9*, 4104-4111.

22. Montano, M. D.; Olesik, J. W.; Barber, A. G.; Challis, K.; Ranville, J. F., Single Particle ICP-MS: Advances toward Routine Analysis of Nanomaterials. *Anal. Bioanal. Chem.* **2016**, *408*, 5053-5074.

23. Degueldre, C.; Favarger, P. Y., Colloid Analysis by Single Particle Inductively Coupled Plasma-Mass Spectroscopy: A Feasibility Study. *Colloids Surf. A Physicochem. Eng. Asp.* **2003**, *217*, 137-142.

24. Laborda, F.; Bolea, E.; Jimenez-Lamana, J., Single Particle Inductively Coupled Plasma Mass Spectrometry: A Powerful Tool for Nanoanalysis. *Anal. Chem.* **2014**, *86*,

2270-2278.

25. Han, G.; Xing, Z.; Dong, Y.; Zhang, S.; Zhang, X., One-Step Homogeneous DNA Assay with Single-Nanoparticle Detection. *Angew. Chem. Int. Ed. Engl.* **2011**, *50*, 3462-3465.

26. Deka, J.; Mech, R.; Ianeselli, L.; Amenitsch, H.; Cacho-Nerin, F.; Parisse, P.; Casalis, L., Surface Passivation Improves the Synthesis of Highly Stable and Specific DNA-Functionalized Gold Nanoparticles with Variable DNA Density. *ACS Appl. Mater. Interfaces* **2015**, *7*, 7033-7040.

27. Li, M.; Zhou, X.; Ding, W.; Guo, S.; Wu, N., Fluorescent Aptamer-Functionalized Graphene Oxide Biosensor for Label-Free Detection of Mercury(II). *Biosens. Bioelectron.* **2013**, *41*, 889-893.

28. Xie, Y., Colorimetric Determination of Hg(II) Via the Gold Amalgam Induced Deaggregation of Gold Nanoparticles. *Mikrochim. Acta* **2018**, *185*, 351.

29. Li, D.; Wieckowska, A.; Willner, I., Optical Analysis of Hg²⁺ Ions by Oligonucleotide-Gold-Nanoparticle Hybrids and DNA-Based Machines. *Angew. Chem. Int. Ed. Engl.* **2008**, *47*, 3927-3931.

30. Wang, F.; Sun, J.; Lu, Y.; Zhang, X.; Song, P.; Liu, Y., Dispersion-Aggregation-Dispersion Colorimetric Detection for Mercury Ions Based on an Assembly of Gold Nanoparticles and Carbon Nanodots. *Analyst* **2018**, *143*, 4741-4746.

31. Zhu, M.; Wang, Y.; Deng, Y.; Yao, L.; S, B. A.; Pan, D.; Xue, F.; Wu, Y.; Zheng, L.; Chen, W., Ultrasensitive Detection of Mercury with a Novel One-Step Signal Amplified Lateral Flow Strip Based on Gold Nanoparticle-Labeled Ssdna Recognition and Enhancement Probes. *Biosens. Bioelectron.* **2014**, *61*, 14-20.

32. Jia, S.; Bian, C.; Sun, J.; Tong, J.; Xia, S., A Wavelength-Modulated Localized Surface Plasmon Resonance (LSPR) Optical Fiber Sensor for Sensitive Detection of Mercury(II) Ion by Gold Nanoparticles-DNA Conjugates. *Biosens. Bioelectron.* **2018**, *114*, 15-21.

33. Chen, G. H.; Chen, W. Y.; Yen, Y. C.; Wang, C. W.; Chang, H. T.; Chen, C. F., Detection of Mercury(II) Ions Using Colorimetric Gold Nanoparticles on Paper-Based Analytical Devices. *Anal. Chem.* **2014**, *86*, 6843-6849.

34. Yang, L.; Yun, W.; Chen, Y.; Wu, H.; Liu, X.; Fu, M.; Huang, Y., Ultrasensitive Colorimetric and Fluorometric Detection of Hg(Ii) Based on the Use of Gold Nanoparticles and a Catalytic Hairpin Assembly. *Microchim. Acta* **2017**, *184*, 4741-4747.

35. Zhu, Y.; Cai, Y.; Zhu, Y.; Zheng, L.; Ding, J.; Quan, Y.; Wang, L.; Qi, B., Highly Sensitive Colorimetric Sensor for Hg(2+) Detection Based on Cationic Polymer/DNA Interaction. *Biosens. Bioelectron.* **2015**, *69*, 174-178.

36. Wu, X.; Mu, F.; Wang, Y.; Zhao, H., Graphene and Graphene-Based Nanomaterials

for DNA Detection: A Review. *Molecules* **2018**, *23*, 2050.

37. Liu, Y.; Dong, X.; Chen, P., Biological and Chemical Sensors Based on Graphene Materials. *Chem. Soc. Rev.* **2012**, *41*, 2283-2307.

38. Huang, X.; Yin, Z.; Wu, S.; Qi, X.; He, Q.; Zhang, Q.; Yan, Q.; Boey, F.; Zhang, H., Graphene-Based Materials: Synthesis, Characterization, Properties, and Applications. *Small* **2011**, *7*, 1876-1902.

39. Kim, J.; Cote, L. J.; Huang, J., Two Dimensional Soft Material: New Faces of Graphene Oxide. *Acc. Chem. Res.* **2012**, *45*, 1356-1364.

40. Liu, Z.; Liu, B.; Ding, J.; Liu, J., Fluorescent Sensors Using DNA-Functionalized Graphene Oxide. *Anal. Bioanal. Chem.* **2014**, *406*, 6885-6902.

41. Lu, C. H.; Yang, H. H.; Zhu, C. L.; Chen, X.; Chen, G. N., A Graphene Platform for Sensing Biomolecules. *Angew. Chem. Int. Ed. Engl.* **2009**, *48*, 4785-4787.

42. Alonso-Cristobal, P.; Vilela, P.; El-Sagheer, A.; Lopez-Cabarcos, E.; Brown, T.; Muskens, O. L.; Rubio-Retama, J.; Kanaras, A. G., Highly Sensitive DNA Sensor Based on Upconversion Nanoparticles and Graphene Oxide. *ACS Appl. Mater. Interfaces* **2015**, *7*, 12422-12429.

43. Li, M.; Zhou, X.; Guo, S.; Wu, N., Detection of Lead (II) with a "Turn-on" Fluorescent Biosensor Based on Energy Transfer from Cdse/Zns Quantum Dots to Graphene Oxide. *Biosens. Bioelectron.* **2013**, *43*, 69-74.

44. He, Y.; Lin, Y.; Tang, H.; Pang, D., A Graphene Oxide-Based Fluorescent Aptasensor for the Turn-on Detection of Epithelial Tumor Marker Mucin 1. *Nanoscale* **2012**, *4*, 2054-2059.

45. Chang, H.; Tang, L.; Wang, Y.; Jiang, J.; Li, J., Graphene Fluorescence Resonance Energy Transfer Aptasensor for the Thrombin Detection. *Anal. Chem.* **2010**, *82*, 2341-2346.

46. Zhang, M.; Yin, B. C.; Tan, W.; Ye, B. C., A Versatile Graphene-Based Fluorescence "on/off" Switch for Multiplex Detection of Various Targets. *Biosens. Bioelectron.* **2011**, *26*, 3260-3265.

47. Wang, Y.; Li, Z.; Wang, J.; Li, J.; Lin, Y., Graphene and Graphene Oxide: Biofunctionalization and Applications in Biotechnology. *Trends Biotechnol.* **2011**, *29*, 205-212.

48. Pena-Bahamonde, J.; Nguyen, H. N.; Fanourakis, S. K.; Rodrigues, D. F., Recent Advances in Graphene-Based Biosensor Technology with Applications in Life Sciences. *J. Nanobiotech.* **2018**, *16*, 75.

49. Wu, Y.; Tilley, R. D.; Gooding, J. J., The Challenges and Solutions in Developing Ultrasensitive Biosensors. *J. Am. Chem. Soc.* **2018**, *141*, 1162-1170.

50. Zhao, Y.; Chen, F.; Li, Q.; Wang, L.; Fan, C., Isothermal Amplification of Nucleic Acids. *Chem. Rev.* **2015**, *115*, 12491-12545.
51. Laborda, F.; Jiménez-Lamana, J.; Bolea, E.; Castillo, J. R., Critical Considerations for the Determination of Nanoparticle Number Concentrations, Size and Number Size Distributions by Single Particle ICP-MS. *J. Anal. At. Spectrom.* **2013**, *28*, 1220-1232.
52. Lin, F.-h.; Miyashita, S.-i.; Inagaki, K.; Liu, Y.-H.; Hsu, I. H., Evaluation of Three Different Sample Introduction Systems for Single-Particle Inductively Coupled Plasma Mass Spectrometry (spICP-MS) Applications. *J. Anal. At. Spectrom.* **2019**, *34*, 401-406.
53. Montoro Bustos, A. R.; Petersen, E. J.; Possolo, A.; Winchester, M. R., Post Hoc Interlaboratory Comparison of Single Particle ICP-MS Size Measurements of Nist Gold Nanoparticle Reference Materials. *Anal. Chem.* **2015**, *87*, 8809-8817.
54. Peters, R.; Herrera-Rivera, Z.; Undas, A.; van der Lee, M.; Marvin, H.; Bouwmeester, H.; Weigel, S., Single Particle ICP-MS Combined with a Data Evaluation Tool as a Routine Technique for the Analysis of Nanoparticles in Complex Matrices. *J. Anal. At. Spectrom.* **2015**, *30*, 1274-1285.
55. Hu, J.; Deng, D.; Liu, R.; Lv, Y., Single Nanoparticle Analysis by ICPMS: A Potential Tool for Bioassay. *J. Anal. At. Spectrom.* **2018**, *33*, 57-67.
56. Zhang, S.; Han, G.; Xing, Z.; Zhang, S.; Zhang, X., Multiplex DNA Assay Based on Nanoparticle Probes by Single Particle Inductively Coupled Plasma Mass Spectrometry. *Anal. Chem.* **2014**, *86*, 3541-3547.
57. Kelley, S. O., What Are Clinically Relevant Levels of Cellular and Biomolecular Analytes? *ACS Sens.* **2017**, *2*, 193-197.
58. Ilgu, M.; Nilsen-Hamilton, M., Aptamers in Analytics. *Analyst* **2016**, *141*, 1551-1568.
59. Yan, L.; Zhou, J.; Zheng, Y.; Gamson, A. S.; Roembke, B. T.; Nakayama, S.; Sintim, H. O., Isothermal Amplified Detection of DNA and RNA. *Mol. Biosyst.* **2014**, *10*, 970-1003.
60. Lee, J.; Kim, J.; Kim, S.; Min, D. H., Biosensors Based on Graphene Oxide and Its Biomedical Application. *Adv. Drug Deliv. Rev.* **2016**, *105*, 275-287.
61. Liu, J., Adsorption of DNA onto Gold Nanoparticles and Graphene Oxide: Surface Science and Applications. *Phys. Chem. Chem. Phys.* **2012**, *14*, 10485-10496.
62. Wu, M.; Kempaiah, R.; Huang, P. J.; Maheshwari, V.; Liu, J., Adsorption and Desorption of DNA on Graphene Oxide Studied by Fluorescently Labeled Oligonucleotides. *Langmuir* **2011**, *27*, 2731-2738.
63. Zhang, Y.; Xia, J.; Zhang, F.; Wang, Z.; Liu, Q., Ultrasensitive Label-Free Homogeneous Electrochemical Aptasensor Based on Sandwich Structure for Thrombin Detection. *Sens. Actuators B Chem.* **2018**, *267*, 412-418.

64. Wang, C.; Qian, Y.; Zhang, Y.; Meng, S.; Wang, S.; Li, Y.; Gao, F., A Novel Label-Free and Signal-on Electrochemical Aptasensor Based on the Autonomous Assembly of Hemin/G-Quadruplex and Direct Electron Transfer of Hemin. *Sens. Actuators B Chem.* **2017**, *238*, 434-440.
65. Schmelcher, M.; Loessner, M. J., Application of Bacteriophages for Detection of Foodborne Pathogens. *Bacteriophage* **2014**, *4*, e28137.
66. Chen, J.; Alcaine, S. D.; Jiang, Z.; Rotello, V. M.; Nugen, S. R., Detection of Escherichia Coli in Drinking Water Using T7 Bacteriophage-Conjugated Magnetic Probe. *Anal. Chem.* **2015**, *87*, 8977-8984.
67. Wang, Y.; Ye, Z.; Si, C.; Ying, Y., Monitoring of Escherichia Coli O157:H7 in Food Samples Using Lectin Based Surface Plasmon Resonance Biosensor. *Food Chem.* **2013**, *136*, 1303-1308.
68. Yuan, S. J.; Li, W. W.; Cheng, Y. Y.; He, H.; Chen, J. J.; Tong, Z. H.; Lin, Z. Q.; Zhang, F.; Sheng, G. P.; Yu, H. Q., A Plate-Based Electrochromic Approach for the High-Throughput Detection of Electrochemically Active Bacteria. *Nat. Protoc.* **2014**, *9*, 112-119.
69. Edgar, R.; McKinstry, M.; Hwang, J.; Oppenheim, A. B.; Fekete, R. A.; Giulian, G.; Merrill, C.; Nagashima, K.; Adhya, S., High-Sensitivity Bacterial Detection Using Biotin-Tagged Phage and Quantum-Dot Nanocomplexes. *Proc. Nat.l Acad. Sci.* **2006**, *103*, 4841-4845.
70. Guo, Q.; Han, J. J.; Shan, S.; Liu, D. F.; Wu, S. S.; Xiong, Y. H.; Lai, W. H., DNA-Based Hybridization Chain Reaction and Biotin-Streptavidin Signal Amplification for Sensitive Detection of Escherichia Coli O157:H7 through Elisa. *Biosens. Bioelectron.* **2016**, *86*, 990-995.
71. Nazemi, E.; Aithal, S.; Hassen, W. M.; Frost, E. H.; Dubowski, J. J., Gaas/Algaas Heterostructure Based Photonic Biosensor for Rapid Detection of Escherichia Coli in Phosphate Buffered Saline Solution. *Sens. Actuators B Chem.* **2015**, *207*, 556-562.
72. Patel, P.; Garson, J. A.; Tettmar, K. I.; Ancliff, S.; McDonald, C.; Pitt, T.; Coelho, J.; Tedder, R. S., Development of an Ethidium Monoazide-Enhanced Internally Controlled Universal 16s Rdna Real-Time Polymerase Chain Reaction Assay for Detection of Bacterial Contamination in Platelet Concentrates. *Transfusion* **2012**, *52*, 1423-1432.
73. Mannoor, M. S.; Zhang, S.; Link, A. J.; McAlpine, M. C., Electrical Detection of Pathogenic Bacteria Via Immobilized Antimicrobial Peptides. *Proc. Nat.l Acad. Sci.* **2010**, *107*, 19207-19212.
74. Etayash, H.; Jiang, K.; Thundat, T.; Kaur, K., Impedimetric Detection of Pathogenic Gram-Positive Bacteria Using an Antimicrobial Peptide from Class Iia Bacteriocins. *Anal. Chem.* **2014**, *86*, 1693-1700.

75. Yoo, S. M.; Kim, D. K.; Lee, S. Y., Aptamer-Functionalized Localized Surface Plasmon Resonance Sensor for the Multiplexed Detection of Different Bacterial Species. *Talanta* **2015**, *132*, 112-117.
76. Wang, J.; Morton, M. J.; Elliott, C. T.; Karoonuthaisiri, N.; Segatori, L.; Biswal, S. L., Rapid Detection of Pathogenic Bacteria and Screening of Phage-Derived Peptides Using Microcantilevers. *Anal. Chem.* **2014**, *86*, 1671-1678.
77. Lee, M. H.; Kim, J. S.; Sessler, J. L., Small Molecule-Based Ratiometric Fluorescence Probes for Cations, Anions, and Biomolecules. *Chem. Soc. Rev.* **2015**, *44*, 4185-4191.
78. Wen, J.; Xu, Y.; Li, H.; Lu, A.; Sun, S., Recent Applications of Carbon Nanomaterials in Fluorescence Biosensing and Bioimaging. *Chem. Commun.* **2015**, *51*, 11346-11358.
79. Shi, H.; Wei, J.; Qiang, L.; Chen, X.; Meng, X., Fluorescent Carbon Dots for Bioluminescence and Biosensing Applications. *J. Biomed. Nanotechnol.* **2014**, *10*, 2677-2699.
80. Li, B.; Yu, Q.; Duan, Y., Fluorescent Labels in Biosensors for Pathogen Detection. *Crit. Rev. Biotechnol.* **2015**, *35*, 82-93.
81. Wegner, K. D.; Hildebrandt, N., Quantum Dots: Bright and Versatile in Vitro and in Vivo Fluorescence Imaging Biosensors. *Chem. Soc. Rev.* **2015**, *44*, 4792-4834.
82. Geszke-Moritz, M.; Moritz, M., Quantum Dots as Versatile Probes in Medical Sciences: Synthesis, Modification and Properties. *Mater. Sci. Eng. C Mater. Bio. Appl.* **2013**, *33*, 1008-1021.
83. Zheng, X. T.; Ananthanarayanan, A.; Luo, K. Q.; Chen, P., Glowing Graphene Quantum Dots and Carbon Dots: Properties, Syntheses, and Biological Applications. *Small* **2015**, *11*, 1620-36.
84. Wu, X.; Tian, F.; Wang, W.; Chen, J.; Wu, M.; Zhao, J. X., Fabrication of Highly Fluorescent Graphene Quantum Dots Using L-Glutamic Acid for in Vitro/in Vivo Imaging and Sensing. *J. Mater. Chem. C* **2013**, *1*, 4676-4684.
85. Rotaru, A.; Dutta, S.; Jentsch, E.; Gothelf, K.; Mokhir, A., Selective Dsdna-Templated Formation of Copper Nanoparticles in Solution. *Angew. Chem. Int. Ed. Engl.* **2010**, *49*, 5665-5667.
86. Xu, F.; Shi, H.; He, X.; Wang, K.; He, D.; Guo, Q.; Qing, Z.; Yan, L.; Ye, X.; Li, D.; Tang, J., Concatemeric Dsdna-Templated Copper Nanoparticles Strategy with Improved Sensitivity and Stability Based on Rolling Circle Replication and Its Application in Microrna Detection. *Anal. Chem.* **2014**, *86*, 6976-6982.
87. Zhou, Z.; Du, Y.; Dong, S., Double-Strand DNA-Templated Formation of Copper Nanoparticles as Fluorescent Probe for Label-Free Aptamer Sensor. *Anal. Chem.* **2011**, *83*, 5122-5127.

88. Song, C.; Yang, X.; Wang, K.; Wang, Q.; Huang, J.; Liu, J.; Liu, W.; Liu, P., Label-Free and Non-Enzymatic Detection of DNA Based on Hybridization Chain Reaction Amplification and dsDNA-Templated Copper Nanoparticles. *Anal. Chim. Acta* **2014**, *827*, 74-79.
89. Zhao, J.; Hu, S.; Cao, Y.; Zhang, B.; Li, G., Electrochemical Detection of Protein Based on Hybridization Chain Reaction-Assisted Formation of Copper Nanoparticles. *Biosens. Bioelectron.* **2015**, *66*, 327-331.
90. Jia, X.; Li, J.; Han, L.; Ren, J.; Yang, X.; Wang, E., DNA-Hosted Copper Nanoclusters for Fluorescent Identification of Single Nucleotide Polymorphisms. *ACS Nano* **2012**, *6*, 3311-3317.
91. Ma, J.-L.; Yin, B.-C.; Wu, X.; Ye, B.-C., Copper-Mediated DNA-Scaffolded Silver Nanocluster on-off Switch for Detection of Pyrophosphate and Alkaline Phosphatase. *Anal. Chem.* **2016**, *88*, 9219-9225.
92. Saiki, R.; Gelfand, D.; Stoffel, S.; Scharf, S.; Higuchi, R.; Horn, G.; Mullis, K.; Erlich, H., Primer-Directed Enzymatic Amplification of DNA with a Thermostable DNA Polymerase. *Science* **1988**, *239*, 487-491.
93. Simpson, J. M.; Lim, D. V., Rapid Pcr Confirmation of E. Coli O157:H7 after Evanescent Wave Fiber Optic Biosensor Detection. *Biosens. Bioelectron.* **2005**, *21*, 881-887.
94. Walker, G. T.; Little, M. C.; Nadeau, J. G.; Shank, D. D., Isothermal in Vitro Amplification of DNA by a Restriction Enzyme/DNA Polymerase System. *Proc. Natl. Acad. Sci.* **1992**, *89*, 392-396.
95. Shi, C.; Liu, Q.; Ma, C.; Zhong, W., Exponential Strand-Displacement Amplification for Detection of Micrnas. *Anal. Chem.* **2014**, *86*, 336-339.
96. Cao, A.; Zhang, C. Y., Sensitive and Label-Free DNA Methylation Detection by Ligation-Mediated Hyperbranched Rolling Circle Amplification. *Anal. Chem.* **2012**, *84*, 6199-6205.
97. Barany, F., Genetic Disease Detection and DNA Amplification Using Cloned Thermostable Ligase. *Proc. Natl. Acad. Sci.* **1991**, *88*, 189-193.
98. Dirks, R. M.; Pierce, N. A., Triggered Amplification by Hybridization Chain Reaction. *Proc. Natl. Acad. Sci.* **2004**, *101*, 15275-15278.
99. Chen, Q.; Guo, Q.; Chen, Y.; Pang, J.; Fu, F.; Guo, L., An Enzyme-Free and Label-Free Fluorescent Biosensor for Small Molecules by G-Quadruplex Based Hybridization Chain Reaction. *Talanta* **2015**, *138*, 15-19.
100. Dai, S.; Xue, Q.; Zhu, J.; Ding, Y.; Jiang, W.; Wang, L., An Ultrasensitive Fluorescence Assay for Protein Detection by Hybridization Chain Reaction-Based DNA Nanotags. *Biosens. Bioelectron.* **2014**, *51*, 421-425.

101. Bao, T.; Wen, W.; Zhang, X.; Xia, Q.; Wang, S., An Exonuclease-Assisted Amplification Electrochemical Aptasensor for Hg(2+) Detection Based on Hybridization Chain Reaction. *Biosens. Bioelectron.* **2015**, *70*, 318-323.
102. Wang, Y. M.; Wu, Z.; Liu, S. J.; Chu, X., Structure-Switching Aptamer Triggering Hybridization Chain Reaction on the Cell Surface for Activatable Theranostics. *Anal. Chem.* **2015**, *87*, 6470-6474.
103. Esteban-Fernandez de Avila, B.; Pedrero, M.; Campuzano, S.; Escamilla-Gomez, V.; Pingarron, J. M., Sensitive and Rapid Amperometric Magnetoimmunosensor for the Determination of Staphylococcus Aureus. *Anal. Bioanal. Chem.* **2012**, *403*, 917-925.
104. Dissemond, J.; Augustin, M.; Eming, S. A.; Goerge, T.; Horn, T.; Karrer, S.; Schumann, H.; Stucker, M., Modern Wound Care - Practical Aspects of Non-Interventional Topical Treatment of Patients with Chronic Wounds. *J. Dtsch. Dermatol. Ges.* **2014**, *12*, 541-554.
105. Wu, W.; Zhang, J.; Zheng, M.; Zhong, Y.; Yang, J.; Zhao, Y.; Wu, W.; Ye, W.; Wen, J.; Wang, Q.; Lu, J., An Aptamer-Based Biosensor for Colorimetric Detection of *Escherichia Coli* O157:H7. *PLoS ONE* **2012**, *7*, e48999.
106. Kulpakko, J.; Kopra, K.; Hanninen, P., Time-Resolved Fluorescence-Based Assay for Rapid Detection of *Escherichia Coli*. *Anal. Biochem.* **2015**, *470*, 1-6.
107. Rizzello, L.; Pompa, P. P., Nanosilver-Based Antibacterial Drugs and Devices: Mechanisms, Methodological Drawbacks, and Guidelines. *Chem. Soc. Rev.* **2014**, *43*, 1501-1518.
108. Marambio-Jones, C.; Hoek, E. M. V., A Review of the Antibacterial Effects of Silver Nanomaterials and Potential Implications for Human Health and the Environment. *J. Nanopart. Res.* **2010**, *12*, 1531-1551.
109. Williamson, D. A.; Carter, G. P.; Howden, B. P., Current and Emerging Topical Antibacterials and Antiseptics: Agents, Action, and Resistance Patterns. *Clin. Microbiol. Rev.* **2017**, *30*, 827-860.
110. Levy, S. B.; Marshall, B., Antibacterial Resistance Worldwide: Causes, Challenges and Responses. *Nat. Med.* **2004**, *10*, s122-129.
111. Buffet-Bataillon, S.; Tattevin, P.; Bonnaure-Mallet, M.; Jolivet-Gougeon, A., Emergence of Resistance to Antibacterial Agents: The Role of Quaternary Ammonium Compounds--a Critical Review. *Int. J. Antimicrob. Agents* **2012**, *39*, 381-389.
112. Eberlein, T.; Assadian, O., Clinical Use of Polihexanide on Acute and Chronic Wounds for Antisepsis and Decontamination. *Skin Pharmacol. Physiol.* **2010**, *23*, 45-51.
113. Chernousova, S.; Epple, M., Silver as Antibacterial Agent: Ion, Nanoparticle, and

Metal. *Angew. Chem. Int. Ed. Engl.* **2013**, *52*, 1636-1653.

114. Payne, D. J.; Gwynn, M. N.; Holmes, D. J.; Pompliano, D. L., Drugs for Bad Bugs: Confronting the Challenges of Antibacterial Discovery. *Nat. Rev. Drug Discov.* **2007**, *6*, 29-40.

115. Kim, K. J.; Sung, W. S.; Suh, B. K.; Moon, S. K.; Choi, J. S.; Kim, J. G.; Lee, D. G., Antifungal Activity and Mode of Action of Silver Nano-Particles on *Candida Albicans*. *Biometals* **2009**, *22*, 235-242.

116. Kang, S.; Pinault, M.; Pfefferle, L. D.; Elimelech, M., Single-Walled Carbon Nanotubes Exhibit Strong Antimicrobial Activity. *Langmuir* **2007**, *23*, 8670-8673.

117. Wu, M.-C.; Deokar, A. R.; Liao, J.-H.; Shih, P.-Y.; Ling, Y.-C., Graphene-Based Photothermal Agent for Rapid and Effective Killing of Bacteria. *ACS Nano* **2013**, *7*, 1281-1290.

118. Kholmanov, I. N.; Stoller, M. D.; Edgeworth, J.; Lee, W. H.; Li, H.; Lee, J.; Barnhart, C.; Potts, J. R.; Piner, R.; Akinwande, D.; Barrick, J. E.; Ruoff, R. S., Nanostructured Hybrid Transparent Conductive Films with Antibacterial Properties. *ACS Nano* **2012**, *6*, 5157-5163.

119. Liu, S.; Zeng, T. H.; Hofmann, M.; Burcombe, E.; Wei, J.; Jiang, R.; Kong, J.; Chen, Y., Antibacterial Activity of Graphite, Graphite Oxide, Graphene Oxide, and Reduced Graphene Oxide: Membrane and Oxidative Stress. *ACS Nano* **2011**, *5*, 6971-6980.

120. Loo, A. E. K.; Wong, Y. T.; Ho, R.; Wasser, M.; Du, T.; Ng, W. T.; Halliwell, B., Effects of Hydrogen Peroxide on Wound Healing in Mice in Relation to Oxidative Damage. *PLoS ONE* **2012**, *7*, e49215.

121. Hayashi, E.; Mokudai, T.; Yamada, Y.; Nakamura, K.; Kanno, T.; Sasaki, K.; Niwano, Y., In Vitro and in Vivo Anti-Staphylococcus Aureus Activities of a New Disinfection System Utilizing Photolysis of Hydrogen Peroxide. *J. Biosci. Bioeng.* **2012**, *114*, 193-197.

122. Murdoch, L. E.; Bailey, L.; Banham, E.; Watson, F.; Adams, N. M.; Chewins, J., Evaluating Different Concentrations of Hydrogen Peroxide in an Automated Room Disinfection System. *Lett. Appl. Microbiol.* **2016**, *63*, 178-82.

123. Vatansever, F.; de Melo, W. C.; Avci, P.; Vecchio, D.; Sadasivam, M.; Gupta, A.; Chandran, R.; Karimi, M.; Parizotto, N. A.; Yin, R.; Tegos, G. P.; Hamblin, M. R., Antimicrobial Strategies Centered around Reactive Oxygen Species--Bactericidal Antibiotics, Photodynamic Therapy, and Beyond. *FEMS Microbiol. Rev.* **2013**, *37*, 955-989.

124. Walling, C., Fenton's Reagent Revisited. *Acc. Chem. Res.* **1975**, *8*, 125-131.

125. Fenton, H. J. H., Lxxiii.-Oxidation of Tartaric Acid in Presence of Iron. *J. Chem. Soc. Trans.* **1894**, *65*, 899-910.

126. Hayyan, M.; Hashim, M. A.; AlNashef, I. M., Superoxide Ion: Generation and Chemical Implications. *Chem. Rev.* **2016**, *116*, 3029-3085.
127. Nahon, P.; Sutton, A.; Rufat, P.; Zioli, M.; Akouche, H.; Laguillier, C.; Charneau, N.; Ganne-Carrie, N.; Grando-Lemaire, V.; N'Kontchou, G.; Trinchet, J. C.; Gattegno, L.; Pessayre, D.; Beaugrand, M., Myeloperoxidase and Superoxide Dismutase 2 Polymorphisms Comodulate the Risk of Hepatocellular Carcinoma and Death in Alcoholic Cirrhosis. *Hepatology* **2009**, *50*, 1484-1493.
128. Gębicka, L.; Gębicki, J. L., Modification of Horseradish Peroxidase Induced by Hydroxyl Radicals. The Influence of Oxygen. *Biochimie* **1996**, *78*, 62-65.
129. Martins, D.; Titorenko, V. I.; English, A. M., Cells with Impaired Mitochondrial H₂O₂ Sensing Generate Less *OH Radicals and Live Longer. *Antioxid Redox Signal* **2014**, *21*, 1490-1503.
130. Sun, H.; Gao, N.; Dong, K.; Ren, J.; Qu, X., Graphene Quantum Dots-Band-Aids Used for Wound Disinfection. *ACS Nano* **2014**, *8*, 6202-6210.
131. Wang, Z.; Dong, K.; Liu, Z.; Zhang, Y.; Chen, Z.; Sun, H.; Ren, J.; Qu, X., Activation of Biologically Relevant Levels of Reactive Oxygen Species by Au/g-C₃N₄ Hybrid Nanozyme for Bacteria Killing and Wound Disinfection. *Biomaterials* **2017**, *113*, 145-157.
132. Gao, L.; Giglio, K. M.; Nelson, J. L.; Sondermann, H.; Travis, A. J., Ferromagnetic Nanoparticles with Peroxidase-Like Activity Enhance the Cleavage of Biological Macromolecules for Biofilm Elimination. *Nanoscale* **2014**, *6*, 2588-2593.
133. Ivankovic, S.; Music, S.; Gotic, M.; Ljubetic, N., Cytotoxicity of Nanosize V(2)O(5) Particles to Selected Fibroblast and Tumor Cells. *Toxicol. In Vitro* **2006**, *20*, 286-94.
134. Yang, J. F.; Zhou, S. B.; Xiao, A. G.; Li, W. J.; Ying, G.-G., Chemical Oxidation of Sulfadiazine by the Fenton Process: Kinetics, Pathways, Toxicity Evaluation. *J. Environ. Sci. Health B* **2014**, *49*, 909-916.
135. Zhou, W.; Saran, R.; Liu, J., Metal Sensing by DNA. *Chem. Rev.* **2017**, *117*, 8272-8325.
136. Liu, J.; Lu, Y., A Colorimetric Lead Biosensor Using Dnazyme-Directed Assembly of Gold Nanoparticles. *J. Am. Chem. Soc.* **2003**, *125*, 6642-6643.
137. Liu, J.; Cao, Z.; Lu, Y., Functional Nucleic Acid Sensors. *Chem. Rev.* **2009**, *109*, 1948-1998.
138. Li, Y.; Sen, D., Toward an Efficient Dnazyme. *Biochemistry* **1997**, *36*, 5589-5599.
139. Kosman, J.; Juskowiak, B., Peroxidase-Mimicking Dnazymes for Biosensing Applications: A Review. *Anal. Chim. Acta* **2011**, *707*, 7-17.

140. Stefan, L.; Denat, F.; Monchaud, D., Insights into How Nucleotide Supplements Enhance the Peroxidase-Mimicking Dnazyme Activity of the G-Quadruplex/Hemin System. *Nucleic Acids Res.* **2012**, *40*, 8759-8772.
141. Ma, D. L.; Zhang, Z.; Wang, M.; Lu, L.; Zhong, H. J.; Leung, C. H., Recent Developments in G-Quadruplex Probes. *Chem. Biol.* **2015**, *22*, 812-828.
142. Gribas, A. V.; Zhao, S.; Sakharov, I. Y., Improved Method for Chemiluminescent Determination of Peroxidase-Mimicking Dnazyme Activity. *Anal. Biochem.* **2014**, *466*, 19-23.
143. Zhang, L.; Er, J. C.; Li, X.; Heng, J. J.; Samanta, A.; Chang, Y. T.; Lee, C. L., Development of Fluorescent Probes Specific for Parallel-Stranded G-Quadruplexes by a Library Approach. *Chem. Commun. (Camb)* **2015**, *51*, 7386-7389.
144. Tan, X.; Wang, Y.; Armitage, B. A.; Bruchez, M. P., Label-Free Molecular Beacons for Biomolecular Detection. *Anal. Chem.* **2014**, *86*, 10864-10869.
145. Li, T.; Dong, S.; Wang, E., Label-Free Colorimetric Detection of Aqueous Mercury Ion (Hg^{2+}) Using Hg^{2+} -Modulated G-Quadruplex-Based Dnazymes. *Anal. Chem.* **2009**, *81*, 2144-2149.
146. Zhao, M.; Liao, N.; Zhuo, Y.; Chai, Y. Q.; Wang, J. P.; Yuan, R., Triple Quenching of a Novel Self-Enhanced Ru(II) Complex by Hemin/G-Quadruplex Dnazymes and Its Potential Application to Quantitative Protein Detection. *Anal. Chem.* **2015**, *87*, 7602-7609.
147. Cheng, X.; Liu, X.; Bing, T.; Cao, Z.; Shangguan, D., General Peroxidase Activity of G-Quadruplex-Hemin Complexes and Its Application in Ligand Screening. *Biochemistry* **2009**, *48*, 7817-7823.
148. Yang, X.; Fang, C.; Mei, H.; Chang, T.; Cao, Z.; Shangguan, D., Characterization of G-Quadruplex/Hemin Peroxidase: Substrate Specificity and Inactivation Kinetics. *Chemistry* **2011**, *17*, 14475-14484.
149. Zhang, Z.; Liu, J., Intracellular Delivery of a Molecularly Imprinted Peroxidase Mimicking Dnazyme for Selective Oxidation. *Mater. Horiz.* **2018**, *5*, 738-744.
150. Yaku, H.; Murashima, T.; Miyoshi, D.; Sugimoto, N., Specific Binding of Anionic Porphyrin and Phthalocyanine to the G-Quadruplex with a Variety of in Vitro and in Vivo Applications. *Molecules* **2012**, *17*, 10586-10613.
151. Li, J.; Zheng, W.; Kwon, A. H.; Lu, Y., In Vitro Selection and Characterization of a Highly Efficient Zn(II)-Dependent Rna-Cleaving Deoxyribozyme. *Nucleic Acids Res.* **2000**, *28*, 481-488.
152. Yuan, K.; Xie, K.; Fox, J.; Zeng, H.; Gao, H.; Huang, C.; Wu, M., Decreased Levels of Mir-224 and the Passenger Strand of Mir-221 Increase Mbd2, Suppressing

Maspin and Promoting Colorectal Tumor Growth and Metastasis in Mice. *Gastroenterology* **2013**, *145*, 853-864.e9.

153. Zhu, L.; Li, C.; Zhu, Z.; Liu, D.; Zou, Y.; Wang, C.; Fu, H.; Yang, C. J., In Vitro Selection of Highly Efficient G-Quadruplex-Based Dnazymes. *Anal. Chem.* **2012**, *84*, 8383-8390.

154. Li, X.; He, S.; Zhou, X.; Ye, Y.; Tan, S.; Zhang, S.; Li, R.; Yu, M.; Jundt, M. C.; Hidebrand, A.; Wang, Y.; Li, G.; Huang, C.; Wu, M., Lyn Delivers Bacteria to Lysosomes for Eradication through Tlr2-Initiated Autophagy Related Phagocytosis. *PLoS Pathog.* **2016**, *12*, e1005363.

155. Li, X.; He, S.; Li, R.; Zhou, X.; Zhang, S.; Yu, M.; Ye, Y.; Wang, Y.; Huang, C.; Wu, M., Pseudomonas Aeruginosa Infection Augments Inflammation through Mir-301b Repression of C-Myb-Mediated Immune Activation and Infiltration. *Nat. Microbiol.* **2016**, *1*, 16132.

156. Guo, Q.; Shen, N.; Yuan, K.; Li, J.; Wu, H.; Zeng, Y.; Fox, J., 3rd; Bansal, A. K.; Singh, B. B.; Gao, H.; Wu, M., Caveolin-1 Plays a Critical Role in Host Immunity against Klebsiella Pneumoniae by Regulating Stat5 and Akt Activity. *Eur. J. Immunol.* **2012**, *42*, 1500-1511.

157. Kannan, S.; Pang, H.; Foster, D. C.; Rao, Z.; Wu, M., Human 8-Oxoguanine DNA Glycosylase Increases Resistance to Hyperoxic Cytotoxicity in Lung Epithelial Cells and Involvement with Altered Mapk Activity. *Cell Death Differ.* **2006**, *13*, 311-23.

158. He, S.; Li, X.; Li, R.; Fang, L.; Sun, L.; Wang, Y.; Wu, M., Annexin A2 Modulates Ros and Impacts Inflammatory Response Via Il-17 Signaling in Polymicrobial Sepsis Mice. *PLOS Pathog.* **2016**, *12*, e1005743.

159. Cai, N.; Li, Y.; Chen, S.; Su, X., A Fluorometric Assay Platform for Caffeic Acid Detection Based on the G-Quadruplex/Hemin Dnzyme. *Analyst* **2016**, *141*, 4456-4462.

160. Isaksen, I. S. A.; Dalsøren, S. B., Getting a Better Estimate of an Atmospheric Radical. *Science* **2011**, *331*, 38-39.

161. Fontmorin, J. M.; Burgos Castillo, R. C.; Tang, W. Z.; Sillanpaa, M., Stability of 5,5-Dimethyl-1-Pyrroline-N-Oxide as a Spin-Trap for Quantification of Hydroxyl Radicals in Processes Based on Fenton Reaction. *Water Res.* **2016**, *99*, 24-32.

162. Azman, N. A. M.; Peiró, S.; Fajarí, L.; Julià, L.; Almajano, M. P., Radical Scavenging of White Tea and Its Flavonoid Constituents by Electron Paramagnetic Resonance (EPR) Spectroscopy. *J. Agric. Food Chem.* **2014**, *62*, 5743-5748.

163. Hayashi, E.; Mokudai, T.; Yamada, Y.; Nakamura, K.; Kanno, T.; Sasaki, K.; Niwano, Y., In Vitro and in Vivo Anti-Staphylococcus Aureus Activities of a New Disinfection System Utilizing Photolysis of Hydrogen Peroxide. *J. Biosci. Bioeng.* **2012**, *114*, 193-197.

164. Ishibashi, K. I.; Fujishima, A.; Watanabe, T.; Hashimoto, K., Detection of Active Oxidative Species in TiO₂ Photocatalysis Using the Fluorescence Technique. *Electrochem. Commun.* **2000**, *2*, 207-210.
165. Ge, S.; Liu, F.; Liu, W.; Yan, M.; Song, X.; Yu, J., Colorimetric Assay of K-562 Cells Based on Folic Acid-Conjugated Porous Bimetallic Pd@Au Nanoparticles for Point-of-Care Testing. *Chem. Commun.* **2014**, *50*, 475-477.
166. Guo, Y.; Chen, J.; Cheng, M.; Monchaud, D.; Zhou, J.; Ju, H., A Thermophilic Tetramolecular G-Quadruplex/Hemin Dnzyme. *Angew. Chem. Int. Ed. Engl.* **2017**, *56*, 16636-16640.
167. Stefan, L.; Denat, F.; Monchaud, D., Deciphering the Dnzyme Activity of Multimeric Quadruplexes: Insights into Their Actual Role in the Telomerase Activity Evaluation Assay. *J. Am. Chem. Soc.* **2011**, *133*, 20405-20415.
168. Ye, Y.; Lin, P.; Zhang, W.; Tan, S.; Zhou, X.; Li, R.; Pu, Q.; Koff, J. L.; Dhasarathy, A.; Ma, F.; Deng, X.; Jiang, J.; Wu, M., DNA Repair Interacts with Autophagy to Regulate Inflammatory Responses to Pulmonary Hyperoxia. *J. Immunol.* **2017**, *198*, 2844-2853.
169. Wang, K.; Zhang, T.; Lei, Y.; Li, X.; Jiang, J.; Lan, J.; Liu, Y.; Chen, H.; Gao, W.; Xie, N.; Chen, Q.; Zhu, X.; Liu, X.; Xie, K.; Peng, Y.; Nice, E. C.; Wu, M.; Huang, C.; Wei, Y., Identification of Anxa2 (Annexin A2) as a Specific Bleomycin Target to Induce Pulmonary Fibrosis by Impeding Tfeb-Mediated Autophagic Flux. *Autophagy* **2018**, *14*, 269-282.
170. Li, L.-l.; Wang, H., Antibacterial Agents: Enzyme-Coated Mesoporous Silica Nanoparticles as Efficient Antibacterial Agents in Vivo (Adv. Healthcare Mater. 10/2013). *Adv. Healthc. Mater.* **2013**, *2*, 1298-1298.
171. Kumar, S.; Bandyopadhyay, U., Free Heme Toxicity and Its Detoxification Systems in Human. *Toxicol. Lett.* **2005**, *157*, 175-188.
172. Chen-Roetling, J.; Benvenisti-Zarom, L.; Regan, R. F., Cultured Astrocytes from Heme Oxygenase-1 Knockout Mice Are More Vulnerable to Heme-Mediated Oxidative Injury. *J. Neurosci. Res.* **2005**, *82*, 802-810.